

# REPORT DOCUMENTATION PAGE

Form Approved  
OMB No. 0704-0188

Public reporting burden for this collection of information is estimated to average 1 hour per response, including the time for reviewing instructions, searching existing data sources, gathering and maintaining the data needed, and completing and reviewing the collection of information. Send comments regarding this burden estimate or any other aspect of this collection of information, including suggestions for reducing this burden, to Washington Headquarters Services, Directorate for Information Operations and Reports, 1215 Jefferson Davis Highway, Suite 1204, Arlington, VA 22202-4302, and to the Office of Management and Budget, Paperwork Reduction Project (0704-0188), Washington, DC 20503.

1. AGENCY USE ONLY (Leave blank)	2. REPORT DATE 23 May 91	3. REPORT TYPE AND DATES COVERED THESIS/DISSERTATION
----------------------------------	-----------------------------	---

4. TITLE AND SUBTITLE Application of Modern Control Design Methodologies to a Multi-Segmented Deformable Mirror System	5. FUNDING NUMBERS <b>1</b>
---	--------------------------------

6. AUTHOR(S) Edgar M. Vaughan, Captain
---


7. PERFORMING ORGANIZATION NAME(S) AND ADDRESS(ES) AFIT Student Attending: Northeastern University	8. PERFORMING ORGANIZATION REPORT NUMBER AFIT/CI/CIA-91-032
---	--


9. SPONSORING/MONITORING AGENCY NAME(S) AND ADDRESS(ES) AFIT/CI Wright-Patterson AFB OH 45433-6583	10. SPONSORING/MONITORING AGENCY REPORT NUMBER
--	--

11. SUPPLEMENTARY NOTES

12a. DISTRIBUTION/AVAILABILITY STATEMENT Approved for Public Release IAW 190-1 Distributed Unlimited ERNEST A. HAYGOOD, 1st Lt, USAF Executive Officer	12b. DISTRIBUTION CODE
--	------------------------

13. ABSTRACT (Maximum 200 words)



**91-07276**  


**91 8 07 146**

14. SUBJECT TERMS	15. NUMBER OF PAGES 105
	16. PRICE CODE

17. SECURITY CLASSIFICATION OF REPORT	18. SECURITY CLASSIFICATION OF THIS PAGE	19. SECURITY CLASSIFICATION OF ABSTRACT	20. LIMITATION OF ABSTRACT
---------------------------------------	--	---	----------------------------

**AD-A239 415**  


**Application of Modern Control  
Design Methodologies  
to a  
Multi-Segmented Deformable Mirror System**

A Thesis Presented  
by  
Edgar Morris Vaughan, Captain, USAF

to

The Department of Electrical and Computer Engineering

in partial fulfillment of the requirements  
for the degree of

Master of Science  
in the field of  
Electrical Engineering



**NORTHEASTERN UNIVERSITY**  
Boston, Massachusetts

May 23, 1991

Accession for	
NTIS	CONF
DWC	786
U.S. DEPARTMENT OF COMMERCE	
JAN 1991	
By	
Date	
Auth	
Dist	Avail
A-1	

NORTHEASTERN UNIVERSITY

Graduate School

**Thesis Title:** Application of Modern Control Design Methodologies to a Multi-Segmented Deformable Mirror System

**Author:** Edgar Morris Vaughan, Captain, USAF

**Department:** Department of Electrical and Computer Engineering

Approved for Thesis of the Master of Science Degree - Department of Electrical and Computer Engineering

Signature of Author Edgar M Vaughan 5/23/91  
Date

Certified by John R Dowdle 5-23-91  
John R. Dowdle, Chief, Flight Systems Section  
The Charles Stark Draper Laboratory

Certified by Clas A. Jacobson  
Clas A. Jacobson, Assistant Professor  
Thesis Advisor

Certified by Gilead Tadmor 5-23-91  
Gilead Tadmor, Assistant Professor  
Thesis Advisor

Accepted by John G. Proakis 5-24-91  
John G. Proakis, Chairman  
Department of Electrical and Computer Engineering

Graduate School Notified of Acceptance

---

## Acknowledgement

I would like to thank the United States Air Force and the Charles Stark Draper Laboratory for the opportunity to pursue my Master's degree at Northeastern University. The opportunity to study while receiving the benefits of active duty status is a blessing and a coveted assignment of any Air Force Officer. The luxury of being able to concentrate only on technical matters has helped make this experience truly educational.

I would like to thank my Charles Stark Draper Laboratory Supervisor, Dr. John Dowdle, for his experience and encouragement throughout my time at Draper. I feel that the mixture of the education at Draper and Northeastern and the various view points of different experts in the theory of control has increased my understanding and made this experience rewarding.

I especially want to thank my Northeastern thesis advisors, Professor Gilead Tadmor and Professor Clas Jacobson. Professor Tadmor's enthusiasm for the mathematical theorems that are shaping modern control theory helped me to appreciate the complexity of multivariable control synthesis and analysis. Professor Jacobson's interest in robust control and decentralized control formed a basis of a significant portion of this thesis. Professor Jacobson continually pushed me to think and become an active learner, and his encouragement made the time very instructive. His dedicated time and effort in reading thesis drafts and offering suggestions were much appreciated.

I would like to thank Dr. Brent Appleby for his conscientious reading of this thesis. His comments were very thoughtful and his efforts aided immensely in the production of this final thesis product.

I want to thank my family for all of the support they have extended to me during my "school" years. My family has always supported me, and that support encourages me to strive to make them proud. I dedicate this thesis in memory of my father.

Finally and most importantly, I want to thank my wife, CeeAnn. Her continual support, encouragement, love, and partnership has been instrumental in whatever success my Master's program has carried.

This thesis was prepared at The Charles Stark Draper Laboratory, Inc., under Independent Research and Development funding. Publication of this report does not constitute approval by the Draper Laboratory or Northeastern University of the findings or conclusions contained herein. It is published solely for the exchange and stimulation of ideas.

### Abstract

The multi-segmented deformable mirror system is proposed as an element for a portion of a ballistic missile defense system. The size of the mirror required for this defense function requires that the mirror be developed in segments, and then these segments should be phased together to produce one continuous, large optic. The application of multivariable control system synthesis techniques to provide closed-loop wavefront control of the deformable mirror system is the problem discussed in this thesis. The method of  $H_{\infty}$  control system synthesis using loop-shaping techniques was used to develop a controller that meets a robust performance specification. The number and location of sensors was treated as a design variable, and the structured singular value ( $\mu$ ) was used to determine the performance robustness of the deformable mirror system. Decentralized control issues are also addressed through the use of necessary conditions in an effort to determine a suitable decentralized control structure with performance similar to that of the centralized controller.

# Contents

<b>1</b>	<b>Introduction</b>	<b>6</b>
1.1	Problem	6
1.2	Available Approaches	7
1.3	Thesis Contribution and Outline	8
<b>2</b>	<b>Description of Deformable Mirror System</b>	<b>10</b>
2.1	Overview	10
2.2	Structural Model Description	12
2.3	Performance Requirements	13
2.4	State Space Model and Control System Block Diagram	14
<b>3</b>	<b>Overview of Robustness Analysis Techniques</b>	<b>16</b>
3.1	Overview	16
3.2	Performance Analysis Tools - Transfer Function Norms	17
3.2.1	Definition of the $H_2$ Norm	17
3.2.2	$H_2$ Analysis	18
3.2.3	$H_\infty$ Analysis	19
3.3	Robust Stability Concepts	19
3.3.1	Small Gain Concepts	20
3.3.2	Structured Singular Value- $\mu$	22
<b>4</b>	<b>Problem Statement</b>	<b>25</b>
4.1	Issues Addressed	25
4.1.1	Simulation Issues	25
4.1.2	Performance Issues	26
4.1.3	Control Design Issues	27
4.1.4	Decentralized Control Issues	27
4.2	Goals	29
4.3	Conclusions	29
<b>5</b>	<b>Open-Loop Plant Analyses</b>	<b>31</b>
5.1	Basic Sensor Selection Requirements	31
5.2	Plant Condition Number	34
5.3	Controllability and Observability	38
5.4	Balancing and Model Reduction	42
5.5	Open-Loop Poles and Zeros	43
5.6	Conclusions	44

<b>6</b>	<b>Closed-Loop System</b>	<b>46</b>
6.1	Sensor Uncertainty . . . . .	46
6.2	Robust Control Specifications . . . . .	48
6.2.1	Plant Augmentation . . . . .	50
6.2.2	Sensitivity Weighting Function . . . . .	53
6.2.3	Complementary Sensitivity Weighting Function . . . . .	54
6.2.4	Control Input Weighting Function . . . . .	55
6.2.5	Robust Performance Weighting Specification . . . . .	55
6.3	$H_\infty$ Controller Solution . . . . .	56
6.3.1	Case 1: Single Petal Model Results . . . . .	59
6.3.2	Case 2: Full Model - 24 Sensors . . . . .	65
6.3.3	Case 3: Full Model - 36 Sensors . . . . .	69
6.4	Conclusions . . . . .	74
<b>7</b>	<b>Decentralized Control System Analyses</b>	<b>75</b>
7.1	Importance of Decentralized Control . . . . .	75
7.2	Necessary Conditions for Decentralized Integral Controllability . . . . .	77
7.2.1	Description of Tests . . . . .	77
7.2.2	Results of Application of DIC Tests to the Single Petal Model . . . . .	78
7.3	$\mu$ Interaction Measure . . . . .	85
7.3.1	Definition . . . . .	86
7.4	Necessary Tests for Viability of Control Configurations . . . . .	88
7.4.1	Discussion and Theorem . . . . .	90
7.4.2	Results of Application of Cross-Feed Performance Degradation Tests to Single Petal Model . . . . .	92
7.4.3	Results of Application of Cross-Feed Performance Degradation Tests to the Full Model Using 36 Sensors . . . . .	94
7.5	Conclusion . . . . .	94
<b>8</b>	<b>Conclusion</b>	<b>96</b>
8.1	Summary of Thesis . . . . .	96
8.2	Topics for Future Research . . . . .	98
<b>A</b>	<b>Performance Criteria Relations</b>	<b>100</b>

# List of Figures

2.1	Deformable Mirror System Schematic . . . . .	11
2.2	Top View of Composite Optic . . . . .	11
2.3	Wavefront Error Induced from Simple Tilt . . . . .	12
2.4	Sensor Positions - Edge Finite Element Nodes . . . . .	13
2.5	Block Diagram for the Deformable Mirror System . . . . .	15
3.1	Block-Diagram for Small Gain Theorem . . . . .	20
3.2	Feedback System for Stability Analysis . . . . .	20
3.3	Feedback System Including Uncertainty Block . . . . .	21
3.4	Reduced Block Diagram for Robust Stability Analysis . . . . .	21
3.5	M- $\Delta$ Block Diagram for Robust Performance Analysis . . . . .	22
5.1	Example of Sensor Locations - Single Petal Model . . . . .	32
5.2	Example of Sensor Locations - Full Model with 36 Sensors . . . . .	33
5.3	Example of Sensor Locations - Full Model with 24 Sensors . . . . .	33
5.4	Sensor Locations Chosen-Single Petal Model . . . . .	35
5.5	Condition Number - Single Petal Model . . . . .	36
5.6	Open-Loop Singular Value Plot of Single Petal Model . . . . .	36
5.7	Sensor Locations Chosen - Full Model with 36 Sensors . . . . .	37
5.8	Condition Number - Full Model with 36 Sensors . . . . .	37
5.9	Sensor Locations Chosen - Full Model with 24 Sensors . . . . .	38
5.10	Condition Number - Full Model with 24 Sensors . . . . .	39
5.11	Controllability Grammian Singular Values - Full Petal Model . . . . .	40
5.12	Observability Grammian Singular Values - Full Petal Model with 24 Sensors . . . . .	41
5.13	Observability Grammian Singular Values - Full Petal Model with 36 Sensors . . . . .	41
5.14	Hankel Singular Values - Full Model with 24 Sensors . . . . .	43
5.15	Comparison of Balanced and Unbalanced Controllability Grammian Singular Values . . . . .	44
6.1	Sensor Illustrating Multiplicative Uncertainty . . . . .	47
6.2	Block Diagram for the Deformable Mirror System . . . . .	47
6.3	Block Diagram Including Sensor Uncertainty . . . . .	47
6.4	Nominal Sensor Characteristics . . . . .	49
6.5	Uncertainty Weight Characteristics . . . . .	49
6.6	Augmented Form of Deformable Mirror System Block Diagram . . . . .	52
6.7	Standard Problem Block Diagram . . . . .	53
6.8	Sensitivity Function Bound . . . . .	54
6.9	Complementary Sensitivity Function Bound . . . . .	55
6.10	Robust Performance Bound . . . . .	56
6.11	Augmented Plant for Calculation of $H_\infty$ Controller . . . . .	57



6.12	$H_\infty$ Cost Function Singular Value Plot - Case 1 . . . . .	60
6.13	Singular Value Plot - Sensitivity Function - Case 1 . . . . .	60
6.14	Singular Value Plot - Complementary Sensitivity Function - Case 1 . . . . .	61
6.15	Singular Value Plot - Control Input Function - Case 1 . . . . .	61
6.16	Structured Singular Value ( $\mu$ ) - Robust Performance - Case 1 . . . . .	62
6.17	$\bar{\sigma}$ , $\mu$ , and $\rho$ Plots - Robust Performance -Case 1 . . . . .	63
6.18	Modified Sensor Uncertainty Weight . . . . .	63
6.19	Structured Singular Value ( $\mu$ ) - Robust Performance - Case 1 with Reduced Uncertainty	64
6.20	$\bar{\sigma}$ , $\mu$ , and $\rho$ Plots - Robust Performance -Case 1 with Reduced Uncertainty . . . . .	64
6.21	$H_\infty$ Cost Function Singular Value Plot - Case 2 . . . . .	66
6.22	Singular Value Plot - Sensitivity Function - Case 2 . . . . .	66
6.23	Singular Value Plot - Complementary Sensitivity Function - Case 2 . . . . .	67
6.24	Singular Value Plot - Control Input Function - Case 2 . . . . .	67
6.25	Structured Singular Value ( $\mu$ ) - Robust Performance - Case 2 . . . . .	68
6.26	$\bar{\sigma}$ , $\mu$ , and $\rho$ Plots - Robust Performance - Case 2 . . . . .	69
6.27	$H_\infty$ Cost Function Singular Value Plot - Case 3 . . . . .	70
6.28	Singular Value Plot - Sensitivity Function - Case 3 . . . . .	71
6.29	Singular Value Plot - Complementary Sensitivity Function - Case 3 . . . . .	71
6.30	Singular Value Plot - Control Input Function - Case 3 . . . . .	72
6.31	Structured Singular Value ( $\mu$ ) - Robust Performance - Case 3 . . . . .	72
6.32	Structured Singular Value ( $\mu$ ) - Robust Performance - Case 3 -Reduced Sensor Un- certainty . . . . .	73
7.1	Diagonal Controller Block Diagram . . . . .	76
7.2	Single Petal Showing Actuator and Sensor Numbers . . . . .	79
7.3	Input-Output Ordering of Possible DIC Structures Using Test 1 . . . . .	79
7.4	Input-Output Ordering of Possible DIC Structures Using Test 2 . . . . .	80
7.5	Input-Output Ordering of Possible DIC Structures Using Test 3 . . . . .	80
7.6	Comparison of DIC Controller Magnitude and Hinf Controller Magnitude . . . . .	81
7.7	SISO Sensitivity Transfer Functions - DIC . . . . .	82
7.8	Matrix Transfer Functions Using DIC; A: Sensitivity Function and Sensitivity Weight, B: Complementary Sensitivity Function and Complementary Sensitivity Function Weight, C: Control Input Function . . . . .	83
7.9	Robust Performance - Single Petal Model Using DIC . . . . .	84
7.10	Robust Performance - Single Petal Model Using DIC - Reduced Uncertainty . . . . .	84
7.11	Robust Performance - Single Petal Model Using DIC - Reduced Performance . . . . .	85
7.12	Representation of Off-Diagonal Portion of Plant as Uncertainty . . . . .	86
7.13	Equivalent Block-Diagram Representation Emphasizing Interaction Measure . . . . .	87
7.14	Interaction Measure Plots for DIC Cases . . . . .	89
7.15	Illustration of Partial Row and Complementary Partial Row Sums of RGA . . . . .	92
7.16	Single Petal Structures Passing Theorem 7.2 and Corollary 7.1 . . . . .	93

# Chapter 1

## Introduction

In 1984, President Reagan challenged the scientific community to develop a system that could be used to protect the United States from a ballistic missile attack. The development of such a system was organized under the Strategic Defense Initiative (SDI). The structure analyzed in this thesis is one element proposed for a portion of this defense system. The deformable mirror system is a multi-segmented reflective mirror proposed for deployment on a space platform. The size of the mirror required for this portion of the defense system requires that the mirror be developed in segments, and then these segments will be "phased" together to produce one continuous, large optic. The phasing of each of these segments is the application problem addressed in this thesis.

The multivariable, highly integrated, deformable mirror system structure requires very precise control action. Many control synthesis techniques have been developed to address multivariable systems. This thesis applies the technique of  $H_\infty$  loop-shaping to meet the performance requirements. This technique provides a method of incorporating control performance objectives into the design of the control system. This chapter introduces the deformable mirror system problem and discusses some of the available approaches that can be used to address the synthesis of the control system. The contribution of the thesis and an outline of the organization conclude this chapter.

### 1.1 Problem

The problem addressed in this thesis is the segment phasing of separate optics into an integrated optic. This is a low-bandwidth problem requiring the integrated surface of the optic to appear as a single mirror. Each individual optic contains force actuators to align each mirror. The figure of the integrated optic will be used to measure the performance. The results of this thesis will be a control system design to meet the required performance given a level of uncertainty in the model.

The uncertainty that is used in this model attempts to reflect the imperfect nature of the model versus the actual system. Simulations are shown to illustrate the effect of this uncertainty on

performance. The simulations will be used to determine the success of applying the control action to the models of the deformable mirror system.

After it is shown that the performance requirements can be met using a centralized controller, analyses are conducted to determine if a decentralized structure exists. The use of decentralized control would simplify the controller design and reduce the number of on-line computations leading to simpler hardware requirements.

## 1.2 Available Approaches

Multivariable control system synthesis techniques have been used with varying levels of success over the past two decades. Optimization techniques using quadratic norms led to Wiener-Hopf and Linear Quadratic Gaussian (LQG) or  $H_2$  control synthesis methods. The application of these synthesis methods requires a description of a particular power spectrum of the disturbance signals.  $H_2$  control systems can be sensitive to modeling errors because the norm is not suited for robustness analysis. There is no easy way to incorporate modeling uncertainty into the optimization problem that yields the compensator.

$H_\infty$  control designs also minimize the quadratic norm of the error, but they are based on minimizing a class of disturbances or a class of spectra. The  $H_\infty$  norm is an induced norm or a measure of maximum error over the class. Furthermore, the  $H_\infty$  norm is compatible with robustness analysis and can be used to incorporate bounded modeling uncertainty into the design. Through the use of singular values, multivariable "Bode" plots can be generated with interpretations similar to the Single Input Single Output (SISO) systems. The magnitude of various transfer function matrices can be measured using frequency dependent singular values. One method of designing  $H_\infty$  controllers is through the use of functions that bound the singular value plots of matrix transfer functions of interest. This method is referred to as "loop-shaping," where the controller performance specifications are appended to the plant model. Control synthesis is then performed on this "augmented" plant. An acceptable controller found for the augmented plant model will meet the performance requirements of the original plant model.

The maximum singular value is a sufficient measure of stability for a system in the presence of plant uncertainty, however, conservatism arises because the structure of the uncertainty cannot be incorporated. This means that uncertainty is "lumped" together to measure the stability. The nature of multivariable systems, specifically singular values, can make this "lumping" arbitrarily conservative. A non-conservative measure of robust stability and robust performance, called the structured singular value or  $\mu$ , was introduced by Doyle [6] in 1982. Through the use of a variation of the small-gain theorem, Doyle developed the "small  $\mu$ " theorem where the uncertainty structure

is exploited. The structured singular value also allows for the performance requirements to be incorporated into this uncertainty structure, thus providing a method to determine if performance is achieved with uncertainty present.

### 1.3 Thesis Contribution and Outline

The primary results of this thesis are the selection of sensors and the synthesis of a controller that satisfies the deformable mirror system performance requirements.  $H_\infty$  loop-shaping techniques are employed to develop the controller, and the structured singular value is used to measure the robustness. Possible decentralized structures are examined through the use of necessary conditions on robust stability. These necessary tests provide a means of reducing the number of possible decentralized structures to a manageable level.

Following this introductory chapter, this thesis is organized as follows:

Chapter 2 provides a description of the deformable mirror system including details of the structural model, performance requirements, and the development of the model into a format useful for control synthesis.

Chapter 3 gives an overview of robust control concepts and develops the tools used in this thesis for analysis. The use of the structured singular value is developed by reviewing the small gain and small  $\mu$  theorems. The application of the structured singular value to robust performance is discussed.

Chapter 4 details the specific problem statement addressed in this thesis. Through discussion of some of the issues encountered in developing a controller for the deformable mirror system, several subgoals are developed.

Chapter 5 presents the results of the open-loop plant analyses and provides an initial sensor selection used for the closed-loop analyses. Details concerning controllability and observability are provided, and the importance of balancing is shown with respect to the determination of controllability and observability. The open-loop poles and zeros are tested and the results provided.

Chapter 6 provides the details of the controllers designed for the deformable mirror system. Three separate cases are used in the development of the controller, and the method of  $H_\infty$  loop-shaping is presented. All of the weighting matrices used in the development of the  $H_\infty$  controller and the evaluation of the robust performance are provided, and results of each case are presented.

Chapter 7 contains the decentralized system analyses performed in an effort to determine the existence of a decentralized control structure. The term "structure" refers to the partitioning of the controller into a block-diagonal form. Through the use of necessary tests thousands of potential structures are eliminated, and a manageable subset results. More stringent tests are then applied

in an effort to determine a suitable decentralized structure.

Chapter 8 presents the conclusions and topics for future research on the deformable mirror system.

Appendix A develops the relationship between the  $\dot{H}_\infty$  norm and the rms performance requirement.

## Chapter 2

# Description of Deformable Mirror System

### 2.1 Overview

The deformable mirror system is a multi-segmented reflective optical system composed of a rigid, fixed circular center segment and six deformable petals (DPs) whose vertical positions, orientations, and shapes are actively controlled. The six DPs form an annulus about the rigid circular center, so that the composite deformable mirror system forms a large circular optic. A schematic of the deformable mirror system is shown in Figure 2.1, and a top-view of the system is shown in Figure 2.2. As seen from Figure 2.1, a laser source generates a beam that travels through a hole in the fixed center optic, reflects off the convex secondary mirror to expand the beam, and then reflects off of the primary mirror (fixed center optic and DPs) to produce the output beam. The primary mirror has a focal length such that the beam energy is focused on the desired target.

Many optic systems proposed for deployment in space require large surfaces with very tight figure specifications. The capability exists to manufacture small optical systems with a very tight figure specification. Unfortunately, as the size of the optic increases, the capability to maintain a tight figure specification decreases. Furthermore, the ability to accurately measure and assess the figure of the optic decreases with the size of the optic. One technique used to circumvent this problem is to produce small optics with tight figure specifications and combine these smaller optics into a larger optic. This eliminates the problem of fabricating a large optic but adds several difficulties to the control system design problem.

The practice of using several smaller optical systems to produce one larger system requires the "phasing" of each optic. Therefore, the control system needs to sense the position of each DP and phase these segments into one large optic. This thesis addresses the issue of robust wavefront control or "phasing" each optic in the presence of uncertainty. A detailed description of the system model is discussed below.

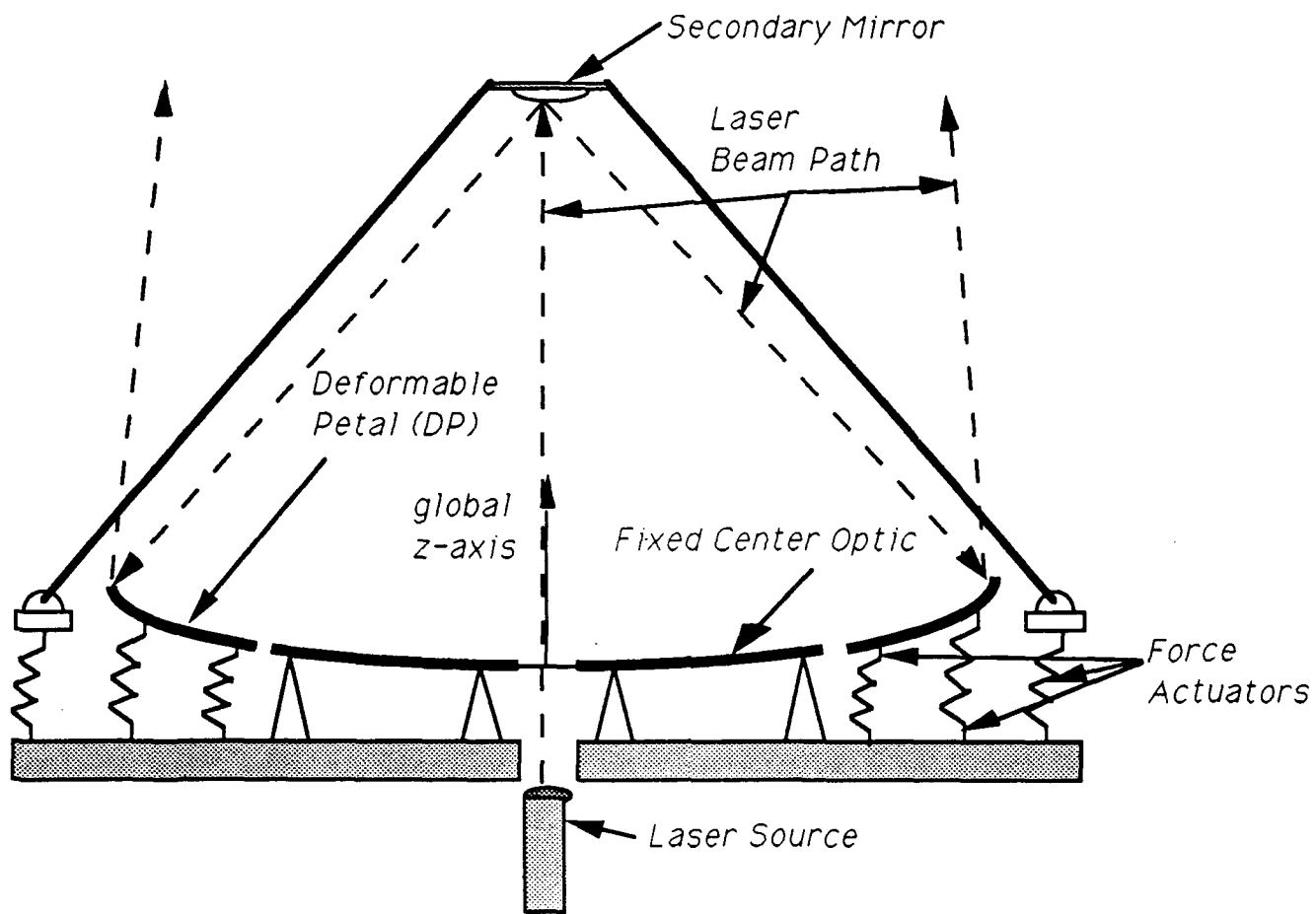


Figure 2.1: Deformable Mirror System Schematic

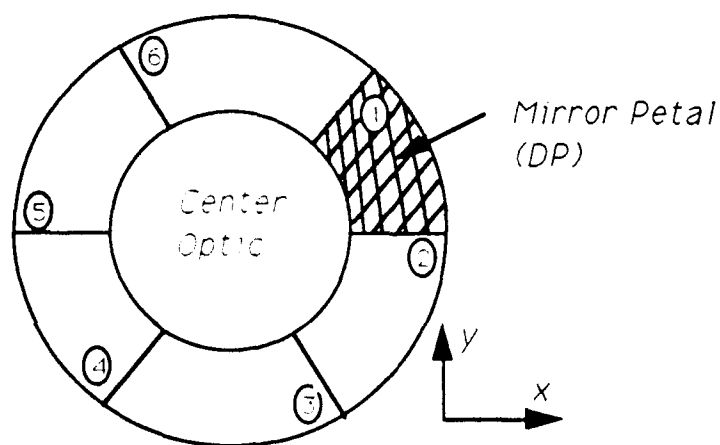


Figure 2.2: Top View of Composite Optic

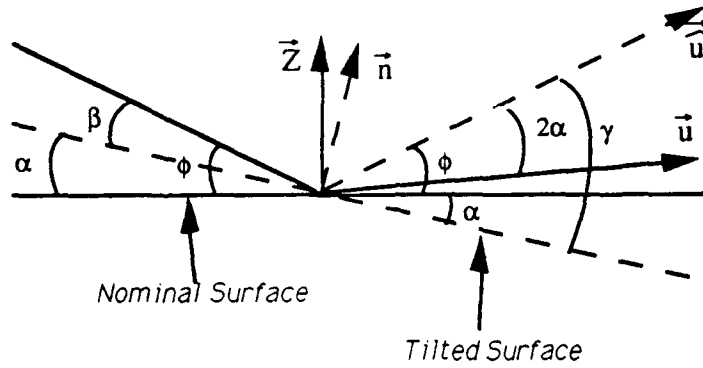


Figure 2.3: Wavefront Error Induced from Simple Tilt

## 2.2 Structural Model Description

The ten meter diameter primary mirror consists of the fixed center optic and the six DPs. The primary mirror model is a finite element representation generated through modal analysis of each DP and the support plate. Each DP has a general parabolic figure with a focal length of 12 m and contains 18 force actuators for figure control (108 figure actuators total) and 6 segment phasing actuators (36 segment phasing actuators total). The figure actuators deform each DP to actively produce specified shapes. The segment phasing actuators translate the DPs in a rigid body sense for petal to petal alignment.

The deformable mirror system model maps actuator forces to wavefront error at 56 finite element surface nodes (per petal). The wavefront error is defined by

$$WFE = 2\vec{Z} \bullet \vec{n}(\vec{u} \bullet \vec{n}) \quad (2.1)$$

where

$\vec{Z}$  = unit vector in the global z-direction

$\vec{n}$  = unit normal vector

$\vec{u}$  = wavefront vector

and

$\bullet$  denotes the vector dot product

A simple example of wavefront error is shown in Figure 2.3, where a nominal surface with a normal vector,  $\vec{Z}$ , is tilted by an angle of  $\alpha$ . The reflection of this tilt produces an output vector tilted by an angle of  $2\alpha$ . The vector,  $\vec{u}$ , shows the reflection of the wavefront from the nominal surface. The wavefront error is the projection of the wavefront vector in the global z-direction.



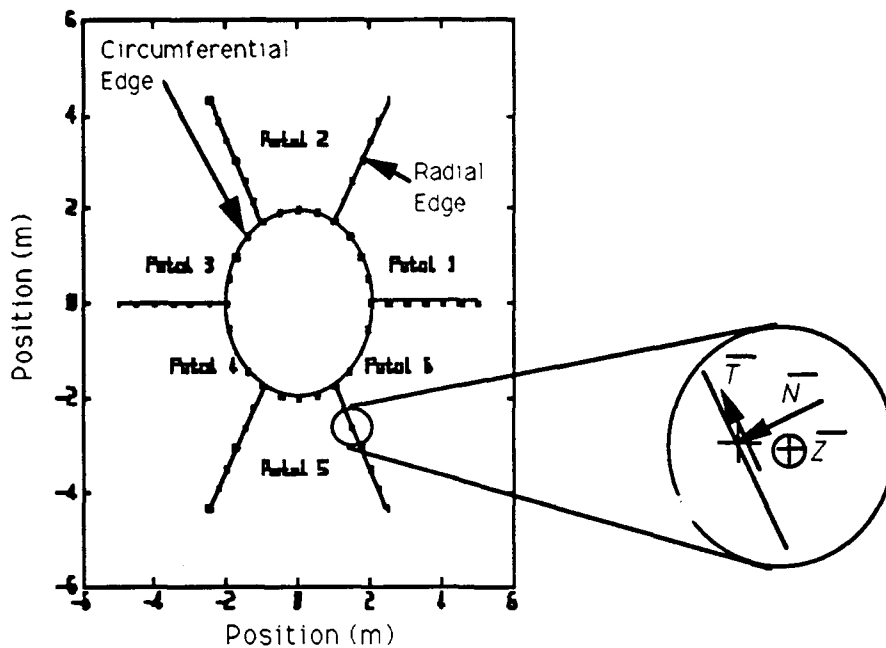


Figure 2.4: Sensor Positions - Edge Finite Element Nodes

Prospective edge sensor locations are related to the finite element nodes located on the edge of each DP as shown in Figure 2.4. These sensors measure displacements normal to the edge, displacements in a radial direction along the edge, and displacements in the  $z$ -direction. The number and location of the edge sensors is considered a design variable, and through analyses described below, the number of edge sensors required will be determined. There are 7 sensor locations per radial edge and 5 sensors per circumferential edge leading to 216 possible edge displacement measurements.

The figure sensor measures the wavefront error of each petal and interpolates these measurements to the surface node locations of the finite element model. Figure control using each DP is not addressed in this thesis.

## 2.3 Performance Requirements

Most optic system requirements are specified in terms of a wavelength error over the aperture of the optic. The deformable mirror system is to have a corrected wavefront figure of  $\lambda/10^1$ . This means that the "rms figure" of the deformable mirror system cannot exceed  $\lambda/10$ , where  $\lambda$  specifies the wavelength of the laser used in the measurement source. This figure control requirement is a nearly static requirement ( $\leq 0.1Hz$ ).

<sup>1</sup>  $\lambda$  is assumed to be  $6328 \text{ \AA}$ , the wavelength of a He-Ne laser. The requirement is based on specifications of many current systems using the He-Ne laser only as a diagnostic tool.

Based on the above performance specification, norm bounds must be generated to apply  $H_2$  and  $H_\infty$  control system synthesis. The performance specification is interpreted as the “rms figure” of the optic, which can be expressed as the  $L_2$  norm [21]:

$$\|e\|_2 \leq \frac{63.28 \mu m}{10} \quad (2.2)$$

A discussion of norms is provided in Chapter 3.

## 2.4 State Space Model and Control System Block Diagram

The finite element model is manipulated to generate the standard state matrices, and the state equations are

$$\dot{x} = Ax + Bu \quad (2.3)$$

$$y = Cx + Du \quad (2.4)$$

The only dynamics modeled are associated with the six segment phasing actuators per DP which are modeled as springs. This produces a full rank  $D$  matrix. The time constants of the actuators are assumed much faster than the dynamics of the structural system. Therefore, the structure appears to act “instantaneously” to the inputs at the actuators. It is assumed that the bandwidth of the wavefront control system will not excite any modes except those modes associated with the segment phasing actuators. The natural frequencies of the actuators are less than 2 Hz. This implies that the structure is expected to act statically to inputs at the segment phasing actuators.

The states consist of the six positions and velocities associated with each DP, resulting in a 72 state model. There are 150 total force inputs in this model including the 144 figure and segment phasing actuators (108 + 36) and an additional 6 inputs for disturbances, one at the base of each DP.

Figure 2.5 shows the block diagram for the deformable mirror system. In this figure,  $K(s)^2$  refers to the compensator or controller,  $G(s)$  refers to the plant, and  $Se(s)$  refers to the segment phasing sensor. As can also be seen from Figure 2.5, the primary disturbance source analyzed occurs at the output of the plant,  $D_1(s)$ , and for this thesis, the reference input,  $R(s)$ , is set to 0.

The actual performance is the wavefront of the composite optic (center and 6 segments). The measure of the performance will be evaluated at a discrete set of points related to the Finite Element Model (FEM) of the DPs ( $E(s)$ ). These measurement locations are chosen to maximize the robust performance. Details of the methods used to determine the measurement locations are presented later.

---

<sup>2</sup>In this document, notation for the Transfer Function Matrices will be denoted by their dependence on  $s$  or  $\omega$ .

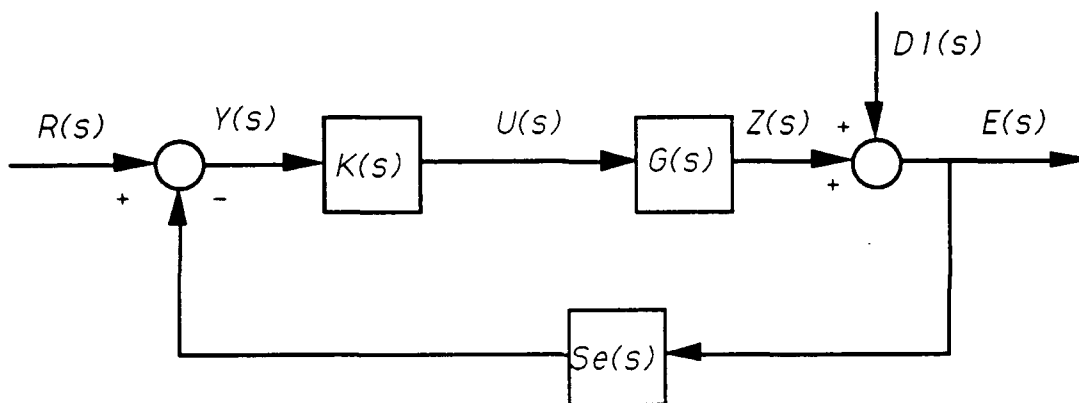


Figure 2.5: Block Diagram for the Deformable Mirror System

## Chapter 3

# Overview of Robustness Analysis Techniques

The purpose of this chapter is to give a brief exposition of robustness analysis techniques and the tools that will be used in this thesis. For a more detailed treatment of these properties, the reader is referred to [5,16].

### 3.1 Overview

The purpose of robust control is to design a controller to achieve a given level of performance in the face of a given level of uncertainty. A robust controller still meets the performance requirement because the effect of unknown or uncertain dynamics of the plant are incorporated into the synthesis of the controller. Two key developments enable the incorporation of uncertainty into the synthesis of a controller.

In 1976, Youla, Jabr, and Bongiorno [23,24] showed that it is possible to parameterize all stabilizing controllers for a particular system by searching over the space of *all stable* transfer functions. This parameterization guarantees that the resulting “optimal” controller will yield an asymptotically stable closed-loop system regardless of whether or not the plant is proper, stable, or minimum-phase. Later, Zames described a method of measuring performance in terms of the  $\infty$ -norm rather than the 2-norm [25]. While the quadratic or 2-norm can measure the energy of a signal of a system, the  $\infty$ -norm can be used to measure the “gain” of a system. The use of the  $H_\infty$  norm unifies performance and robustness analysis. This led to a new method of synthesizing controllers known as  $H_\infty$  control.

These two developments provided a framework for Doyle, who developed a powerful tool for testing “robust stability” and “robust performance” in 1982 [6] called the structured singular value or  $\mu$ . Using the  $H_\infty$  performance objective and norm bounded uncertainties, Doyle exploited the structure of the uncertainty and, using a variation of the small-gain theorem, developed  $\mu$  as a

nonconservative measure of robust performance.

With these developments and some enhanced computational algorithms, it is possible to express a performance requirement, establish bounds on the uncertainty, and synthesize a controller to meet the performance requirement. If no controller can be found that meets the performance requirement, a trade-off between the requirements and the uncertainty is necessary. In other words, if the control requirement cannot be satisfied, the control designer either needs to lower the performance specifications, or learn more about the system in order to lower the uncertainty bounds.

The remaining sections of this chapter describe the performance analysis tools (the  $H_2$  norm and the  $H_\infty$  norm) and the robust stability concepts.

## 3.2 Performance Analysis Tools - Transfer Function Norms

Performance analysis can involve many different concepts depending on the system analyzed and the performance requirement. If an error signal is to be minimized for disturbances having a fixed power-spectrum, a quadratic minimization of the rms error is appropriate. This type of problem occurs if a disturbance source is steady, i.e. 60 Hz noise in power supplies. For this particular case,  $H_2$  or Linear Quadratic Gaussian (LQG) methods are appropriate. In other cases, the disturbance spectra may include a class of signals, including impulses and narrow-band signals of various frequencies. For this class of problems, the minimization of the system gain is appropriate. In effect, the minimization of the system gain corresponds to minimizing the maximum response over all disturbances in a class of disturbance spectra. This minimization involves the induced norm, and is commonly referred to as  $H_\infty$  optimal control. This section details the  $H_2$  and  $H_\infty$  norms used in control system analysis.

### 3.2.1 Definition of the $H_2$ Norm

This section provides an overview of the use of the  $H_2$  norm in control system analysis and synthesis. All developments in this section are shown without proof. For a more detailed description, the reader is referred to [5].

The normed vector space  $(L_2^n, \|\cdot\|_2)$  is defined as the set of square-(Lebesgue) integrable functions such that

$$L_2^n = \{f | f : \mathfrak{R} \rightarrow \mathfrak{R}^n, \int_{-\infty}^{\infty} f^T(t)f(t)dt < \infty\}$$

and the norm is defined as

$$\|f\|_2 = \left( \int_{-\infty}^{\infty} f^T(t)f(t)dt \right)^{\frac{1}{2}} \quad (3.1)$$

Physically, this set is used to model finite energy signals. The subspace of  $L_2^n(\mathfrak{R})$  consisting of the

functions that satisfy [8]

$$f(t) = 0, \quad t < 0$$

is defined by  $L_2^n(\mathfrak{R}_+)$ . It can be shown that the Laplace transform of every signal in  $L_2^n(\mathfrak{R}_+)$  and denoted by  $\mathcal{L}(L_2^n(\mathfrak{R}_+))$  exists and satisfies

1.  $f(s)^1$  exists for  $s \in \mathcal{C}_+$  and  $f$  is analytic in  $\mathcal{C}_+$
2.  $\sup_{\alpha > 0} \int_{-\infty}^{\infty} [f^*(\alpha + j\omega)][f(\alpha + j\omega)] d\omega < \infty$
3.  $\lim_{\alpha \rightarrow 0} f(\alpha + j\omega) = f(j\omega)$  exists almost everywhere and  $f \in L_2^n(j\mathfrak{R})$

where  $\mathcal{C}_+$  denotes the right-half  $s$ -plane.

As a consequence, the set  $\mathcal{L}(L_2^n(\mathfrak{R}_+))$  can be identified with the boundary value function  $f(j\omega)$ . The set of all functions that satisfy 1), 2), and 3) above is denoted by  $H_2^n(\mathcal{C}_+)$  and the identification is made that

$$H_2^n(\mathcal{C}_+) = \mathcal{L}(L_2^n(\mathfrak{R}_+))$$

Using this relationship between the  $L_2$  and  $H_2$  spaces, the vector  $H_2$  norm can be found from the application of Parseval's Theorem to Equation 3.1, yielding

$$\|f\|_2 = \left( \frac{1}{2\pi} \int_{-\infty}^{\infty} f^T(-j\omega) f(j\omega) d\omega \right)^{\frac{1}{2}} \quad (3.2)$$

For matrix transfer functions,  $G(j\omega)$ , the (operator)  $H_2$  norm of a transfer function is given by

$$\|G\|_2 = \left\{ \frac{1}{2\pi} \int_{-\infty}^{\infty} \text{tr}[G(j\omega)G^T(-j\omega)] d\omega \right\}^{\frac{1}{2}} \quad (3.3)$$

These two norms provide a base for the definition of the  $H_2$  problem.

### 3.2.2 $H_2$ Analysis

The  $H_2$  norm developed above can be directly applied to the deformable mirror system. The  $H_2$  problem is defined as finding the stabilizing controller  $K$  which minimizes the cost function

$$J = \frac{1}{2\pi} \int_{-\infty}^{\infty} \text{tr}[(T_{ed}(j\omega))(T_{ed}^*(j\omega))] d\omega \quad (3.4)$$

which is equivalent to an LQG problem [13]. This problem can be interpreted as minimizing the rms value of the output signal  $e$  when the system is driven by a white noise<sup>2</sup> disturbance  $d$ . In other words, the minimization is carried out against a fixed power spectral density. The solution of this minimization problem can be found using Riccati equations [1].

<sup>1</sup>With a slight abuse of notation, time domain functions and frequency domain functions are denoted by the same symbol. In areas where this notation is not straightforward, the dependence on time or frequency will be included.

<sup>2</sup>Through the addition of filters, "colored" noise inputs can be treated in the same manner.

Therefore, the  $H_2$  optimal control problem uses the  $H_2$  norm of the closed-loop transfer function between the disturbance inputs and the error vector in the design and analysis procedures. The disturbance input is specified as white noise with unit variance. Under these conditions, the minimization of the error vector through the minimization of the  $H_2$  norm of  $T_{ed}$  results in the optimal solution. As has been discussed above, there are many problems where the disturbances come from a class of spectra, and only a bound on the disturbance is known. This fact motivated the  $H_\infty$  problem.

### 3.2.3 $H_\infty$ Analysis

As seen in Section 3.2.1, the  $H_2$  norm provides a means of determining the average power of the error function,  $T_{ed}(j\omega)$ . A different measure on the error function is the maximum amplification of the energy of a system. The tool that provides this measurement is known as the  $H_\infty$  norm. This section provides the definition of the  $H_\infty$  norm.

To facilitate the definition, assume that the vector signal,  $e(j\omega) \in H_2^m$ , is generated from an input vector signal,  $d(j\omega) \in H_2^n$ , and the transfer function matrix,  $T_{ed}(j\omega)$ . If this transfer function matrix,  $T_{ed} : H_2^n \rightarrow H_2^m$  is applied to the input signal, the maximum gain from the disturbance input,  $d(j\omega)$ , to the error output,  $e(j\omega)$  can be determined. This maximum gain forms the definition of the  $H_\infty$  norm.

$$\|T_{ed}\|_\infty = \max_{\|d\|_2 \neq 0} \frac{\|T_{ed}d\|_2}{\|d\|_2} = \max_{\omega \in \mathfrak{R}} \bar{\sigma}(T_{ed}(j\omega)) \quad (3.5)$$

Applying this to the deformable mirror system, again the requirement is to reduce the 2 norm of the error vector,  $e$ . For the  $H_\infty$  norm case, we search over all frequencies for the maximum gain of the transfer function  $T_{ed}$ . By minimizing the  $H_\infty$  norm, we are reducing the 2 norm of the error vector,  $e$  (See Appendix A). The  $H_\infty$  norm can also be used with the small gain theorem to unify stability robustness concepts.

## 3.3 Robust Stability Concepts

Robust stability implies that a closed-loop system is stable for a set of open-loop plants. Using the Nyquist stability tests in a multivariable setting, it is desired to determine some conditions that will assure system stability given uncertainty. This section provides an overview of the robust stability problem through the formulation of the small gain problem. Then, through application of a small  $\mu$  theorem, the structured singular value is developed as a tool that can be applied to determine performance robustness. All results are provided without proof. For more details, the reader should consult [5,8,16].

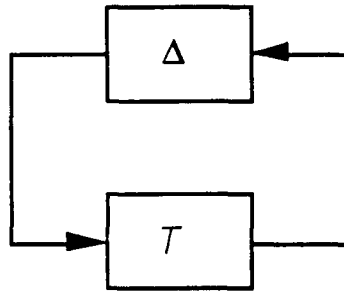


Figure 3.1: Block-Diagram for Small Gain Theorem

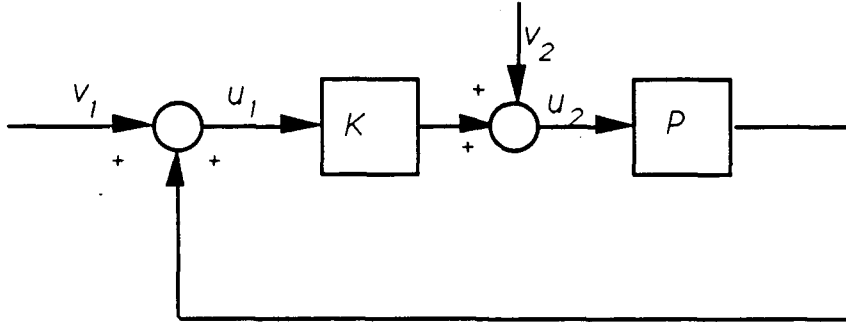


Figure 3.2: Feedback System for Stability Analysis

### 3.3.1 Small Gain Concepts

The small gain theorem gives conditions under which a “bounded-input” produces a “bounded-output”. Consider the block diagram shown in Figure 3.1, where  $T$  represents some matrix transfer function and  $\Delta$  represents an unstructured (full block) uncertainty. The motivation for the small gain theorem is to determine conditions on  $\Delta$  that will make the nominally stable  $T$  unstable. Therefore, the small gain theorem looks at the affect of an unstructured perturbation on the stable system  $T$ . The small gain theorem states that a sufficient condition for internal stability, given that  $\Delta$  is stable, is

$$\|\Delta T\|_{\infty} < 1 \quad (3.6)$$

The small gain theorem can be used to determine internal stability properties of a system. Consider the feedback system shown in Figure 3.2, where the plant is represented by  $P$ , and the controller is denoted by  $K$ . The feedback system is said to be internally stable if the four transfer functions from  $v_1$  and  $v_2$  to  $u_1$  and  $u_2$  are stable.

Extending the small gain theorem to robust stability, a multiplicative output uncertainty is added to the plant as shown in Figure 3.3. This defines a new plant

$$\tilde{P} = P + \Delta P$$



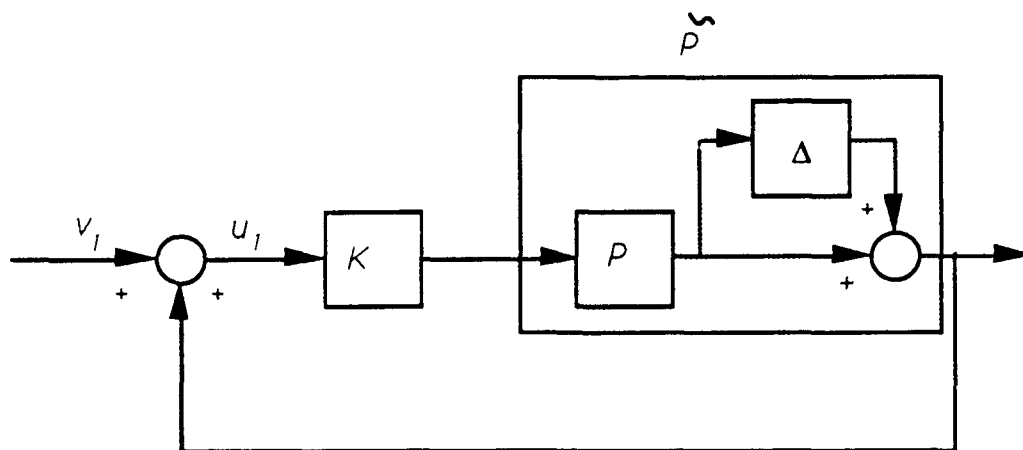


Figure 3.3: Feedback System Including Uncertainty Block

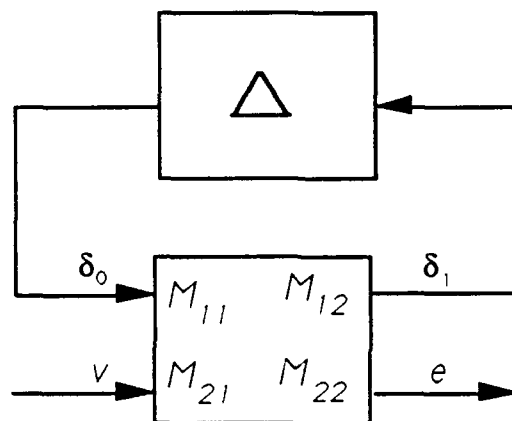


Figure 3.4: Reduced Block Diagram for Robust Stability Analysis

The only information that is known about the uncertainty,  $\Delta$ , is that it is bounded from above. Without loss of generality, this bound is often selected as unity, so that

$$\bar{\sigma}(\Delta(j\omega)) \leq 1, \quad \forall \omega \quad (3.7)$$

It will be shown later that if this is not the case, weighting functions can be used in order to assure that the uncertainty,  $\Delta$ , satisfies Equation 3.7. The only information known about the uncertainty is the bound. Therefore, the uncertainty is called an unstructured uncertainty. The question posed is, "How large can  $\Delta$  be so that internal stability is maintained?" Through manipulation of the block diagram, a reduced block diagram is obtained as shown in Figure 3.4. This is a generalized structure used for robustness analysis. With this structure, the following theorem can be stated [16].

**Theorem 3.1:** [Morari [16], p. 238] *Assume that  $M$  and  $\Delta$  are stable. Then the closed-loop system of Figure 3.4 is stable for all perturbations  $\Delta$  ( $\bar{\sigma}(\Delta) \leq 1$ ) if and only if one of the following*

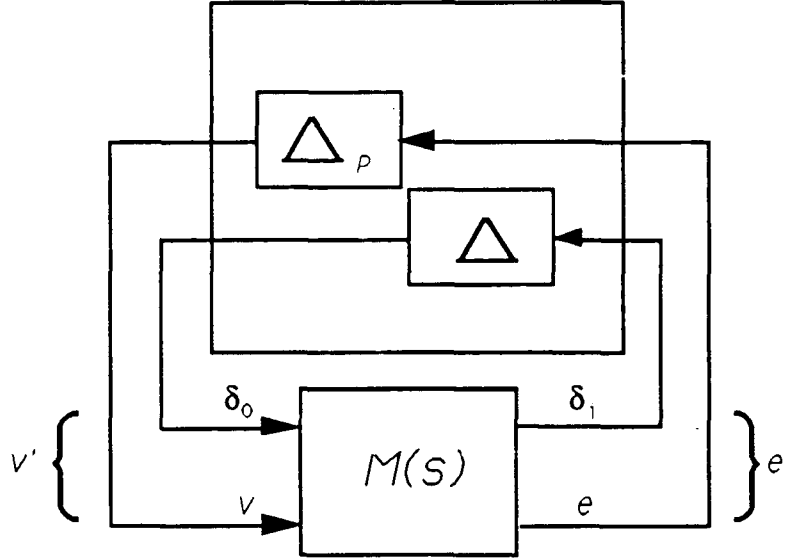


Figure 3.5: M- $\Delta$  Block Diagram for Robust Performance Analysis

three equivalent conditions is satisfied

$$\det(I - M_{11}\Delta(j\omega)) \neq 0, \quad \forall \omega, \forall \Delta \ni \bar{\sigma}(\Delta) \leq 1 \quad (3.8)$$

$$\Leftrightarrow \rho(M_{11}\Delta(j\omega)) < 1, \quad \forall \omega, \forall \Delta \ni \bar{\sigma}(\Delta) \leq 1 \quad (3.9)$$

$$\Leftrightarrow \bar{\sigma}(M_{11}(j\omega)) < 1, \quad \forall \omega \quad (3.10)$$

$$\Leftrightarrow \|M_{11}\|_{\infty} < 1 \quad (3.11)$$

where  $\rho(\cdot)$  denotes the spectral radius.<sup>3</sup>

**Proof:** See [16].

Utilizing this theorem for robust stability, the next step is to incorporate the performance requirements in order to determine a robust performance measure. This can be done by adding a fictitious performance “uncertainty” block [6]. When including this performance block, we add “structure” to the uncertainty block,  $\Delta$ .

### 3.3.2 Structured Singular Value- $\mu$

If we take Figure 3.4 and look specifically at the performance map from  $v$  to  $e$ , a performance block can be connected between  $e$  and  $v$  such that Figure 3.5 results. If we now combine the inputs,  $\delta_0$

<sup>3</sup>The spectral radius is defined as

$$\rho(M) \equiv \max_i |\lambda_i(M)|$$

and  $v$ , and the outputs,  $\delta_i$  and  $e$ , into two composite vectors,  $v'$  and  $e'$ , it is obvious that we again have a reduced block diagram of the form of Figure 3.4, where

$$\Delta_M = \begin{bmatrix} \Delta & 0 \\ 0 & \Delta_P \end{bmatrix} \quad (3.12)$$

Again using the small gain theorem, we can state the performance robustness requirement in terms of the stability robustness problem analyzed in Section 3.3.1. There is one slight problem to just repeating the analysis in Section 3.3.1. As stated above, the uncertainty  $\Delta$  used in the analysis of Section 3.3.1 is considered an unstructured uncertainty. Obviously, Equation 3.12, details a structure to  $\Delta_M$ . This structure can be incorporated through application of the structured singular value. Using the following definition of  $\mu$  will allow a variation of the small gain theorem to be applied [16].

**Definition 3.1:** (Morari [16], p. 249) *The function  $\mu(M)$ , called the Structured Singular Value (SSV) is defined such that  $\mu^{-1}(M)$  is equal to the smallest  $\bar{\sigma}(\Delta)$  needed to make  $(I - M\Delta)$  singular. If no  $\Delta$  exists such that  $\det(I - M\Delta) = 0$ , then  $\mu(M) = 0$ .*

Utilizing this definition, a test for robust stability and robust performance can be formulated. Before presenting the theorem, let us define the set,  $X_\nu$ , of all complex perturbations with a specific block diagonal structure and spectral norm less than  $\nu$ .

$$X_\nu = \{\Delta = \text{diag}\{\Delta_1, \Delta_2, \dots, \Delta_m\} | \bar{\sigma}(\Delta_i) \leq \nu\}$$

By selecting  $\Delta \in X_\nu$ , it can be easily shown that robust stability is guaranteed via the small gain theorem if and only if

$$\begin{aligned} \det(I - M\Delta) &\neq 0 \quad \forall \Delta \in X_\nu \\ \iff \rho(M\Delta) &< 1 \quad \forall \Delta \in X_\nu \end{aligned}$$

or robust stability will be guaranteed only if

$$\nu < \bar{\sigma}^{-1}(M) \quad (3.13)$$

It should be noted that Equation 3.13 is only a sufficient condition because in the original small gain theorem, the perturbation set includes all  $\Delta$  such that  $\bar{\sigma}(\Delta) \leq 1$ . Here, we have restricted the set of  $\Delta$  to  $X_\nu$ . This condition can be arbitrarily conservative. The "small  $\mu$ " theorem determines a new bound for robust stability.

**Theorem 3.2:** [Morari [16], p. 249] *Assume that  $M$  and  $\Delta$  are stable. Then the closed-loop system is stable for all perturbations  $\Delta \in X_{\nu=1}$  if and only if*

$$\mu(M(j\omega)) < 1, \quad \forall \omega \quad (3.14)$$

**Proof:** See [16].

By concentrating on the block,  $\Delta_i$ , that makes the quantity  $\det(I - M\Delta)$  singular, the structured singular value utilizes the small gain theorem while taking advantage of the structure. The basic limitation is that

$$\bar{\sigma}(\Delta_i) \leq 1, \quad \forall \omega$$

Through the use of weighting functions, this condition can always be satisfied (Chapter 6). Therefore, by establishing the performance as another  $\Delta$  block, the test for robust stability actually becomes a test for robust performance. The structured singular value is used extensively in Chapter 6 as a test for robust performance of the deformable mirror system.

An important point to note when studying the small  $\mu$  theorem is the fact that the system inputs and system outputs are normalized (i.e.  $\|v'\|_2 \leq 1$  and  $\|e'\|_2 \leq 1$  in Figure 3.5). The fact that the normalization is with respect to unity allows some straightforward observations of the "size" of  $M$ . If  $\|M\|_\infty > 1$ , the system will amplify disturbances in the error vector. In contrast, the system will attenuate disturbances and remain stable if  $\|M\|_\infty \leq 1$ . The structured singular value provides a non-conservative measurement of the "size" of  $M$ .

The actual calculation of  $\mu$  is done via bounds on  $\mu$ . It is shown in [16] that the structured singular value is bounded from above by the maximum singular value of a weighted matrix and bounded from below by the spectral radius of a weighted matrix. Many of the tests shown in Chapter 6 refer to these bounds in order to show the conservativeness of using the singular value in cases where the uncertainty block has structure. The bounds are given below without proof.

$$\rho(UM) \leq \mu(M) \leq \bar{\sigma}(DMD^{-1}) \quad (3.15)$$

The weighting matrices  $U$  and  $D$  can be adjusted to yield a tight bound on the calculation of  $\mu$ . In Equation 3.15,  $U$  is a unitary matrix with the same block diagonal structure as  $\Delta$ , and  $D$  is a diagonal matrix  $D = \text{diag}\{d_i I_i\}$  where the size of each  $I_i$  is equal to the size of the blocks,  $\Delta_i$ .

## Chapter 4

# Problem Statement

This chapter defines the issues and the goals for the deformable mirror system. As stated earlier, the primary goal is to choose the number and location of sensors and design a controller to meet a robust performance specification. In attaining this goal, several issues need to be resolved and several subgoals are established in an attempt to extend the usefulness of the control synthesis methods to other large-scale problems. This chapter provides a “road-map” of the steps used in developing a robust controller for the deformable mirror system.

### 4.1 Issues Addressed

This section details the issues involved in developing a robust controller for the deformable mirror system. In addition to the issue of meeting the performance requirements, there are several issues raised in dealing with an integrated structure of the size of the deformable mirror system. This concerns the issue of the simulation of the deformable mirror system models. The performance of the controllers synthesized is evaluated through the use of computer simulations, so the size and numerical condition of the problem figures prominently. Finally, decentralized control is addressed in reference to the deformable mirror system.

#### 4.1.1 Simulation Issues

As described in Chapter 2, the deformable mirror system has a complex model representation. With 72 states, 36 inputs, and a possibility of 216 sensor measurements, performing simulations with this model is not a trivial task. The physical size of the model will make the computations burdensome, and numerical conditioning problems are prevalent. The simulation and design software package, *MATLAB* [4], is used exclusively for the simulations. A majority of the *MATLAB* algorithms used have been developed for numerical robustness, and this increases the confidence in the simulation results. Still, the application of the analysis tools described in Chapter 3 can have numerical

difficulties in calculating the performance. Chapter 6 details the actual synthesis of the controllers for the system models which includes the appending of states of weighting functions to the 72 plant states. This greatly increases both the size and complexity of the model, and simulations become even more difficult. The physical size of the model is an issue that faces many large simulations, and a natural attempt to minimize the size of the model is to concentrate on a subset of the model and attempt to extend the results to the full model.

If the deformable mirror system is examined in an attempt to model a subsystem and extend the results to the full model, an obvious subsystem is a single DP. Each DP has six separate actuators for inputs and the control action can be thought of as regulating positions and velocities in three translation and three rotation modes. Therefore, the model of a single petal will contain only 12 states, 6 inputs, and a possibility of 57 sensor measurements (7 sensor locations along each radial edge and 5 sensor locations along the circumferential edge). A conjecture is made that a single petal model can be simulated to determine sensor locations and robust performance, and then these results can be applied to the full 6 petal model. Each sensor measures wavefront error relative to a specific edge in a specific direction. Therefore, a simulation of one petal can be thought of as a special case of the full model where only one petal is perturbed. With the highly integrated structure of the deformable mirror system, the results from the single petal model scaled in one case and did not fully scale in a second case. Chapter 6 compares simulations for a single petal model and two cases of a full model.

#### **4.1.2 Performance Issues**

From the earliest years of control synthesis, a fundamental trade-off has been made: performance versus uncertainty. The performance requirement for the deformable mirror system is to be met in the presence of uncertainty. If this requirement cannot be met, two choices exist. Either the performance requirement needs to be loosened, or the knowledge of the plant model needs to be improved to lessen the uncertainty. With the realization that control synthesis and simulation can provide a large amount of information to system designers before the system is built, control theory is beginning to be applied much earlier in the system design process. Therefore, the trade-off for the deformable mirror system is that the knowledge of the plant will need to be increased in the event that robust performance cannot be achieved.

The uncertainty sources that can occur in the deformable mirror system include uncertainty in the modeling of the plant, uncertainty in the sensors, uncertainty in the force actuators, uncertainty in the tolerance of physically building the deformable mirror system, etc. This analysis, though, only addresses uncertainty in the sensors. The quality of the sensors can greatly affect the closed-loop performance, and different sensors could be suggested should the closed-loop performance

not meet the specification. It is possible, through methods explained in Chapter 6, to model the sensor accuracy as a function of frequency. This makes it possible to model a sensor with frequency characteristics of a high degree of accuracy over low frequencies and poor accuracy over high frequencies. This same frequency dependence is also present in the deformable mirror system dynamic model where the plant model is also more accurate over low frequencies than at high frequencies.

### 4.1.3 Control Design Issues

$H_2$  controllers are designed to minimize the quadratic norm of an error function with inputs of known power spectrum as discussed in Chapter 3. This minimization over a fixed disturbance spectra has been widely used over the past 30 years. One weakness of  $H_2$  controllers can be observed when the knowledge of the input power spectrum is unknown except for a bound. For this particular problem,  $H_\infty$  controllers are developed.  $H_\infty$  controllers are still designed to minimize the quadratic norm of an error function, but the power spectra of the disturbances is not known. The disturbances belong to a class of spectra for the  $H_\infty$  controller solution.

Whereas the  $H_2$  controller provides a condition on the  $H_2$  norm of the transfer function from disturbance inputs to outputs, the  $H_\infty$  controller provides a condition on the *induced 2-norm* or  $H_\infty$  norm. The power spectra of a disturbance source does not need to be known, only the fact that the disturbance source is bounded. This intuitively leads to a more robust controller, because the controller is developed for a set of "unknown" disturbances.  $H_2$  controllers function on the nominal plant and minimize the error signal based on a disturbance source with a fixed spectrum, while  $H_\infty$  controllers function on an uncertain plant and minimize the error based on a minimization of the maximum system gain for a set of disturbances. To achieve this additional robustness, though,  $H_\infty$  controllers tend to sacrifice performance.

$H_\infty$  control synthesis is used for the deformable mirror system. The goal of this thesis is to synthesize a controller to meet the robust performance specification. Using a deterministic development of uncertainty in the sensor, a general bound is established. This establishes the problem in a format suitable for  $H_\infty$  control synthesis.  $H_\infty$  control synthesis was chosen for the additional flexibility of incorporating the uncertainty into the synthesis procedure.

### 4.1.4 Decentralized Control Issues

With the prospect of increasingly complex systems, there is a need to develop and apply decentralized control techniques. The size and integrated nature of the structure of the deformable mirror system provides an example for decentralized control. The definition of decentralized control as used here means that the controller is block diagonal. This is done by searching for a block diagonal

plant structure and treating the off-diagonal portion of the plant as an uncertainty. Then separate controllers can be designed for the block diagonal portions of the deformable mirror system plant, and the overall control action is assured to be stable. This type of decentralized control has a nice property in that a subsystem can fail yet the overall control system will remain stable. It is also important to determine the effect on performance from the use of a decentralized controller when compared to a centralized controller.

In order to design a decentralized controller, a decentralized plant structure needs to be identified. This structure takes the shape of a block-diagonal plant, where subsystems function independently. Each subsystem relies on a subset of the total inputs and outputs. The criteria for identifying a decentralized structure includes a requirement that the system remain stable if a subsystem were to fail. The method of choosing a decentralized structure is very important, and the ease in testing several potential decentralized structures is critical in a model the size of the deformable mirror system. Consider the issue of selecting input-output pairs of a system with  $n$  candidate inputs and  $n$  candidate outputs. The number of distinct subsystems with  $m$  inputs and  $m$  measurements that can be selected for the closed loop control is [18]

$$\binom{n}{m}^2$$

where

$$\binom{n}{m} = \frac{n!}{m!(n-m)!}$$

This means that the total number of distinct square subsystems of an  $n \times n$  system is

$$\sum_{m=1}^n \binom{n}{m}^2$$

where each subsystem corresponds to a selected subset of the candidate measurements and inputs. For the deformable mirror system, with 36 inputs and 36 outputs (assuming 36 sensors are chosen from the possible 216), the number of distinct subsystems is in excess of  $4 \times 10^{20}$ .

With this outrageously large number of distinct subsystems, simple tests for decentralizability need to be used. Even with these simple tests, all of the possible subsystems are not tested in this thesis. The tests that are used provide a basis for "narrowing down" the number of possible candidate subsystems to a manageable subset. Stronger tests are then applied to this subset to determine if decentralized control is a valid alternative for the deformable mirror system.

With the above issues, separate subgoals are established to determine items of interest. The desire is to develop a framework that can be generally applied to other large structural systems.



## 4.2 Goals

In satisfying the primary goal of developing a robust controller, several subgoals are established to address the issues described above. These subgoals identify specific areas that are addressed in the following chapters and attempt to generalize the results that will be presented in Chapter 6 to similar systems. The generalizations are not mathematically proven and are not rigorous. They only provide a framework to begin asking the correct questions and attempting to understand the answers.

The first subgoal that is established is to develop a thorough analysis of the single petal model, and to apply this knowledge to the full model. This is a critical step in this effort. As discussed earlier, size limitations make analysis of the full model extremely difficult. If the analysis completed on the single petal can be "scaled" to the full model, then it is possible to complete a great deal of the design effort on a subset of the full model, and apply the results directly. This may not be possible, though. The first subgoal, therefore, is to determine if this "scaling" of single petal results to the full model is valid.

The second subgoal is to determine the "optimal" sensor selection method. The analysis will show an extreme sensitivity to the location of the sensors for the deformable mirror system. A method needs to be developed to select the sensor locations. This method can range from something as simple as attempting to make the problem as well conditioned as possible to an analysis of the robust performance for different sensor combinations. As will be shown in Chapter 6, robust performance of the deformable mirror system cannot be achieved for the selection of sensor locations that seem to be intuitively correct. The mathematical tools developed in Chapter 3 along with open-loop properties described in Chapter 5 begin to provide a framework for sensor selection.

The final subgoal is to determine a suitable decentralized control structure. The need to simplify the deformable mirror system model to a model that can be analyzed and implemented is a prevalent theme of this work. The ability to decentralize the deformable mirror system into more manageable pieces would represent a significant accomplishment. Therefore, several tests are applied in an attempt to identify a valid decentralized control structure. However, the highly integrated nature of the deformable mirror system make this subgoal unattainable for the full model.

## 4.3 Conclusions

The primary task of developing a robust controller for the deformable mirror system can provide several subtasks that will provide a method to generalize the results of this analysis to different problems. Many multivariable control problems have difficulties with the physical dimension of the system model or a method to select the number of sensors required to meet the performance

requirement. It is intended that solutions of these issues for the deformable mirror system will provide a starting point for analysis of similar systems. As more knowledge is gained as to how these issues have been resolved for different types of systems, a more mathematical treatment can follow.

## Chapter 5

# Open-Loop Plant Analyses

The analysis of the open-loop plant model of the deformable mirror system involves four main areas. The first area is the selection of sensor locations based on the physics of the model. This simple analysis provides a starting point in determining the number of sensors required to adequately meet the performance requirements. The second area of analysis uses the information of the number of sensors required to find a method of placing these sensors. For this analysis, the sensors were placed to reduce the condition number of the open-loop plant at d.c. Taking advantage of the dynamics incorporated in the model, controllability and observability tests were used to determine if the sensor selection meets the requirements for control synthesis. Model balancing and possible model reduction is also discussed. The final analysis addresses the open-loop poles and zeros and potential impacts on closed-loop design.

### 5.1 Basic Sensor Selection Requirements

In order to adequately control the deformable mirror system, all degrees of freedom need to be determined. Each direction and rotation of each DP and combinations need to be known in order to develop a control signal to account for this motion. In a rigid body sense, this requirement is straightforward. The number of sensors required is the number of degrees of freedom that need to be controlled. For a dynamic model, there is a possibility that the dynamics will provide additional information so that the number of sensors required can be reduced. The analysis completed in this section uses the rigid body as a baseline, and then a reduced sensor placement is tried. In the following sections, this reduced sensor placement is found to meet all of the requirements for synthesis of a controller. The dynamics of the model allowed a reduction in the number of sensors required.

A single petal contains 6 force actuators capable of moving the DP in 6 Degrees-of-Freedom (DOF): translations in the  $x$ -axis,  $y$ -axis, and  $z$ -axis; and rotations about the  $x$ -axis,  $y$ -axis, and

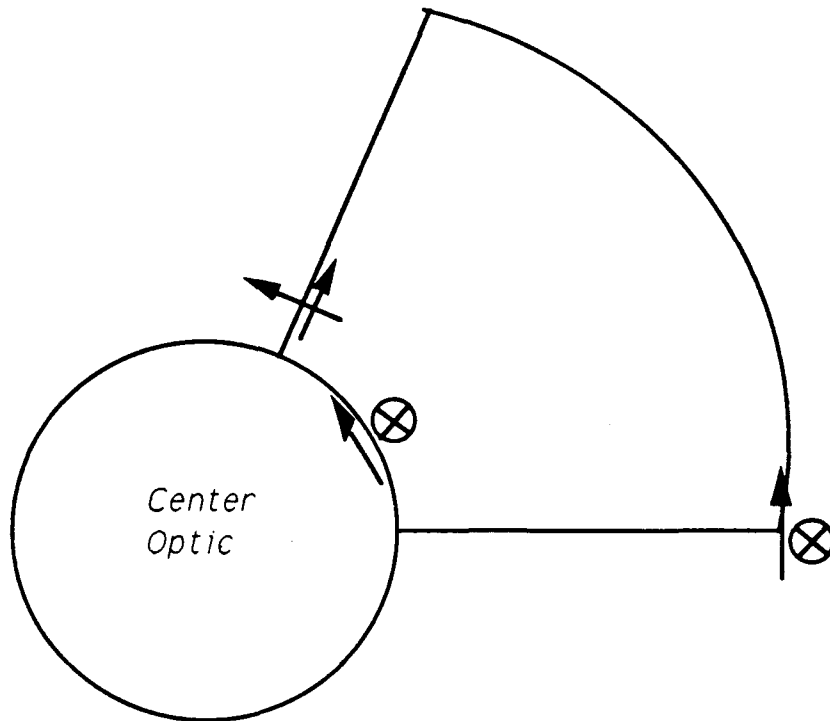


Figure 5.1: Example of Sensor Locations - Single Petal Model

$z$ -axis. Because each sensor measures the relative difference between petals in one-axis only, a minimum of 6 sensors measuring the 6 DOF are required in a rigid body sense to adequately determine the complete position of the single DP. Therefore, 6 sensors are chosen for the single petal model as the minimum number of sensors required. An example of 6 sensors for the single petal model is shown in Figure 5.1, where arrows denote the axes sensed and  $\otimes$  denotes a displacement into the page ( $z$ -direction).

The selection of sensors for the full model case is not quite as straight forward. One simple way is to extend the 6 sensors per petal to the entire model. This would produce 36 sensor locations. Figure 5.2 shows possible sensor locations for the full model based on 36 sensors. If no dynamics were included in the deformable mirror system model, 36 sensors would be the minimum number of sensors required to measure all of the associated degrees of freedom. Because a dynamic model of the structure is available, the possibility of finding a suitable structure with less than 36 sensors exists. The initial method used to find a candidate system was to again look at the full model with 36 sensors and attempt to reduce the sensors in a logical fashion.

Through studying Figure 5.2, a candidate sensor selection system would be to remove some of the sensors along the radial edge. Trying to alternate tangential and normal sensors, Figure 5.3 is developed. This results in a 24 sensor model. As will be shown below, this model meets the requirements for controller synthesis.

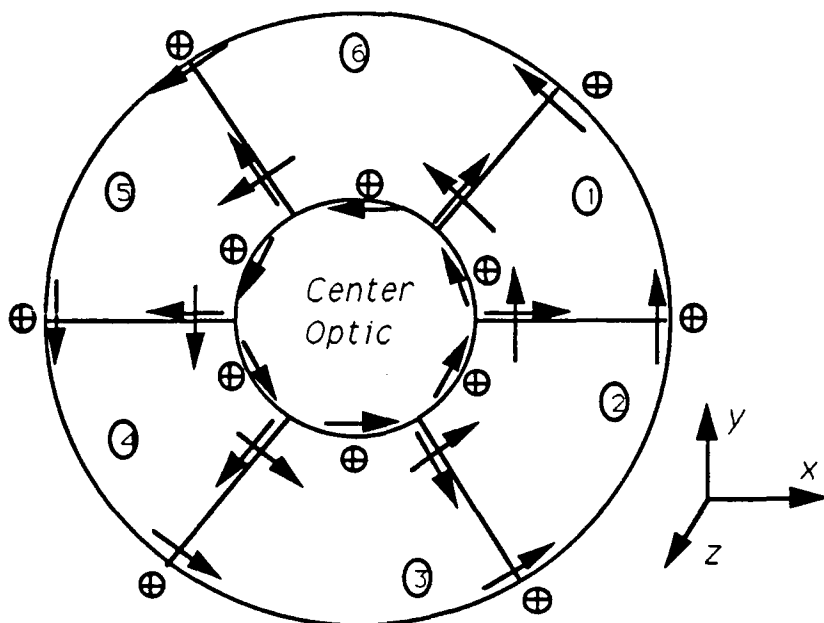


Figure 5.2: Example of Sensor Locations - Full Model with 36 Sensors

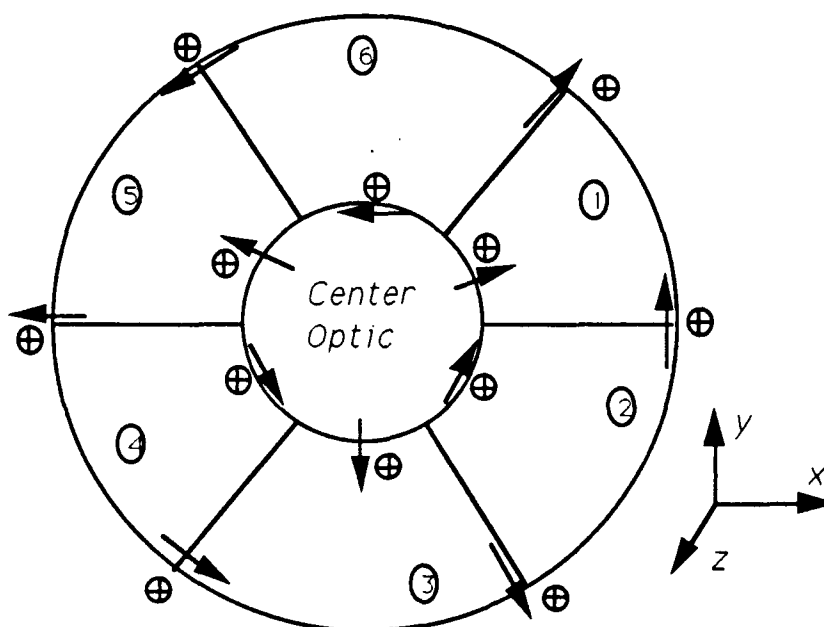


Figure 5.3: Example of Sensor Locations - Full Model with 24 Sensors

For purposes of decentralized control, it is still useful to analyze the system with 36 sensors, and therefore, this system will be addressed in the remaining open-loop analyses as well as Section 6.3, ( $H_\infty$  Controller Solution). The single petal model and the full model with 24 sensors will form the baseline of the closed-loop synthesis and analyses.

## 5.2 Plant Condition Number

Generally, linear multivariable plants with a “large” condition number are inherently difficult to control [17]. Minimizing the condition number of the plant is sound engineering practice, and this section provides the effort to assure that the plant is well-conditioned.

The condition number is defined by

$$\kappa\{G(j\omega)\} = \frac{\bar{\sigma}(G(j\omega))}{\underline{\sigma}(G(j\omega))} \quad (5.1)$$

where

$$\bar{\sigma}(G(j\omega)) = \text{Maximum Singular Value of } G(j\omega)$$

$$\underline{\sigma}(G(j\omega)) = \text{Minimum Singular Value of } G(j\omega)$$

The condition number reflects the coupling of inputs to outputs. Well-conditioned means that the different input directions produce similar magnitude outputs. There is no one channel that requires a significant increase in gain in order to affect the output. Ill-conditioned means,

$$\kappa\{G(j\omega)\} \gg 1$$

Therefore, an ill-conditioned system is strongly dependent on the input direction. To achieve tight control of an ill-conditioned plant, the controller should compensate for the strong directionality by applying large inputs in the directions where the plant gain is low and small inputs in the directions where the plant gain is large. This suggests a controller similar to  $G^{-1}$  [20]. Due to uncertainty, the direction of the large input to the low plant gain may not correspond exactly, and there is a possibility of amplifying the input signal to a much greater degree than modelled. This often leads to instability and poor performance.

The sensor locations and directions were selected to minimize the condition number of the plant at d.c. A search method was developed that selected sensors based on the minimization of the condition number of the plant. An initial guess was input into the iteration process, and the iteration process continued until the condition number no longer changed. For the single petal model, Figure 5.4 shows the sensors selected that yield the lowest condition number, and Figure 5.5 shows a plot of the condition number for sensors shown in both Figure 5.1 and Figure 5.4. Note that the sensor locations shown in Figure 5.4 are not symmetric. Sensor 1 is not located at the

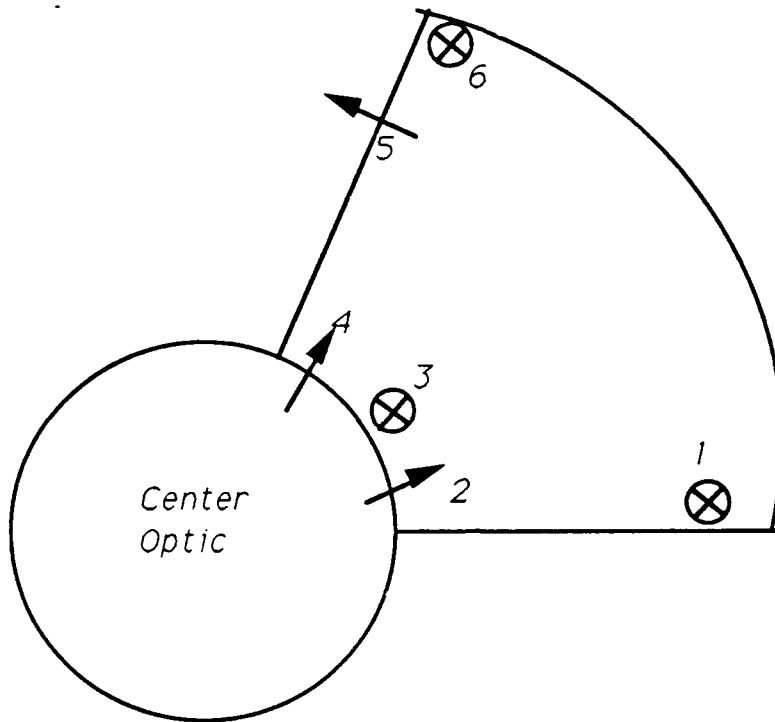


Figure 5.4: Sensor Locations Chosen-Single Petal Model

edge of the DP but is located one finite element node in from the edge toward the center optic. The best conditioned single petal plant model does not have any two sensors located at the same finite element node. Figure 5.5 shows that the single petal is well conditioned for the frequency range of interest.

Figure 5.6 shows the open-loop singular value plot of the single petal model. This figure shows the relatively “flat” open-loop response of the single petal model to approximately 2 Hz, where the resonant mode of the segment phasing actuators appear. The desired bandwidth of the system, as described in Section 2.3, should maintain performance accuracy to a frequency of 0.1 Hz. This is an order of magnitude below the resonance seen in Figure 5.6, and it will be shown later that this requirement is difficult to meet for the full model.

Using the same iterative process described above, the sensors that yield the best conditioned plant for the full model, 36 sensors, were chosen and are shown in Figure 5.7. Note that the minimum plant condition number again results from a selection of sensors with no apparent symmetry. The condition number of the sensors from both Figure 5.2 and Figure 5.7 are shown in Figure 5.10. As can be seen, the condition number increases drastically at  $\approx 2$  Hz. The disturbance rejection requires the performance to be maintained to frequencies of 0.1 Hz. Therefore, the condition number of the full model with 36 sensors at 2 Hz should have minimal effect on the control design.

The same procedure was repeated for the full model, 24 sensor case, and the sensors are shown

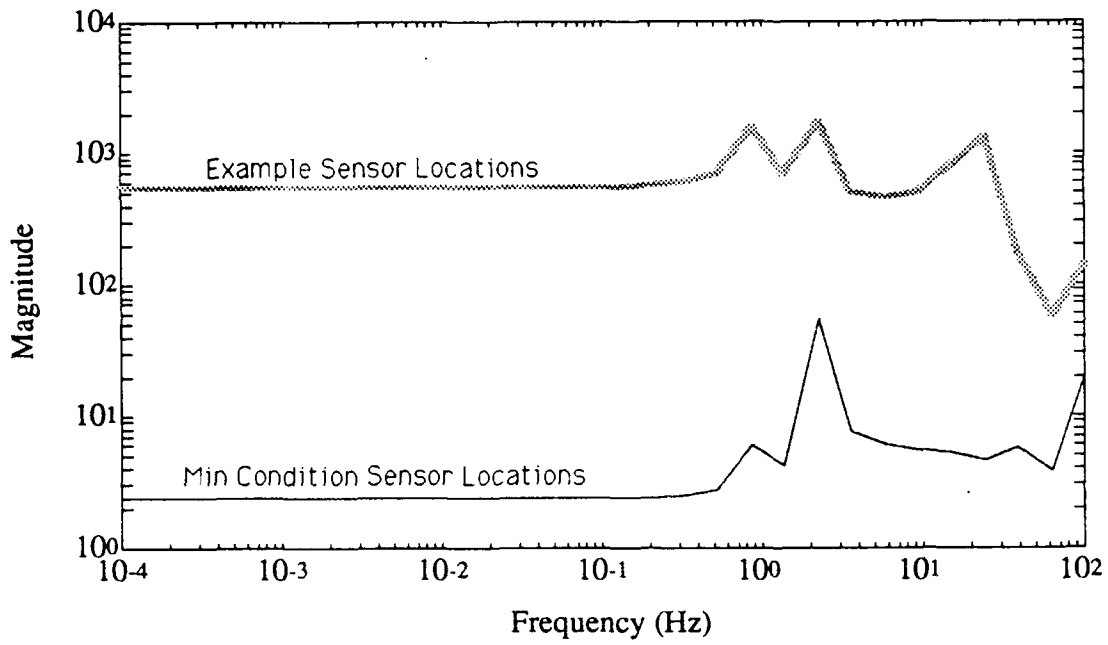


Figure 5.5: Condition Number - Single Petal Model

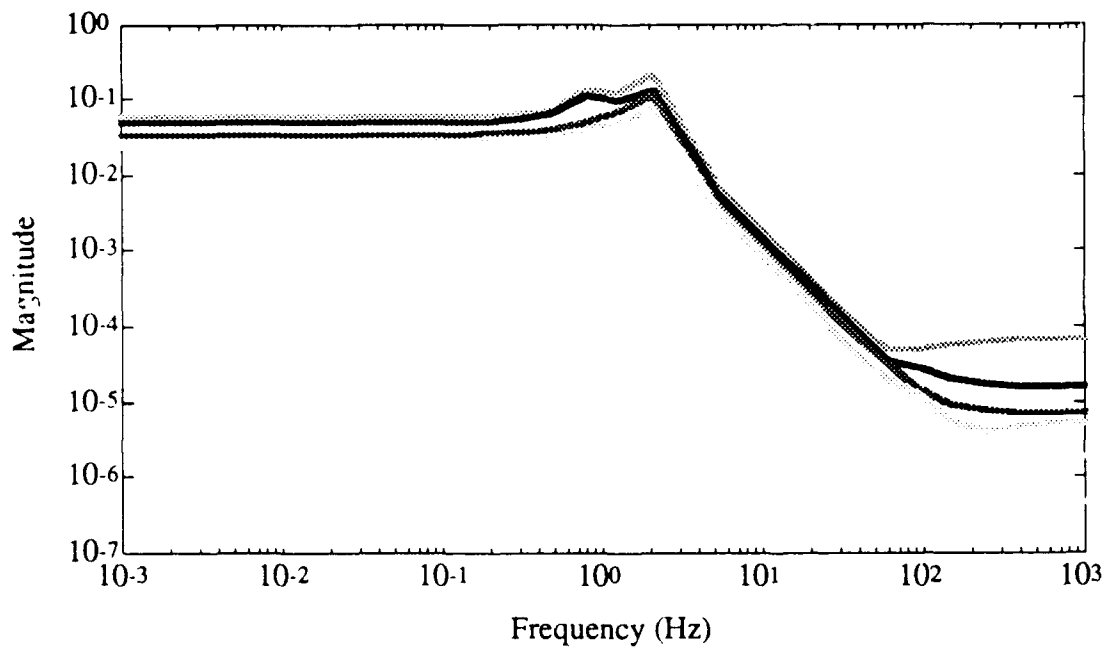


Figure 5.6: Open-Loop Singular Value Plot of Single Petal Model



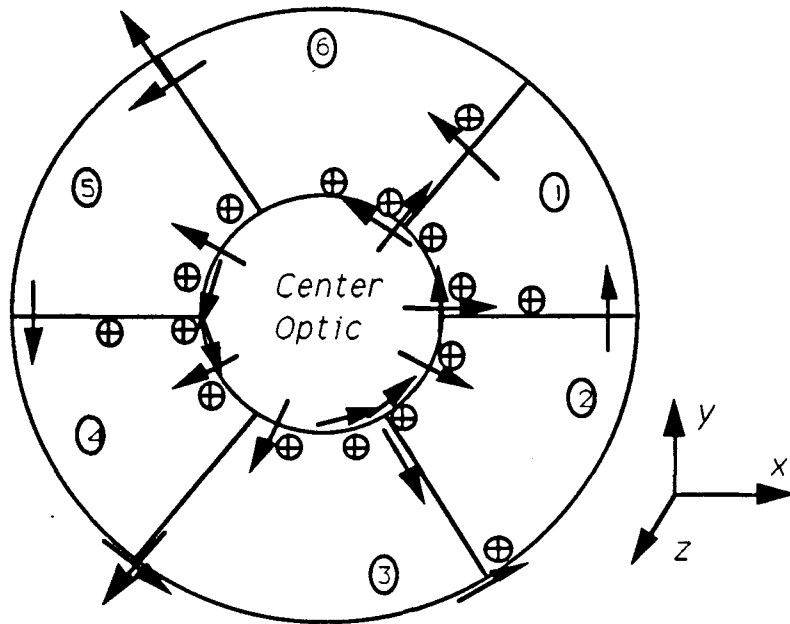


Figure 5.7: Sensor Locations Chosen - Full Model with 36 Sensors

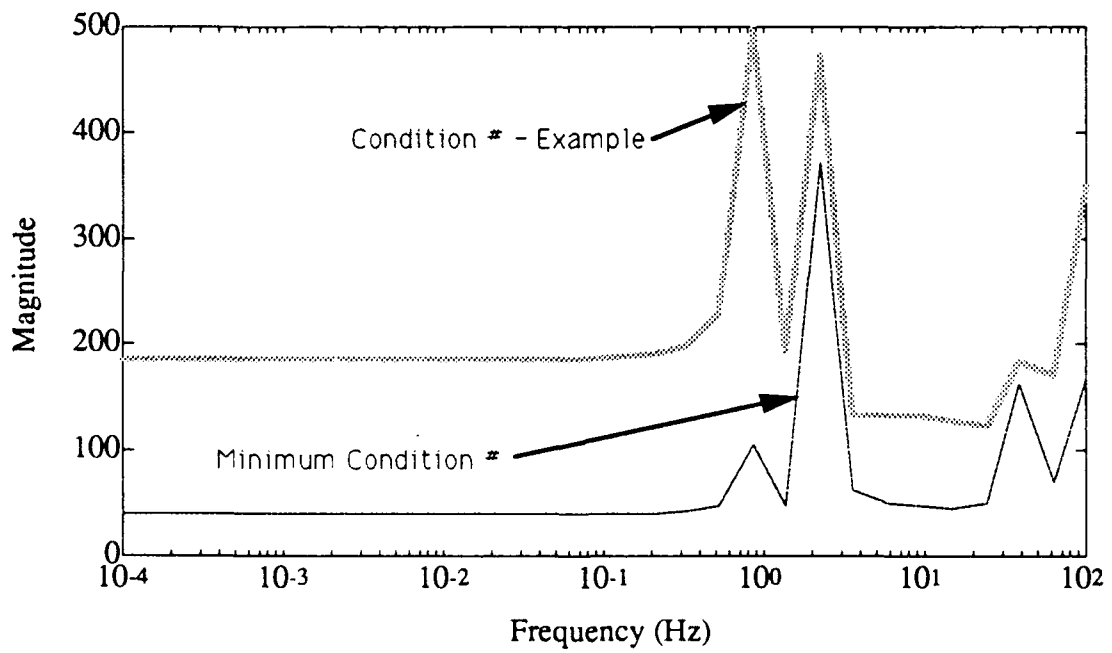


Figure 5.8: Condition Number - Full Model with 36 Sensors

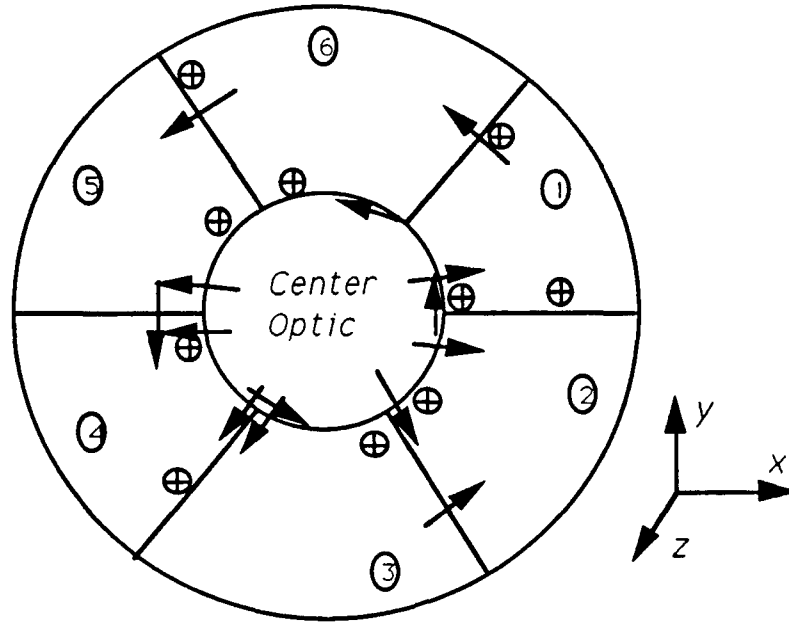


Figure 5.9: Sensor Locations Chosen - Full Model with 24 Sensors

in Figure 5.9. Again, note that the minimum plant condition number results from a selection of sensors with no apparent symmetry. The condition number of the sensors from both Figure 5.3 and Figure 5.9 are shown in Figure 5.10.

The sensor locations suggested by this analyses as yielding the best-conditioned plant still need to be tested to assure that observability of the system is maintained. Therefore, with the sensors selected for the minimum condition number of the model, observability and controllability of the models are tested.

### 5.3 Controllability and Observability

Controllability describes the coupling between the actuator inputs and the modes of the plant dynamics, while observability describes the coupling between the plant's modes and the output measurements. For a system to have optimum performance, the system must be observable and controllable. This means that inputs to the system will affect all of the plant's modes which are observable by the output measurements.

The state-space realization of a system is not unique. Different state-space matrices,  $A$ ,  $B$ ,  $C$ , and  $D$ , yield the same input-output response. The reason this occurs is due to the fact that each state matrix performs a different mapping, and it is the total map (inputs to outputs) that describes a system. It is useful to specifically describe the mappings found in an ordinary state equation,

$$\dot{x} = Ax + Bu$$

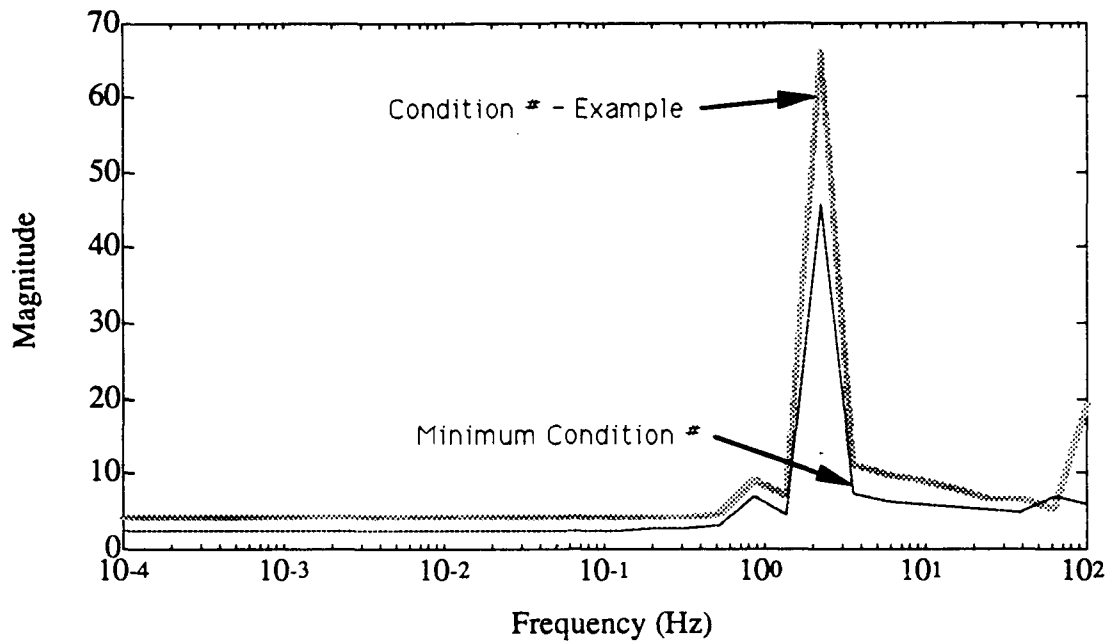


Figure 5.10: Condition Number - Full Model with 24 Sensors

$$y = Cx + Du$$

where  $u$  represents the inputs,  $y$  represents the outputs, and  $x$  represents the states.

For a system to be controllable, the coupling between the inputs and the states must be “complete,” while for a system to be observable, the coupling between the states and the outputs must be “complete.” Formal definitions of controllable and observable can be found in [2].

The definitions provide the meaning of controllable and observable systems, but they do not provide explicit tests. The controllability and observability of a system can be evaluated using the controllability and observability grammians [12] defined as:

$$G_c = \int_0^{\infty} e^{A\tau} B B^T e^{A^T \tau} d\tau \quad (5.2)$$

$$G_o = \int_0^{\infty} e^{A^T \tau} C^T C e^{A\tau} d\tau \quad (5.3)$$

The controllability grammian,  $G_c$ , has full rank if and only if the system is completely controllable, and the observability grammian,  $G_o$ , has full rank if and only if the system is completely observable. Controllability (and observability) is not usually a “yes” or “no” decision. The degree of controllability and observability can be determined through observation of the condition number of the controllability and observability grammian. The condition number provides a measure of how close a matrix is to losing “rank”. Therefore, the evaluation of the condition number of the controllability and observability grammian provides information on how controllable or observable a system is.

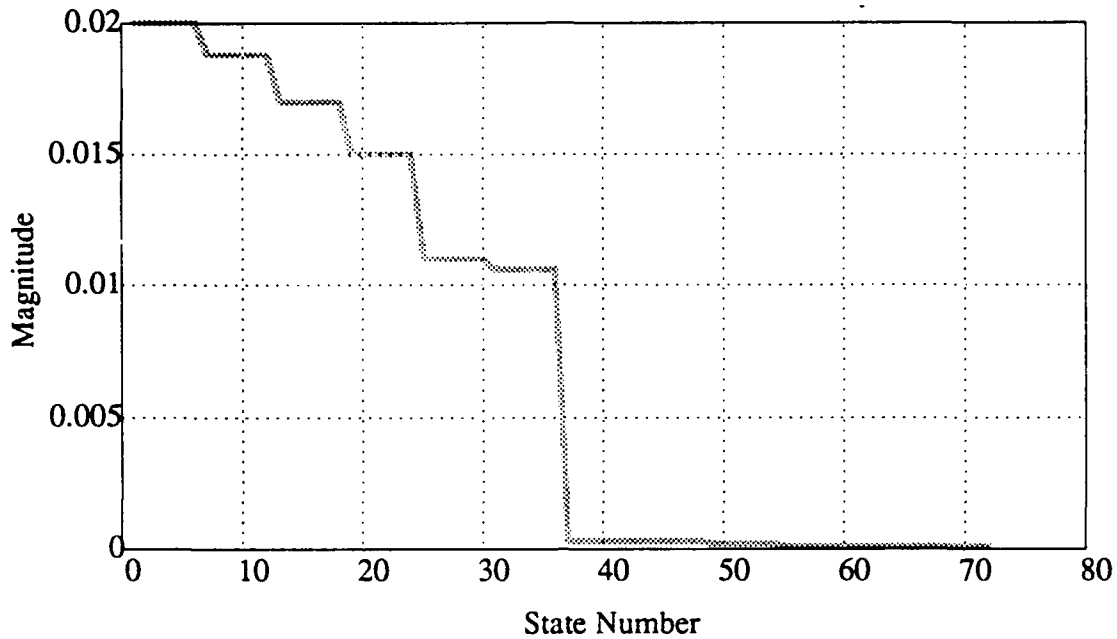


Figure 5.11: Controllability Grammian Singular Values - Full Petal Model

A system is said to be minimal if it is both completely controllable and observable. This is an important issue in modern control synthesis. If a plant has an uncontrollable and unobservable mode, this mode should be neglected when synthesizing a controller. The requirement of minimality is a necessity in optimizing a controller for a given plant.

As was discussed above, plant dynamics may make it possible to gather information on outputs without having to specifically measure the output. Equation 5.3 illustrates that observability is determined from both the  $A$  and  $C$  matrices. Therefore, for a dynamic model, it should not be surprising that a system with fewer measurements than inputs can be observable.

The sensor locations chosen for the three different models (single petal model, full model with 36 sensors, and full model with 24 sensors), minimum condition number case, provide an observable system. The system is also controllable. This does not appear to be the case, though, when looking at the singular values of the controllability grammian, shown in Figure 5.11. Note the sharp decline after the 36<sup>th</sup> singular value in Figure 5.11. This would seem to suggest that only 36 modes are controllable. As will be seen in Section 5.4 by balancing the model, all 72 modes are controllable. Note that the selection of sensors does not affect either the  $A$  or  $B$  matrices, therefore, the controllability grammian is the same for both full petal models.

The observability grammian singular values are shown for the full model with 24 sensors in Figure 5.12 and the full model with 36 sensor in Figure 5.13. Both of these cases are for the minimum condition number models. Through evaluation of the condition number of the observability gram-

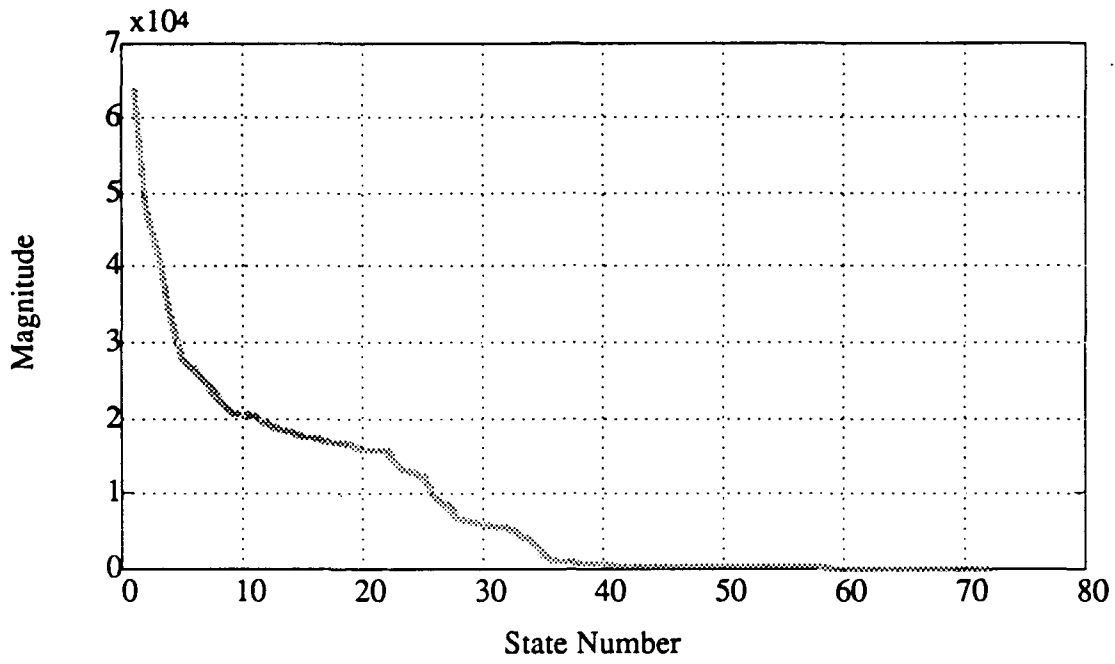


Figure 5.12: Observability Grammian Singular Values - Full Petal Model with 24 Sensors

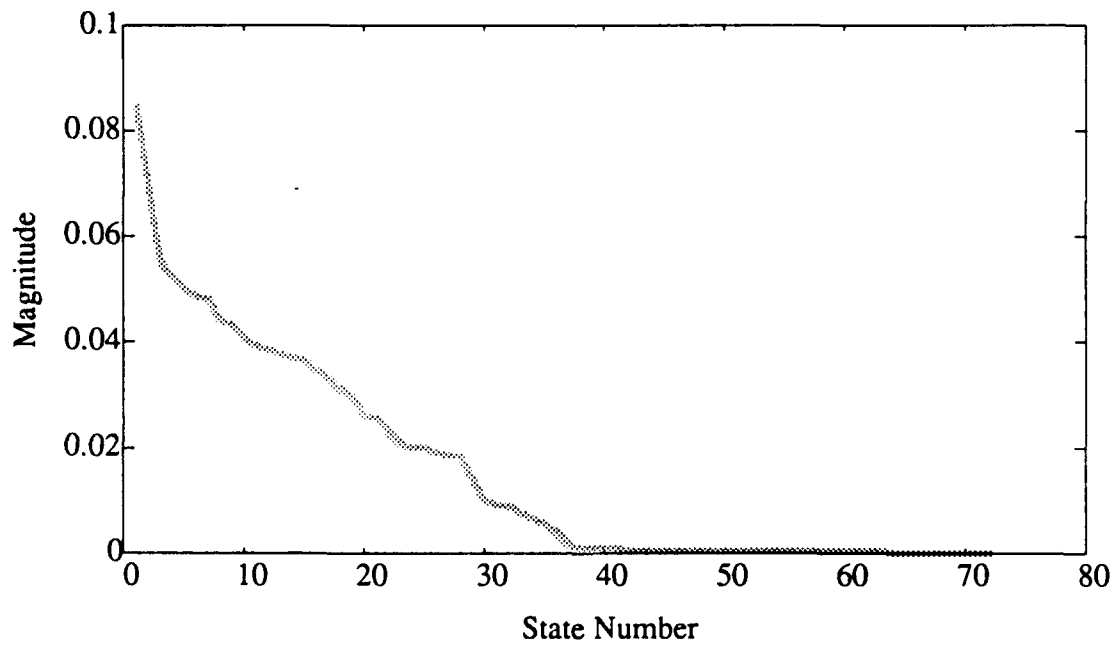


Figure 5.13: Observability Grammian Singular Values - Full Petal Model with 36 Sensors

mian, the 36 sensor model is “more” observable than the 24 sensor model (i. e.  $\mathcal{K}(G_{o_{36}}) < (G_{o_{24}})$ ). Also note the same type of decline at the 36<sup>th</sup> singular value as seen in the controllability grammian. If only using the unbalanced model, a control designer could claim that only 36 modes are observable. Again, Section 5.4 shows that with proper balancing, the deformable mirror system models are completely observable.

## 5.4 Balancing and Model Reduction

When dealing with a system that has many states, balancing the model and model reduction become important issues. This section provides the background needed to understand the concepts of balancing and reducing the model. As stated earlier, one of the first requirements in synthesizing an optimal controller is that the plant model needs to be minimal.

Assuming that the plant is indeed both controllable and observable (which is the case for the models of the deformable mirror system), it is desired to balance the controllability and observability of the states. In other words, it is desired to make a state as hard (or as easy) to control as it is to observe. One obvious way to do this would be to force the controllability grammian in Equation 5.2 to equal to the observability grammian in Equation 5.3. If we require these grammians to be equal and diagonal, the diagonal elements are referred to as the Hankel Singular Values (HSV). The HSVs provide a tool that can be used for model reduction.

A large HSV indicates a state that is both easy to control and observe, while small HSVs indicate states that are neither easy to control nor observe. The technique proposed in [15] is to eliminate the small HSVs by truncating the associated transformed states from the plant model. As long as the system retained does not have a HSV equal to zero, the reduced model will be both controllable and observable, hence minimal, and the model will be balanced. This becomes important in preparing the numerics of the plant for control system synthesis.

The three model cases addressed in this chapter do not have a significant difference between the largest HSV and the smallest HSV. Therefore, the plant models are balanced but not truncated. This result says that all states of the model are both controllable and observable. This appears to be in contrast to the plots shown in Section 5.3. The controllability and observability plots showed a marked decrease at 36 states. The results of the balancing illustrate that the decrease seen in the unbalanced model were due to scaling and not uncontrollable or unobservable modes. A typical plot of the HSV for the full model with 24 sensors is shown in Figure 5.14.

To further illustrate the properties of balancing, the controllability grammian singular values for the balanced model are shown on the same plot (Figure 5.15) as the controllability grammian singular values shown in Figure 5.11. As can be seen from Figure 5.15, the balanced controllability

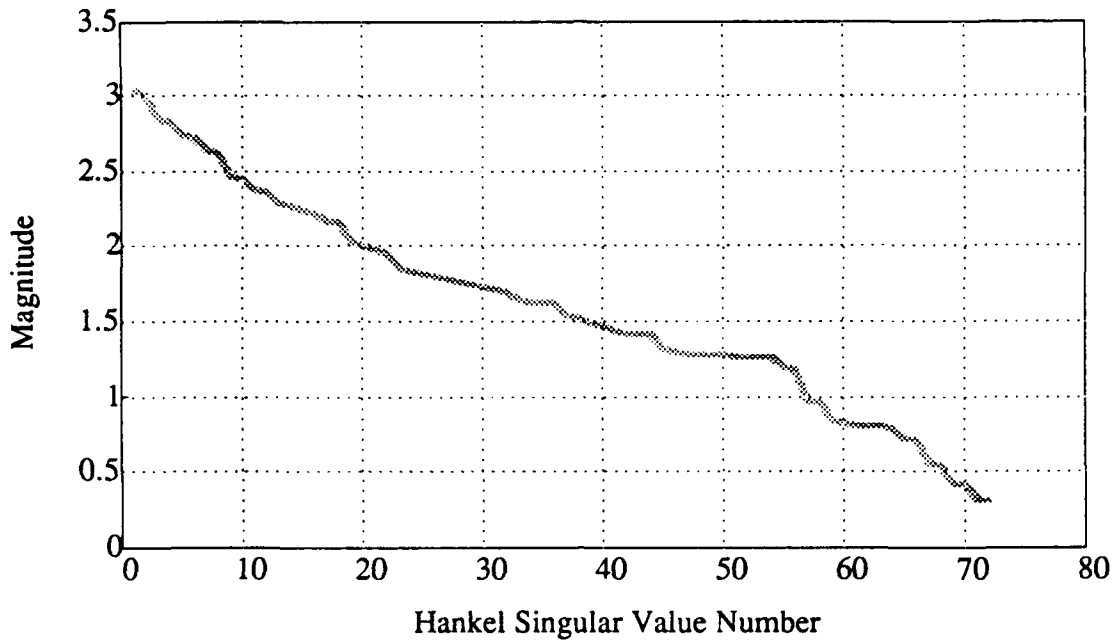


Figure 5.14: Hankel Singular Values - Full Model with 24 Sensors

grammians do not show a marked decrease at 36 modes. Notice the 2 order of magnitude drop in the unbalanced controllability grammian singular values at the 37th singular value. The magnitude of the maximum singular value of the balanced controllability grammian singular value to the minimum singular value of the balanced controllability grammian is less than 1 order of magnitude. This example illustrates the importance of balancing.

## 5.5 Open-Loop Poles and Zeros

Poles of the open-loop plant located in the right-half plane yield unstable plants. There are many methods available for testing the open-loop stability of a plant model. One method is to test the real parts of the eigenvalues,  $\lambda$ , of the state  $A$  matrix. If

$$\text{Re}[\lambda(A)] \leq 0$$

the system is stable. The deformable mirror system is open-loop stable.

In a Single-Input Single-Output (SISO) sense, zeros of a transfer function relate to frequencies of the input signal which produce no output. In a multivariable system, the idea of a zero is similar. Instead of a SISO transfer function, multivariable systems have matrices of SISO transfer functions, for example;

$$G(s) = \begin{bmatrix} \frac{s+4}{s^3-2s^2+s-3} & 3 \\ \frac{s+6}{s-3} & \frac{1}{s^2+4} \end{bmatrix}$$

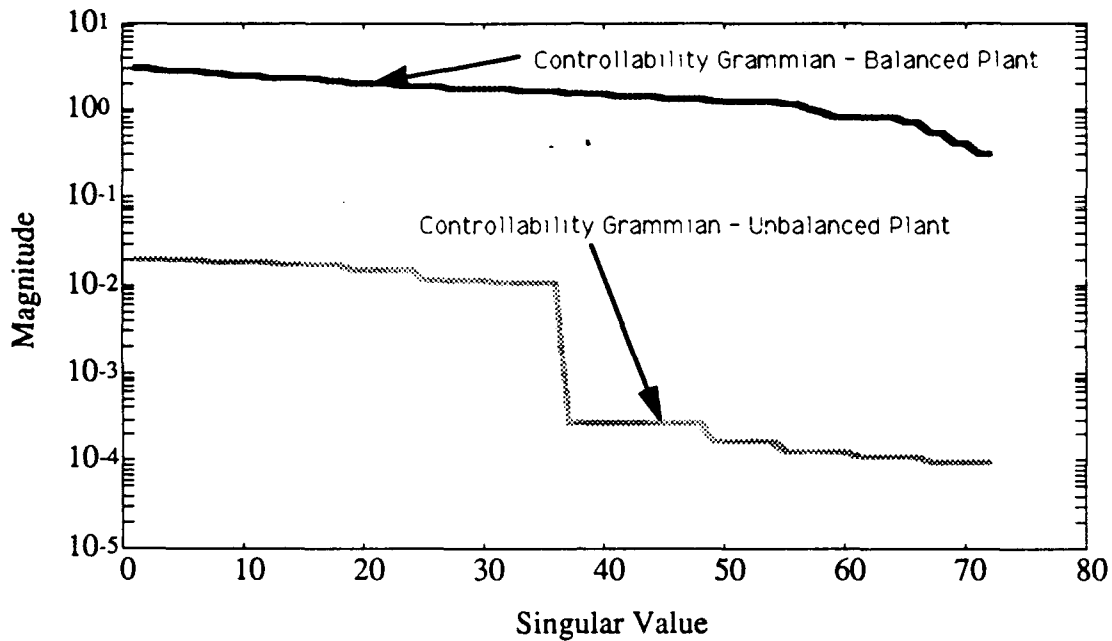


Figure 5.15: Comparison of Balanced and Unbalanced Controllability Grammian Singular Values

In this simple example, it is not clear what the zeros are of the system,  $G(s)$ .

Transmission zeros are defined as the zeros of the Smith-McMillan form [14]. The Smith-McMillan form of a rational matrix uses elementary row and column operations to generate a pseudo-diagonal rational matrix. The zeros of this form have similar characteristics to the SISO zeros.

The transmission zeros of the deformable mirror system include zeros in the open right-half plane. These zeros are referred to as nonminimum phase zeros. Nonminimum phase plants that require the sensitivity function to be less than one over some frequency range implies that the sensitivity function is necessarily greater than one at other frequencies [9]. The result of the nonminimum phase zeros is that these zeros impose constraints on the closed-loop system design. Therefore, the transmission zeros will limit the achievable performance for this system. The limitation of performance is the main issue raised by the transmission zeros in the open right-half plane. A more detailed discussion on the effects of transmission zeros is given in [9].

## 5.6 Conclusions

This chapter has detailed the open-loop analyses performed for the models of the deformable mirror system. An initial sensor position was chosen based on the geometry of the structure, and then the sensor positions were modified to reduce the condition number of the plant. This produces three distinct models that will be carried forward to the closed-loop system; a single petal



model with 6 sensors, the full model with 24 sensors, and the full model with 36 sensors. Each of these three models were tested for controllability, observability, and transmission zeros. All of the models are controllable and observable, and each model does contain transmission zeros in the open right-half plane (nonminimum phase zeros) which will impose limitations on the closed-loop performance. Each of the models were balanced, but there was no clear benefit in truncating the models. Chapter 6 details the closed-loop performance of the three models chosen in this chapter.

## Chapter 6

# Closed-Loop System

This chapter describes the closed-loop analyses that are performed in order to determine the performance robustness of the deformable mirror system. The deformable mirror system uses the position sensors to generate an error signal that is fed to the controller. The controller acts on this error signal in an attempt to null the error through the use of actuator commands at the petals. Before the analyses are presented, the sensor uncertainty and the application of the robust control specifications are developed. The method of augmenting the weighting functions applied to the deformable mirror system is described. The  $H_\infty$  controller solution is then presented for three plant model cases of the deformable mirror system.

### 6.1 Sensor Uncertainty

This section details the sensor uncertainty included in the analysis of the performance robustness of the deformable mirror system. As discussed in Chapter 4, the only uncertainty source considered in this thesis is uncertainty in the sensors.

It is assumed that the sensor has a multiplicative uncertainty at the output as shown in Figure 6.1. This implies that if the nominal sensor is described by  $S_{e_{nom}}(s)$ , then the actual sensor  $S_e(s)$  is described by

$$S_e(s) = S_{e_{nom}}(s) + l_{S_e}(s)\Delta_{S_e}S_{e_{nom}}(s) = (I + l_{S_e}(s)\Delta_{S_e})S_{e_{nom}}(s) \quad (6.1)$$

where  $l_{S_e}(s)$  represents a weighting function on the uncertainty and  $\Delta_{S_e}(s)$  represents a block of uncertainty.

The incorporation of the sensor uncertainty into the system block diagram enables the use of a formulation that has become standard in multivariable control analysis and synthesis. To place a problem into this "standard form" requires block-diagram manipulation. Figure 2.5 detailed the system block diagram. This block diagram is repeated in Figure 6.2 for convenience. If the full sensor block including uncertainty is now included in Figure 6.2, Figure 6.3 results.

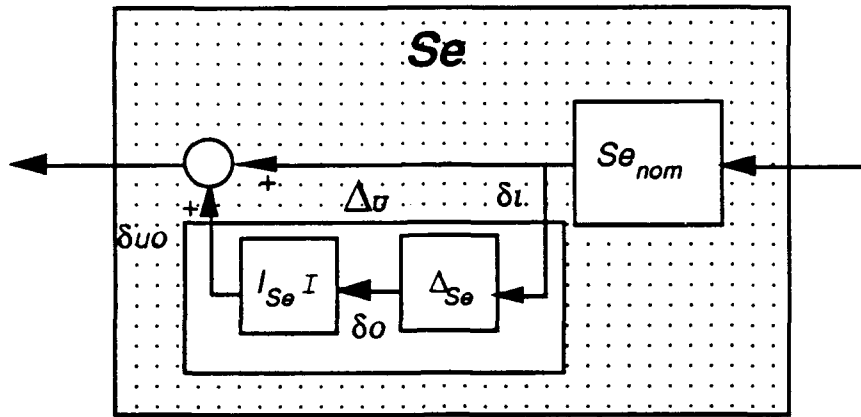


Figure 6.1: Sensor Illustrating Multiplicative Uncertainty

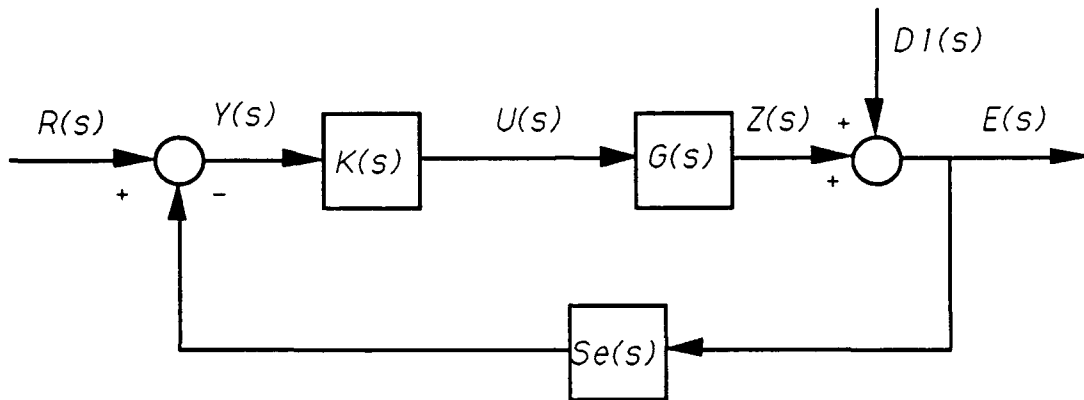


Figure 6.2: Block Diagram for the Deformable Mirror System

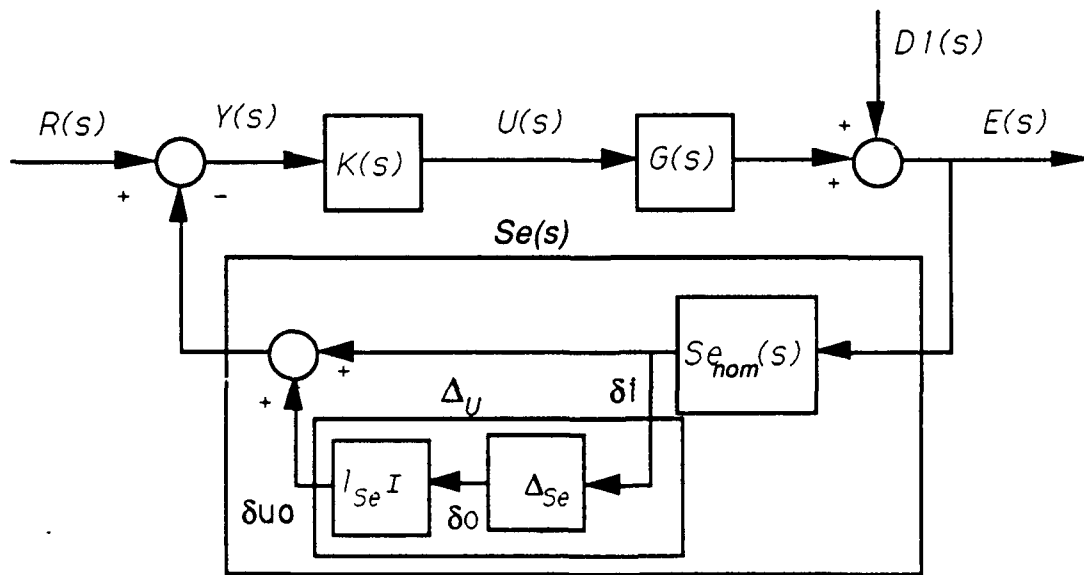


Figure 6.3: Block Diagram Including Sensor Uncertainty

The sensor uncertainty is defined as

$$\Delta_u(j\omega) = l_{S_e}(j\omega)\Delta_{S_e}(j\omega)$$

where the weighting function,  $l_{S_e}(s)$ , provides a tool for adjusting the uncertainty. Using this weighting function, the sensor uncertainty  $\Delta_{S_e}$  is bounded by unity so that

$$\bar{\sigma}(\Delta_{S_e}(j\omega)) \leq 1 \quad \forall \omega$$

Through application of the small gain theorem as discussed in Chapter 3, a sufficient condition for robust stability is

$$\bar{\sigma}[l_{S_e}(j\omega)M(j\omega)] < 1, \quad \forall \omega \quad (6.2)$$

where  $M(j\omega)$  represents the transfer function from  $\delta_i$  to  $\delta_{uo}$  in Figure 6.3. The purpose of the weighting function,  $l_{S_e}(j\omega)$  becomes evident, because the weighting function allows the designer to satisfy the requirements of the small gain theorem ( $\bar{\sigma}(\Delta_{S_e}) \leq 1$ ). This places the problem into a similar format of transfer function matrix and uncertainty shown in Figure 3.4, where the uncertainty block is  $\Delta_u$ .

The initial sensors chosen for the deformable mirror system have a bandwidth of 1 Hz with a single-pole roll-off. The frequency response of  $S_{e_{nom}}(s)$  is shown in Figure 6.4. Note that the sensor levels off at -80 dB. This is done for two reasons. The first involves the constraints of  $H_\infty$  synthesis using state-space methods. As will be explained in Section 6.3, this requires a full rank D matrix for the sensor in this case. This is accomplished by adding a zero to the transfer function representation of the sensor. A second reason is that this simulates the possibility of small signals being passed through the sensor at high frequency. The sensor is to be accurate to within 10% up to 1 Hz, and then the accuracy degrades at a rate of 20 dB/dec. This provides information needed to establish the uncertainty weight,  $l_{S_e}(s)$ . The uncertainty weight is shown in Figure 6.5. It needs to be emphasized that the uncertainty here is for each sensor individually. Therefore, the uncertainty block,  $\Delta_{S_e}(s)$  is diagonal.

With the sensor and sensor uncertainty weight now described, the analysis can proceed in placing the problem in a form for robust control system analysis.

## 6.2 Robust Control Specifications

This section details the specifications applied to the deformable mirror system to produce a controller that meets the robust performance specifications. An  $H_\infty$  controller was used for loop shaping. This section details the augmentation of the deformable mirror system models with weights in order to place the problem in a proper form for  $H_\infty$  controller synthesis. Details concerning

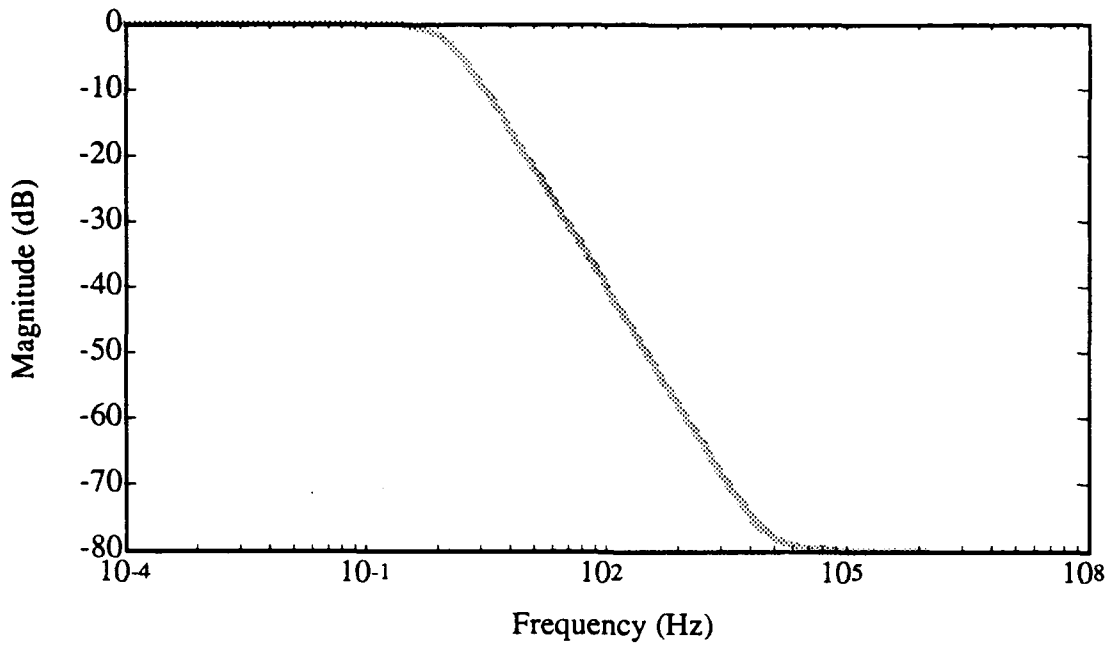


Figure 6.4: Nominal Sensor Characteristics

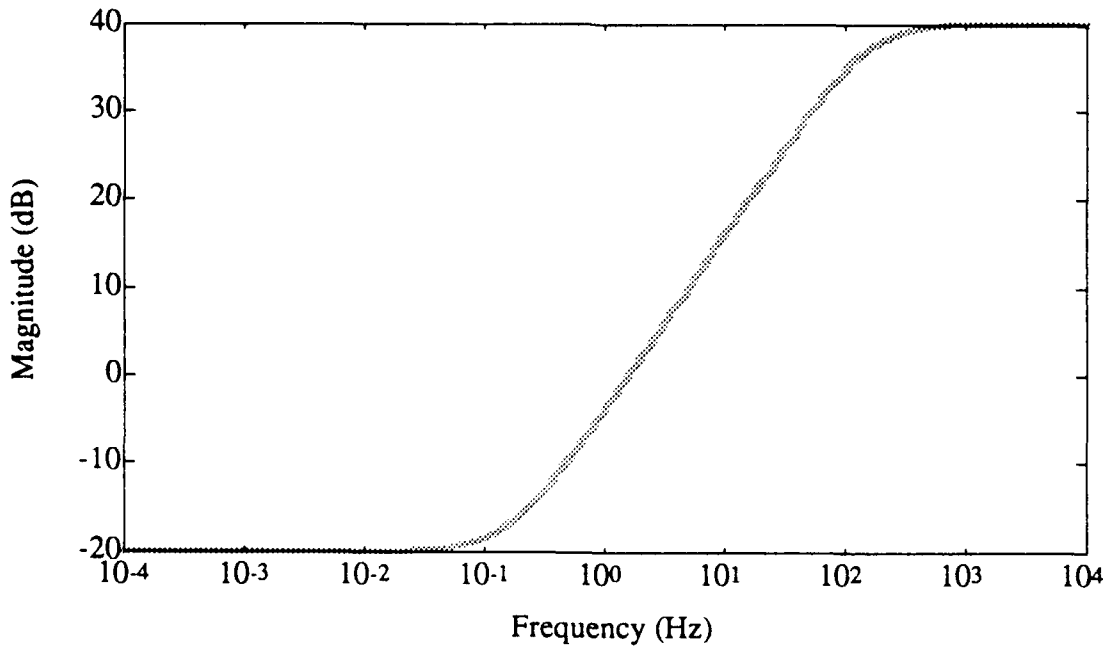


Figure 6.5: Uncertainty Weight Characteristics

the weights used for each of the various transfer function matrices are then provided. This section concludes with the description of the weight used to measure the performance robustness.

### 6.2.1 Plant Augmentation

One method of designing controllers is through the use of loop shaping techniques. A system requirement is provided to the control designers in terms of performance and robustness goals. These goals are then applied to various transfer functions within the control system model in order to design controllers to meet the requirements.

The method of loop shaping augments the system requirements to the dynamics of the system model. If a controller exists for the augmented system, then the controller will meet the requirements of the original system. If no controller can be found to meet the requirements of the augmented system, an iteration is required to lessen performance requirements or uncertainty.

The requirements of the deformable mirror system have been specified as a disturbance rejection requirement. Therefore, disturbance input effects at  $D_1(s)$  are to be minimized at the output,  $E(s)$ . The transfer function matrix relating  $D_1(s)$  to  $E(s)$  is called the sensitivity function,  $H(s)$ , and is represented by

$$H(s) = (I + G(s)K(s)Se(s))^{-1} \quad (6.3)$$

Another important transfer function matrix is the complementary sensitivity function, denoted by  $T(s)$ , relating the plant outputs at  $Z(s)$  to the system output,  $E(s)$ . This transfer function matrix describes the closed-loop performance of the system.

$$T(s) = (I + G(s)K(s)Se(s))^{-1}G(s)K(s)Se(s) = H(s)G(s)K(s)Se(s) = I - H(s) \quad (6.4)$$

The complementary sensitivity matrix transfer function provides a relationship of the plant outputs before the additive disturbance inputs to the system outputs after the additive disturbance inputs. Equation 6.4 also illustrates the trade-off between the sensitivity matrix transfer function and the complementary sensitivity transfer function. Ideally, the sensitivity matrix transfer function should be made as "small" as possible over a finite frequency range for good disturbance rejection. Also, ideally the complementary sensitivity matrix transfer function should be made as close to unity as possible over a finite frequency range for good setpoint tracking.

The final transfer function matrix used in the synthesis of a controller for the deformable mirror system is the transfer function from the disturbance inputs  $D_1(s)$  to the control inputs  $U(s)$ . This transfer function can be used to specify the bandwidth requirements of the actuators. This transfer function will be called the control input function, denoted by  $C_i(s)$ , in this thesis and is found from

$$C_i(s) = -K(s)Se(s)(I + G(s)K(s)Se(s))^{-1} = -K(s)Se(s)H(s) \quad (6.5)$$

The singular value Bode plots of these three transfer function matrices provide a framework for robust multivariable control system design. Through the use of each of these equations, bounds are chosen that each individual transfer function matrix must satisfy. These bounds are then combined to provide a mixed sensitivity analysis. This means that the bounds on each transfer function matrix must be met individually in order to satisfy the conditions for the synthesis of a controller.

The singular values of the sensitivity function  $H(j\omega)$  are “shaped” to satisfy a bound denoted by  $l_H(s)$ . Therefore

$$\bar{\sigma}(H(j\omega)) \leq |l_H(j\omega)^{-1}|, \quad \forall \omega \quad (6.6)$$

results. Here,  $|l_H(j\omega)^{-1}|$  is the desired disturbance attenuation factor. The functional description for  $l_H(j\omega)$  is provided below.

In a similar manner, the complementary sensitivity function  $T(j\omega)$  and the control input function  $C_i(j\omega)$  are also shaped to satisfy bounds as shown below.

$$\bar{\sigma}(T(j\omega)) \leq |l_T(j\omega)^{-1}|, \quad \forall \omega \quad (6.7)$$

$$\bar{\sigma}(C_i(j\omega)) \leq |C_c(j\omega)^{-1}|, \quad \forall \omega \quad (6.8)$$

Again, the functions used and their frequency responses are detailed in the section below.

With these bounds established, it is necessary to augment the block-diagram shown in Figure 6.3 to a modified system reflecting the weights. This augmented transfer function is shown in Figure 6.6. The shaded area shown in Figure 6.6 represents the augmented plant,  $P(s)$ . Simplifying Figure 6.6 through notation, Figure 6.7 represents the “standard” problem format, where

$$P(s) = \begin{bmatrix} 0 & S e_{nom} & S e_{nom} G \\ 0 & l_H & l_H G \\ 0 & 0 & C_c \\ -l_T l_{S_e} & -l_T S e_{nom} & -l_T S e_{nom} G \\ -l_{S_e} & -S e_{nom} & -S e_{nom} G \end{bmatrix} = \begin{bmatrix} P_{11} & P_{12} & P_{13} \\ P_{21} & P_{22} & P_{23} \\ P_{31} & P_{32} & P_{33} \\ P_{41} & P_{42} & P_{43} \\ P_{51} & P_{52} & P_{53} \end{bmatrix} \quad (6.9)$$

This figure is very useful in synthesizing multivariable controllers. The outputs are combined into one vector,  $W$  such that

$$W = \begin{bmatrix} Y_{1a} \\ Y_{2a} \\ Y_{3a} \end{bmatrix}$$

and the transfer function from  $D_1$  to  $W$  is evaluated for different controllers. As will be shown in Section 6.3, the state-space representation for  $P(s)$  allows the problem to be specified in a format suitable for  $H_\infty$  control synthesis.

Before describing the control system synthesis, the weighting functions are provided.

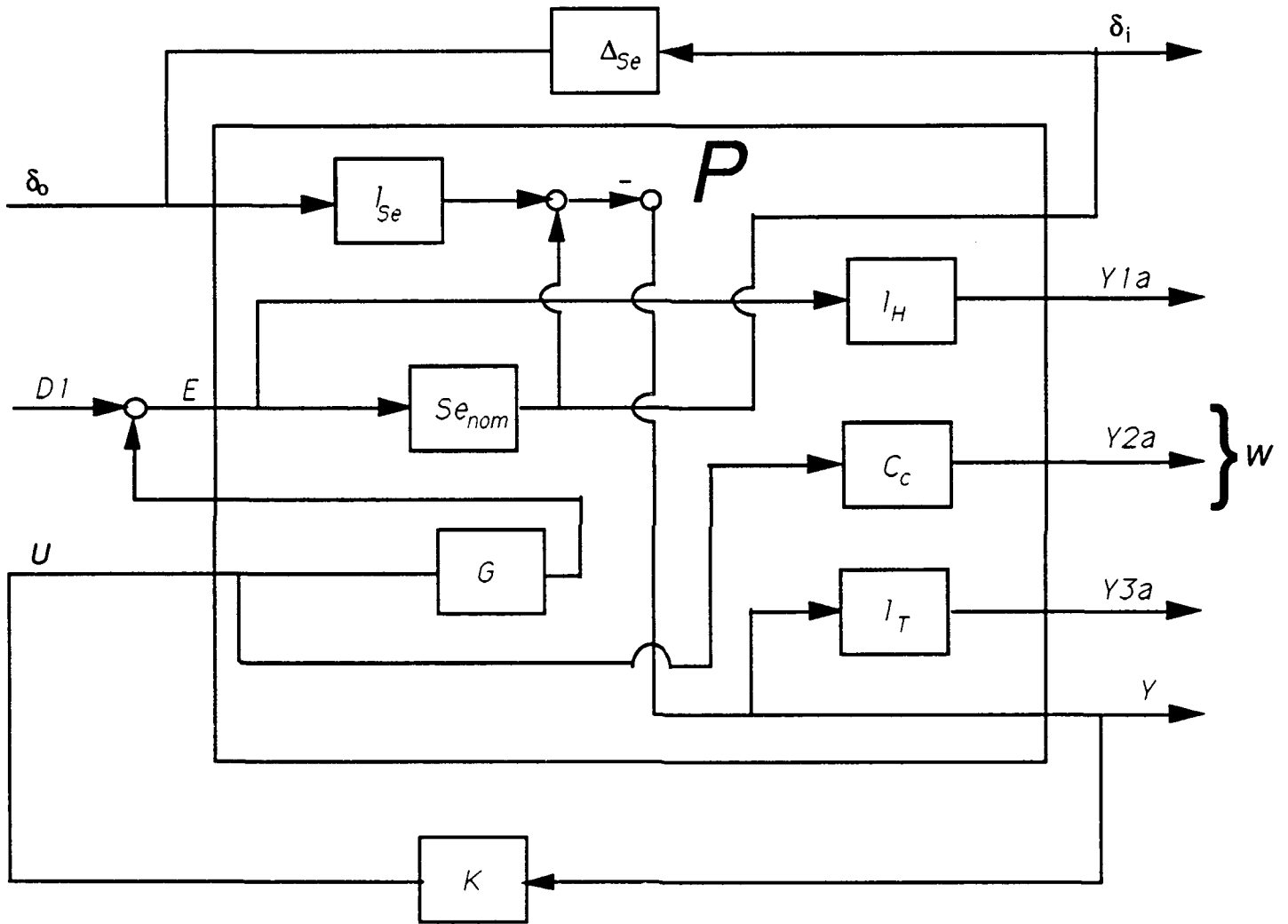


Figure 6.6: Augmented Form of Deformable Mirror System Block Diagram



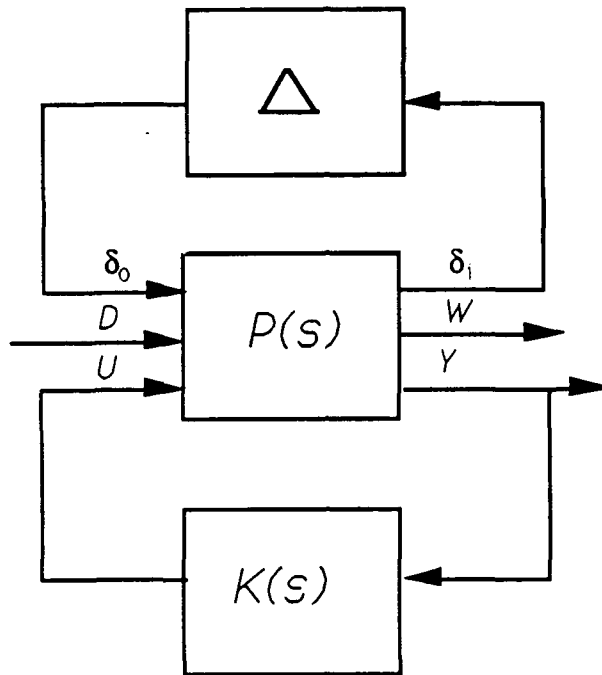


Figure 6.7: Standard Problem Block Diagram

### 6.2.2 Sensitivity Weighting Function

The deformable mirror system requirements described in Chapter 2 detail a specification on the sensitivity function,  $H(s)$ . It is desired to synthesize a controller such that Equation 6.6 is satisfied where  $|l_H(s)|$  is a desired disturbance attenuation factor.

Recall that the deformable mirror system is required to bound the “rms figure” by a magnitude of  $\frac{\lambda}{10}$  where  $\lambda = 63.28 \mu\text{m}$  for frequencies  $\leq 0.1$  Hz. Therefore, this bounding information can be used to generate  $l_H(s)^{-1}$ . For this analyses, it is assumed that the disturbance inputs are bounded by  $\|D_1\|_2 \leq 100 \mu\text{m}$ . This requires a constant scaling factor that needs to be applied to the performance specification of  $\frac{\lambda}{10}$ . Therefore, the equation for the sensitivity function weight for each manipulated variable becomes

$$l_H(s) = \frac{100}{\frac{63.28}{10}} \frac{s + 2\pi}{10(s + 0.2\pi)} \quad (6.10)$$

where the first fraction represents the normalizing constants for the robust performance specification. The second fraction is a normalized filter with a d. c. gain of 0 dB. It is important to remember that when this filter is actually applied, this results in

$$\|H\|_\infty \leq |l_H|^{-1}$$

Therefore, the performance is bounded by the inverse magnitude of the weight,  $l_H(j\omega)$ . The bound,  $l_H(s)^{-1}$ , is shown in Figure 6.8.

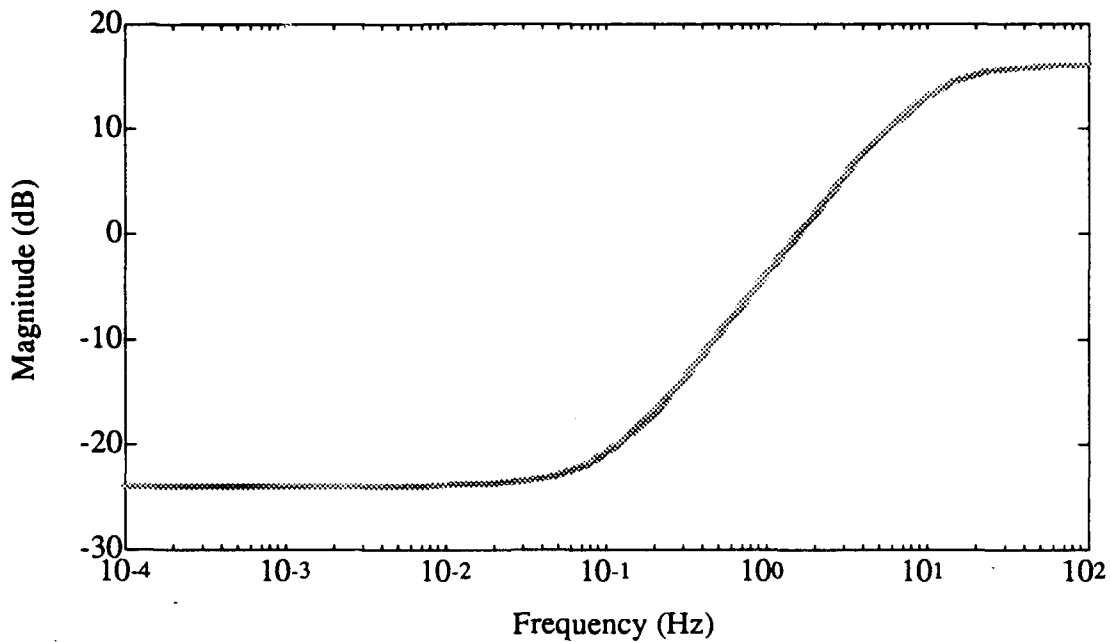


Figure 6.8: Sensitivity Function Bound

### 6.2.3 Complementary Sensitivity Weighting Function

The weighting function associated with the complementary sensitivity function can be related to the sensor uncertainty weight [16]. This provides information on the “shape” desired of the complementary sensitivity function. The shape should be approximately the inverse magnitude of the sensor uncertainty weight. To gain better performance in the low frequency range, the actual bound for the complementary sensitivity weight is lowered. Figure 6.9 illustrates the “shape” of the complementary sensitivity function weight. As can be seen when comparing this figure with Figure 6.5, the d. c. gain of  $|l_T(s)^{-1}|$  is approximately 6 dB where the uncertainty bound has a d.c. gain of 20 dB. As will be seen from the complementary sensitivity function plots detailed below, the actual d.c. magnitude of  $|l_T(s)^{-1}|$  has only a minor effect on the  $H_\infty$  control synthesis for this problem.

The transfer function equation describing the complementary sensitivity function weight for each manipulated variable is

$$l_T(s) = \frac{10(s + 50)}{s + 1000} \quad (6.11)$$

The cut-off frequencies were chosen arbitrarily in an attempt to maximize performance of the complementary sensitivity function. The only limitation on the cut-off frequencies is [4]

$$\omega_{l_H} < \omega_{l_T^{-1}}$$

This requirement means that the 0 dB crossover frequency of  $l_H$  must be sufficiently below the 0

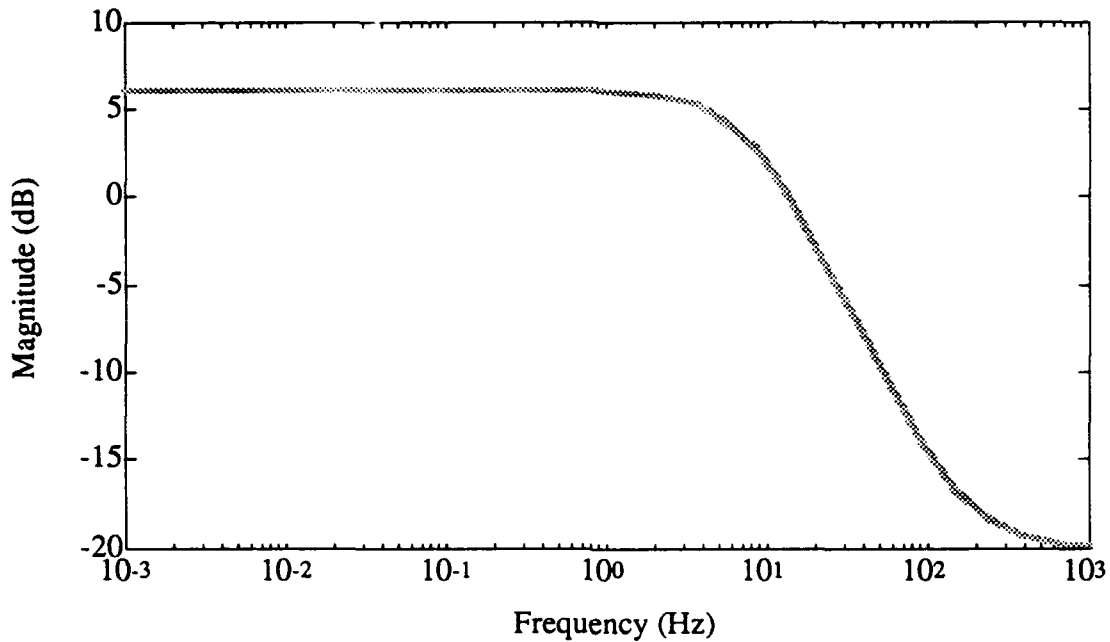


Figure 6.9: Complementary Sensitivity Function Bound

dB crossover frequency of  $l_T$  for the performance requirements to be achievable.

#### 6.2.4 Control Input Weighting Function

The weighting function for the control input  $C_c$  was set to a constant

$$C_c(s) = 3 \times 10^{-3} I \quad (6.12)$$

The primary reason this weight is included is to assure that the augmented system is “well-posed” for a state-space solution of the  $H_\infty$  controller. In Section 6.3, the general requirement for this weight will be explained more fully. It will be shown that the synthesis of an  $H_\infty$  controller for the deformable mirror system is very sensitive to changes in this weight.

With the bounds on the sensitivity, control input function, and complementary sensitivity function established, it is possible to combine these bounds to form a “mixed sensitivity” bound. This “mixed sensitivity” bound becomes the “cost” function for the  $H_\infty$  controller. Before proceeding into the  $H_\infty$  controller solution, the performance bounding weight will be described. This will complete the description of all weighting functions used in the deformable mirror system control synthesis and analysis.

#### 6.2.5 Robust Performance Weighting Specification

The establishment of the robust performance weight parallels the development of the sensitivity function weight,  $l_H(s)$ . The sensitivity function weight was established through the performance

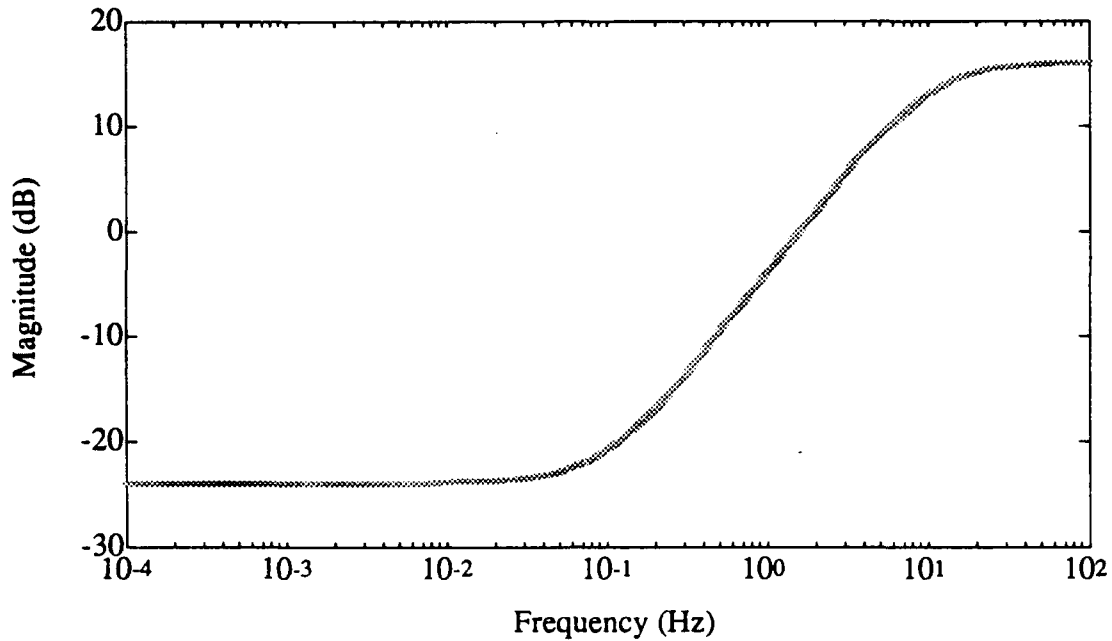


Figure 6.10: Robust Performance Bound

requirements of the deformable mirror system. The robust performance weight is the same weight. The difference occurs in where the weights are applied. As seen from Figure 6.6, the sensitivity function weight is applied to the output  $E$  resulting from the disturbance input  $D_1$ . The robust performance weight will be applied as described in Chapter 3. This enables the performance robustness to be analyzed with the structured singular value in a stability robustness analysis. A plot of the performance robustness bound  $|l_P(j\omega)|^{-1}$  is shown in Figure 6.10.

### 6.3 $H_\infty$ Controller Solution

This section details the design of the  $H_\infty$  controller for the deformable mirror system. In synthesizing  $H_\infty$  controllers, three different models were used. The first model was a single petal model with 6 inputs and 6 outputs. The second model was the full 72 state model with 36 inputs and 24 outputs, and the third model was the full 72 state model with 36 inputs and 36 outputs. The third model was employed to set-up some simple decentralized control system tests. All three cases described used the sensor selection based on optimizing the condition number of the plant as described in Chapter 5.

Each model was analyzed in the same manner. As shown in Figure 6.6 and shown in Equation 6.9, the deformable mirror system plant and sensor models have been appended with the states

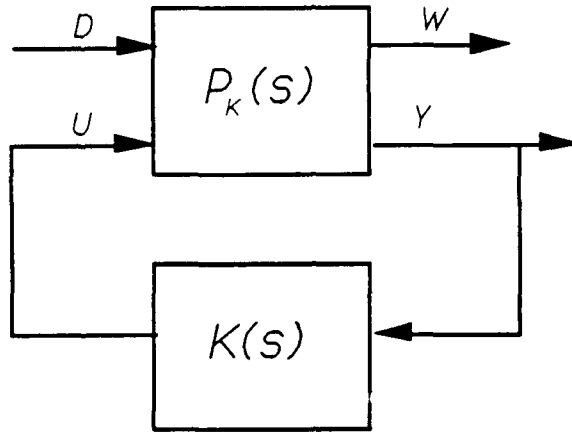


Figure 6.11: Augmented Plant for Calculation of  $H_\infty$  Controller

of various weighting functions. The overall  $H_\infty$  cost function becomes

$$\|T_{WD}\|_\infty \leq 1 \quad (6.13)$$

where

$$T_{WD} = \begin{bmatrix} l_H H \\ C_c C_i \\ l_T T \end{bmatrix} \quad (6.14)$$

An important property of singular values is

$$\max\{\bar{\sigma}(A), \bar{\sigma}(B)\} \leq \bar{\sigma} \begin{bmatrix} A \\ B \end{bmatrix} \leq \sqrt{2} \max\{\bar{\sigma}(A), \bar{\sigma}(B)\}$$

This property allows that Equation 6.13 implies Equation 6.6, Equation 6.7, and Equation 6.8. Therefore, Equation 6.13 is sometimes called a “mixed-sensitivity” cost function.

The solution of the  $H_\infty$  control problem for the deformable mirror system was obtained for the augmented system shown in Figure 6.11. This figure does not include the uncertainty block, and the uncertainty was not used in the calculation of the  $H_\infty$  controller but rather in the analysis of the performance after the controller had been designed.

The augmented plant,  $P_K(s)$ , utilizes the lower block of  $P(s)$  shown in Equation 6.9:

$$P_K(s) = \begin{bmatrix} P_{22} & P_{23} \\ P_{32} & P_{33} \\ P_{42} & P_{43} \\ P_{52} & P_{53} \end{bmatrix} \quad (6.15)$$

The state equation representation for the augmented plant can be found from the state space representations of each transfer function matrix. The state space representation for the augmented plant becomes

$$P_K(s) = \begin{bmatrix} A & B_1 & B_2 \\ C_1 & D_{11} & D_{12} \\ C_2 & D_{21} & D_{22} \end{bmatrix} \quad (6.16)$$

where

$$A = \begin{bmatrix} A_G & 0 & 0 & 0 \\ B_{Se}C_G & A_{Se} & 0 & 0 \\ B_{l_H}C_G & 0 & A_{l_H} & 0 \\ -B_{l_T}D_{Se}C_G & -B_{l_T}C_{Se} & 0 & A_{l_T} \end{bmatrix} \quad (6.17)$$

$$B_1 = \begin{bmatrix} 0 \\ B_{Se} \\ B_{l_H} \\ -B_{l_T}D_{Se} \end{bmatrix} \quad (6.18)$$

$$B_2 = \begin{bmatrix} B_G \\ -B_{Se}D_G \\ -B_{l_H}D_G \\ B_{l_T}D_{Se}D_G \end{bmatrix} \quad (6.19)$$

$$C_1 = \begin{bmatrix} D_{l_H}C_G & 0 & C_{l_H} & 0 \\ 0 & 0 & 0 & 0 \\ -D_{l_T}D_{Se}C_G & -D_{l_T}C_{Se} & 0 & C_{l_T} \end{bmatrix} \quad (6.20)$$

$$C_2 = \begin{bmatrix} -D_{Se}C_G & C_{Se} & 0 & 0 \end{bmatrix} \quad (6.21)$$

$$D_{11} = \begin{bmatrix} D_{l_H} \\ 0 \\ -D_{l_T}D_{Se} \end{bmatrix} \quad (6.22)$$

$$D_{12} = \begin{bmatrix} D_{l_H}D_G \\ D_{C_c} \\ D_{l_T}D_{Se}D_G \end{bmatrix} \quad (6.23)$$

$$D_{21} = [D_{Se}] \quad (6.24)$$

$$D_{22} = [-D_{Se}D_g] \quad (6.25)$$

In order to calculate an  $H_\infty$  controller, certain conditions on  $P_K(s)$  need to be met. In addition to the usual controllability and observability conditions, the "two-Riccati" formulae that define the controller [7] also require the following conditions to be satisfied:

1.  $\text{rank}(D_{12}) = \text{dim}(Y) \leq \text{dim}(W)$
2.  $\text{rank}(D_{21}) = \text{dim}(u) \leq \text{dim}(D)$

The augmented plant for the deformable mirror system meets these requirements. Condition 1 requires that the matrix,  $D_{12}$ , have full column rank. This means that all of the controls are included in the error vector. All of the weights used in the augmentation have full rank  $D$  matrices. The plant matrix is also full rank. Therefore, this condition is satisfied without including the constant term for the weight,  $C_c$ . The control input function weight is used as an additional weighting tool. In many cases, the original plant does not contain a feedforward  $D$  matrix. Therefore, the

requirement for  $D_{C_c}$  to be full rank is needed to satisfy Condition 1. Condition 2 requires the  $D_{21}$  matrix to be full row rank. This requires that noise must be included in all of the measurements. To satisfy this condition,  $D_{S_c}$  must be full row rank. This is the reason that the sensor includes a finite zero in the transfer function matrix. Therefore, Condition 2 is also satisfied. The problem is now in a form for computation of an  $H_\infty$  controller.

### 6.3.1 Case 1: Single Petal Model Results

The single petal model consists of the 6 input, 6 output, 12 state model using the sensors chosen for the best conditioned plant. This small model enables the computation of an  $H_\infty$  controller to be completed very rapidly. This section details the results of the controller designed for this model.

It should be noted that the use of an augmented plant greatly increases the size of the state-space. For the single petal model, the augmented  $A$  matrix contains 30 states. Therefore, the  $H_\infty$  controller generated will also contain 30 states. This produces numerical problems in the cases using the full model.

In order to evaluate the adequacy of the controller, several singular value plots are used. Figure 6.12 shows the maximum singular value plot for the transfer function matrix between the input,  $D_1$  and the error,  $W$ . In order to have a valid solution for the  $H_\infty$  controller, the maximum singular value of this transfer function matrix should be less than 1 for all frequencies as shown by Equation 6.14. Figure 6.12 illustrates this by showing the singular values of the cost function shown in Equation 6.14. The fact that  $\bar{\sigma}(T_{WD})$  is almost 1 for low-frequencies suggests that the controller is nearly  $H_\infty$  optimal. This means that the solution is nearing equality for the bound shown in Equation 6.14. For the given bounds, the  $H_\infty$  optimal solution is the "best" solution.

The singular value plots of the sensitivity and complementary sensitivity matrix functions are shown in Figure 6.13 and Figure 6.14 respectively. From the results seen in Figure 6.12, it is expected that both the sensitivity singular values and the complementary sensitivity singular values are bounded by their respective weights. Note the way the sensitivity singular values "follow" the weight,  $l_H(s)^{-1}$ . Also note the "flat" performance of the complementary sensitivity function. This indicates that outputs of the plant,  $Z$  are tracked at the output,  $E$ . This is the type of performance desired of the closed-loop system.

Figure 6.15 shows the singular value plot of the control input transfer function matrix,  $C_i(s)$ . The requirement for  $\bar{\sigma}(C_i(j\omega))$  is

$$\bar{\sigma}(C_i(j\omega)) \leq |C^{-1}| = 50.43\text{dB}$$

This is satisfied as can be seen in Figure 6.15. Note the "peaking" of control effort between 1 Hz and 10 Hz. In a sense, this illustrates the area that the controller is forced to work "hardest." Through

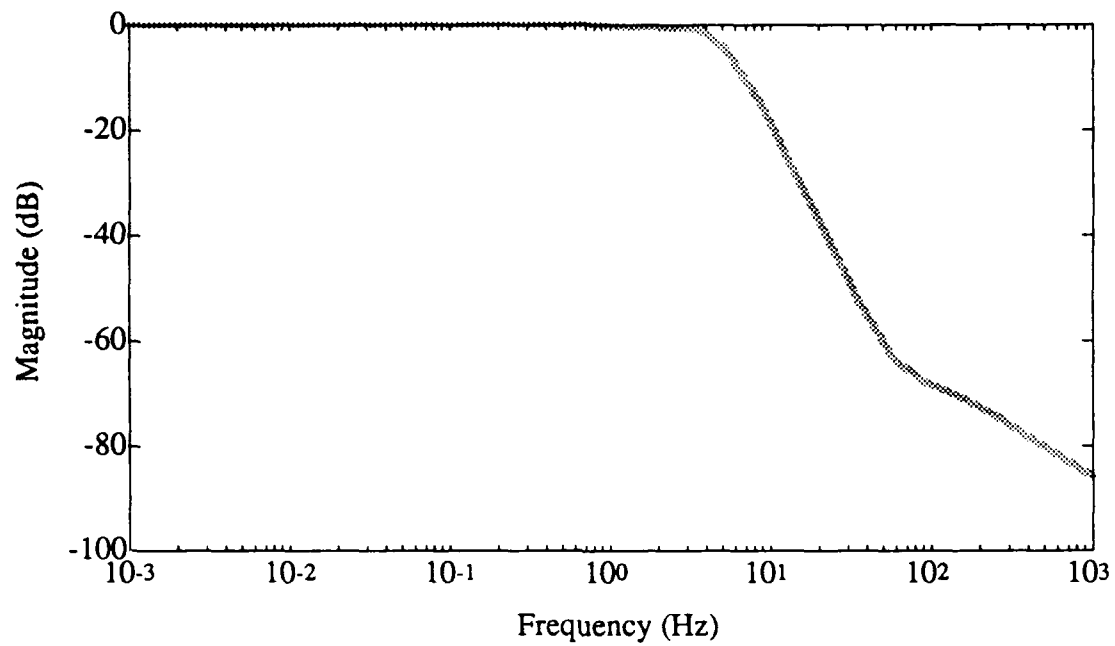


Figure 6.12:  $H_\infty$  Cost Function Singular Value Plot - Case 1

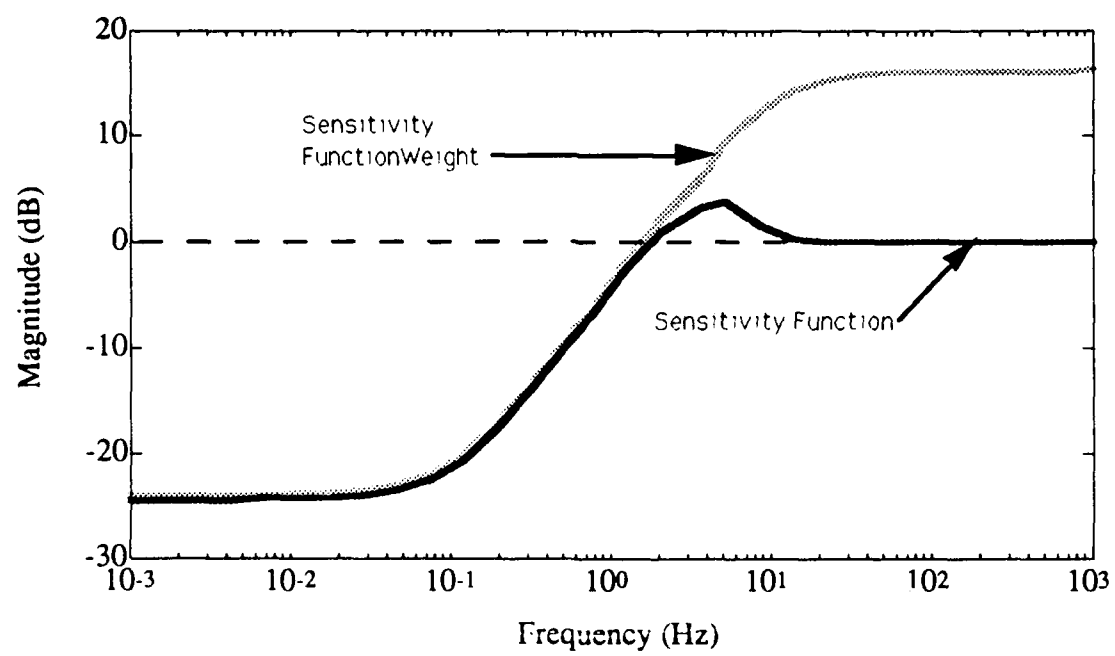


Figure 6.13: Singular Value Plot - Sensitivity Function - Case 1



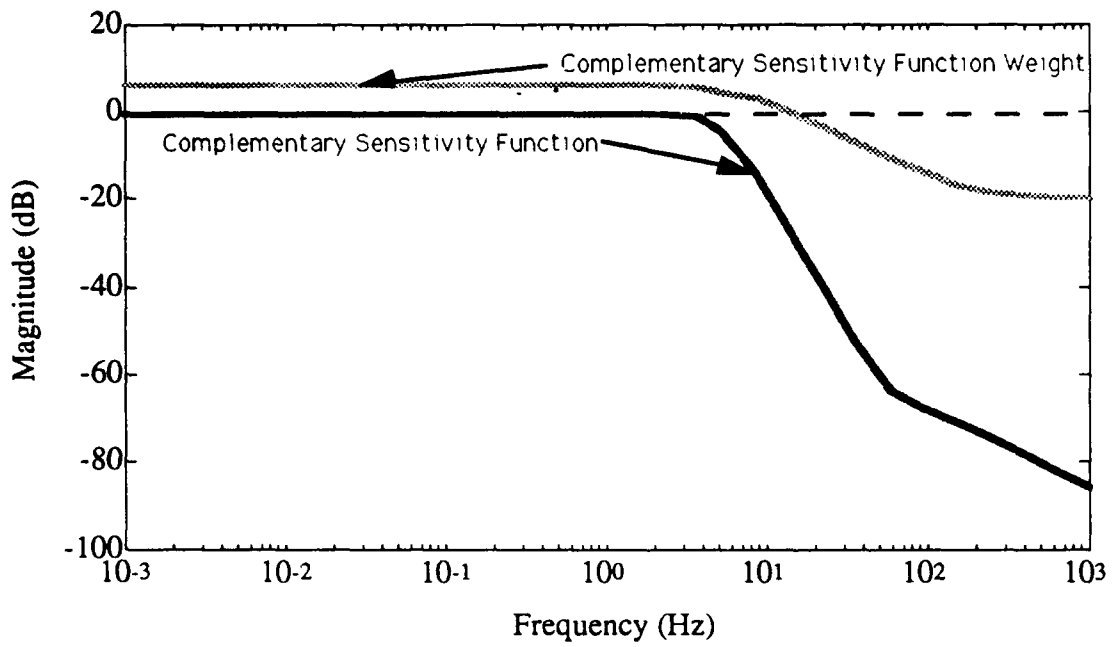


Figure 6.14: Singular Value Plot - Complementary Sensitivity Function - Case 1

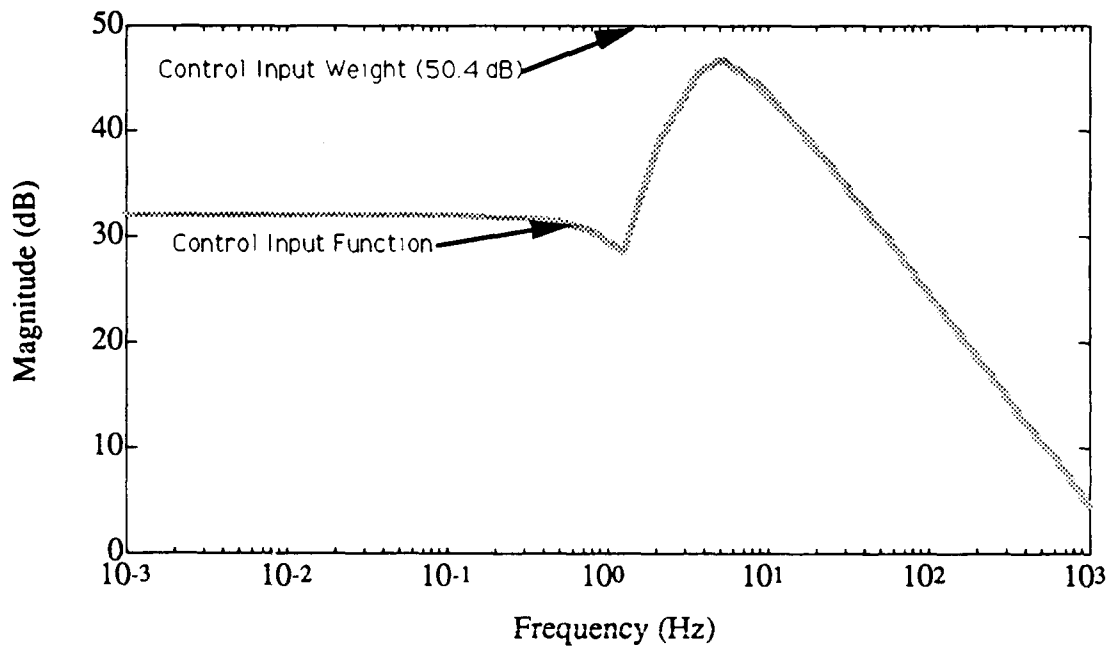


Figure 6.15: Singular Value Plot - Control Input Function - Case 1

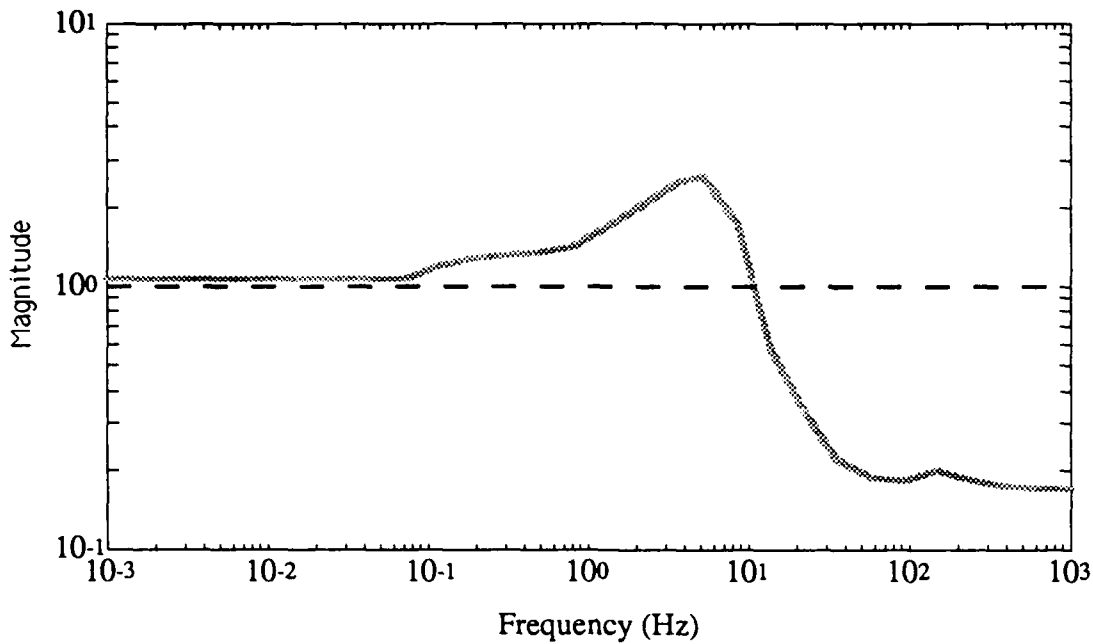


Figure 6.16: Structured Singular Value ( $\mu$ ) - Robust Performance - Case 1

manipulation of all of these weights, it was seen that the control synthesis was very sensitive to changes in the sensitivity weight  $l_H(s)$  and the control input weight,  $C_c$ .

With the controller calculated, the performance is next evaluated. Figure 6.16 shows the structured singular value plot, and the structured singular value exceeds 1. This implies that robust performance will not be met given the uncertainty magnitude of the sensor.

As a comparison with the other bounds, Figure 6.17 shows the maximum singular value,  $\bar{\sigma}$ , and the spectral radius,  $\rho$ . In this case, the maximum singular value is not less than 1 for any frequency range. This illustrates the bounds on  $\mu$  described in Equation 3.15. In order to meet the performance robustness specification, the sensor uncertainty must be reduced.

Through iteration on the sensor uncertainty, it was determined that a sensor accurate to within 1% to 1 Hz will enable the performance robustness specification to be met. Therefore, a modified uncertainty bound for the sensor is shown in Figure 6.18. Then performance robustness was determined using this reduced uncertainty, and the plot of the structured singular value is shown in Figure 6.19. The reduction of the sensor uncertainty produced the expected results, and the structured singular value now shows that performance robustness is maintained. Figure 6.20 details the maximum singular value,  $\mu$ , and the spectral radius. In this case,  $\bar{\sigma}$  shows that robust performance is not evident using this performance measurement tool. However, using  $\mu$ , performance robustness is demonstrated. This illustrates the meaning of non-conservative. Using  $\bar{\sigma}$  as the performance measurement tool would require reducing uncertainty or the performance requirement

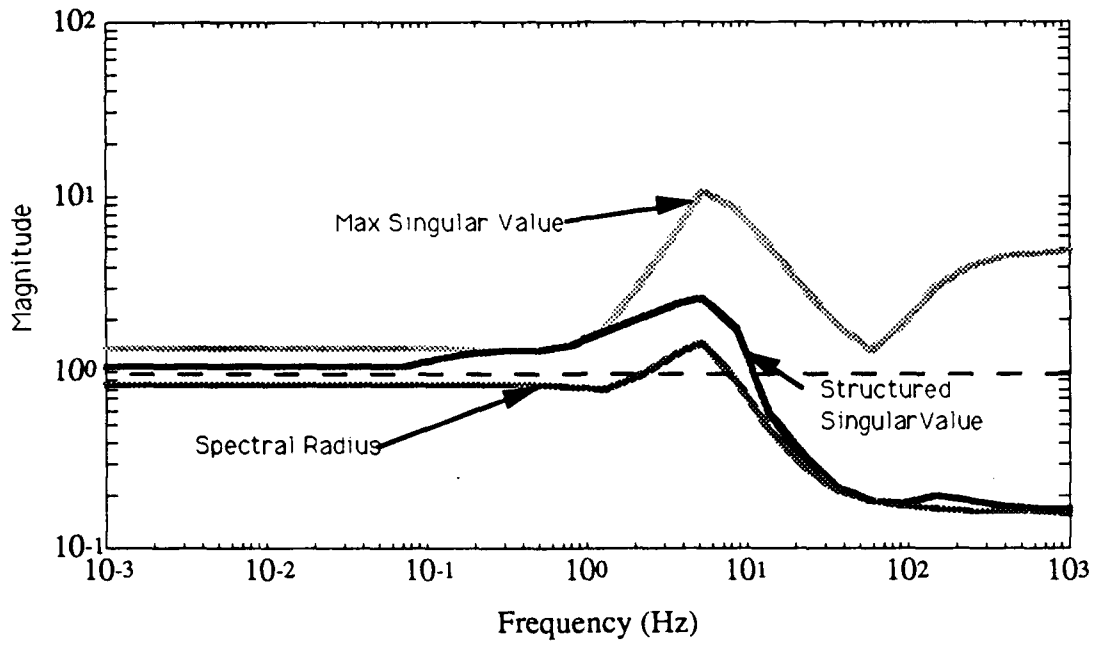


Figure 6.17:  $\bar{\sigma}$ ,  $\mu$ , and  $\rho$  Plots - Robust Performance -Case 1

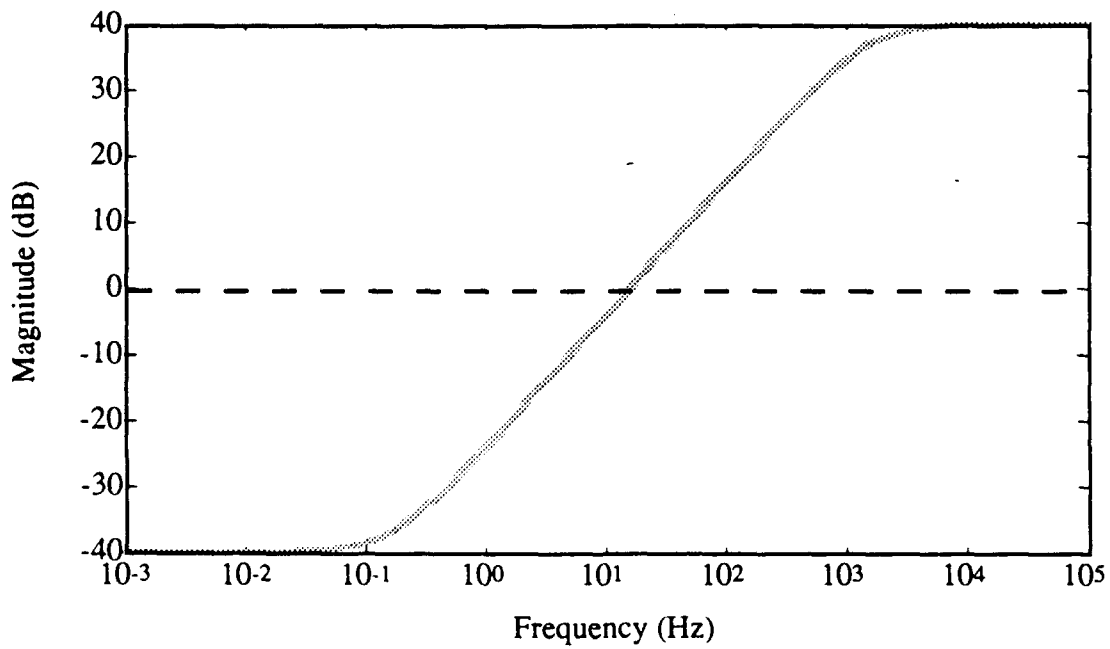


Figure 6.18: Modified Sensor Uncertainty Weight

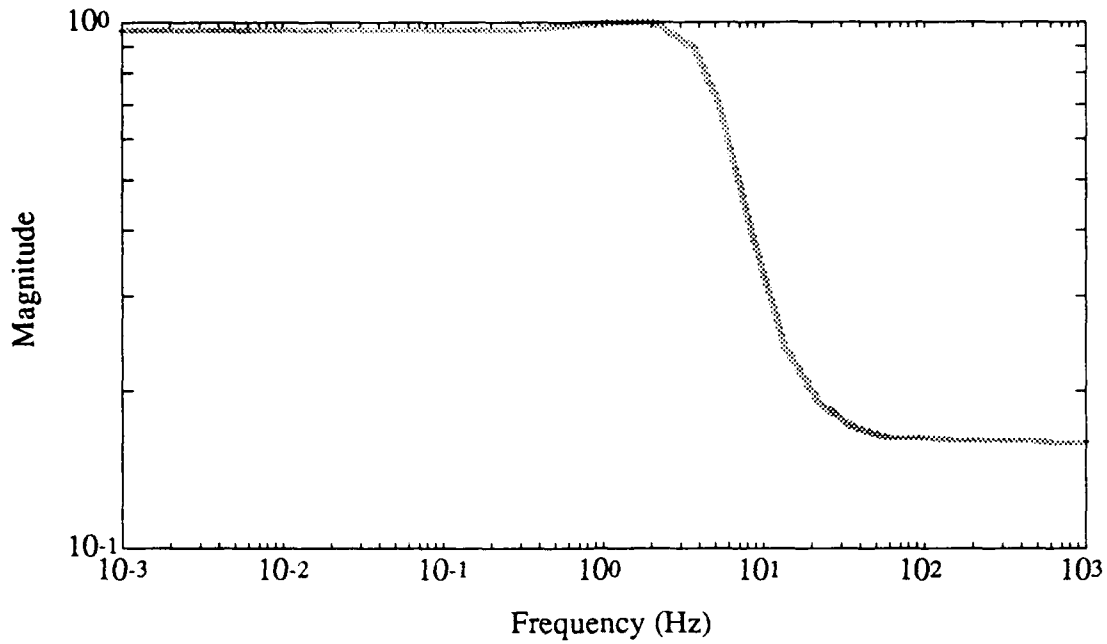


Figure 6.19: Structured Singular Value ( $\mu$ ) - Robust Performance - Case 1 with Reduced Uncertainty

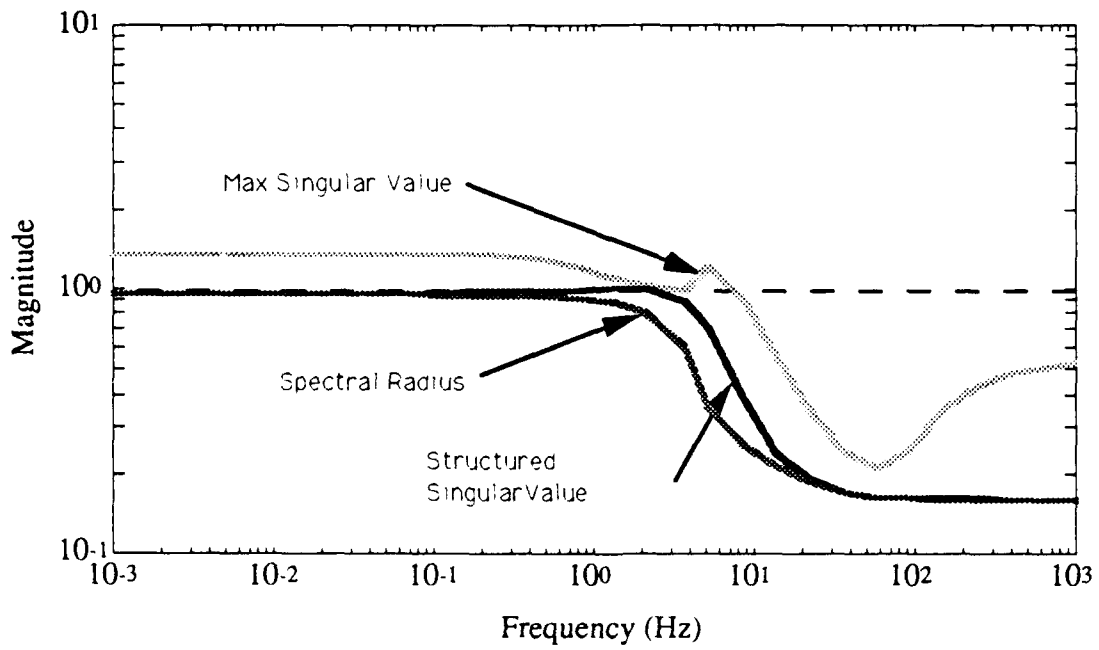


Figure 6.20:  $\bar{\sigma}$ ,  $\mu$ , and  $\rho$  Plots - Robust Performance - Case 1 with Reduced Uncertainty

while  $\mu$  shows that no reduction is necessary.

The sensor positions shown for the example case, Figure 5.1, were used for comparison to the results shown above. It was found that a controller could not be synthesized to meet the sensitivity weight bound. Therefore, the example measurement points were unable to provide the performance robustness required of this system.

With the performance robustness requirement met on the single petal model, these results will be used on the full model case with 24 sensors. For the results to truly scale to the full model case, the reduced uncertainty and the weighting matrices applied in the synthesis of the controller should yield a system that meets the performance robustness requirement.

### 6.3.2 Case 2: Full Model - 24 Sensors

The full model with 24 sensors utilizes the entire 6 petals with 36 inputs and 72 states. The same weighting functions,  $l_H(s)$ ,  $l_T(s)$ , and  $C_c(s)$ , were applied to this model as to the single petal model and an  $H_\infty$  controller was calculated.

As was noted above, the augmented state-matrices contain many states. For this case, the augmented  $A$  matrix contains 144 states. Therefore, the controller will also contain 144 states. When using the state matrix format to generate the open-loop system,  $GK$ , the state-space contains 288 states. This shows how quickly the state dimension can increase, and the evaluation of the transfer function matrices via state-space methods may not be wise. Instead, the transfer function matrices can be generated and the multiplications can be carried out on the reduced dimension input-output maps. It is better to calculate  $G(j\omega)$  and  $K(j\omega)$  at each frequency and multiply the matrices,  $GK(j\omega) = G(j\omega)K(j\omega)$ .

Figure 6.21 shows the maximum singular value plot for the transfer function matrix between the disturbance input  $D_1$  and the weighted performance vector  $W$ . For the  $H_\infty$  controller to have a solution as posed in Equation 6.14, the maximum singular value,  $\bar{\sigma}(T_{WD}) \leq 1 \forall \omega$ . As with the single petal case, Figure 6.21 shows that a valid solution was obtained for the  $H_\infty$  controller.

The singular value plots of the sensitivity function and complementary sensitivity function are shown in Figure 6.22 and Figure 6.23. The sensitivity singular values are "shaped" by the sensitivity weighting function,  $l_H(s)^{-1}$ , and the sensitivity singular values are bounded by this function. The plot of the complementary sensitivity function is also bounded by the complementary sensitivity function weight,  $l_T(s)^{-1}$ . As hoped, the singular value plots of case 2 resemble the singular value plots described above for case 1.

Figure 6.24 shows the singular value plot of the control input transfer function matrix,  $C_i(s)$ . Note that  $\bar{\sigma}(C_i(j\omega))$  has a similar shape when compared to the single petal plot shown in Figure 6.15. The performance robustness was evaluated for the case of the reduced sensor uncertainty,

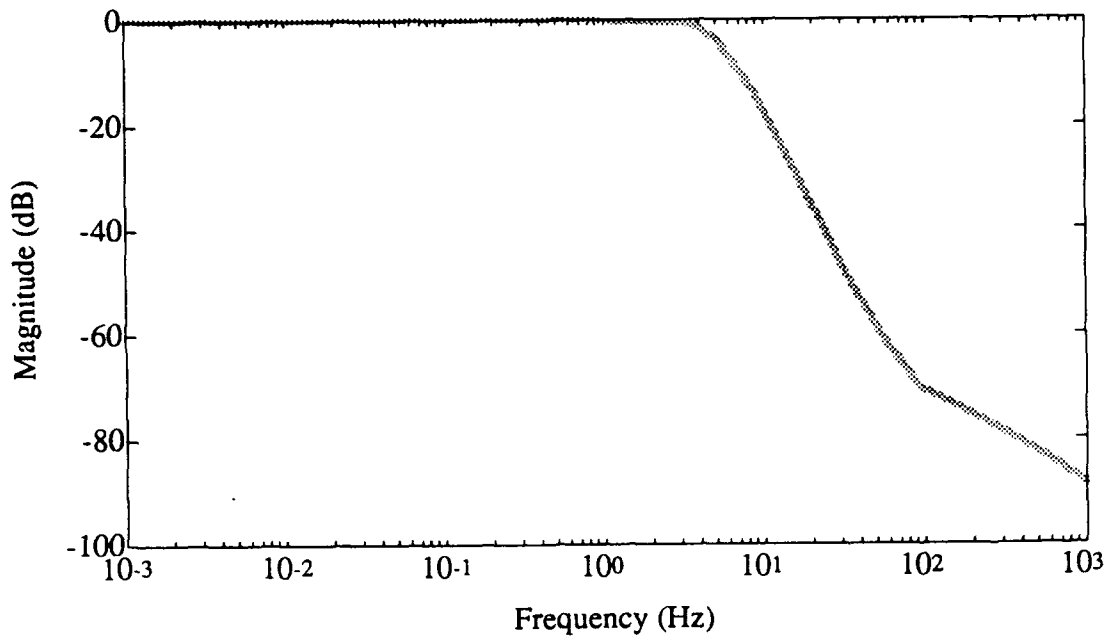


Figure 6.21:  $H_\infty$  Cost Function Singular Value Plot - Case 2

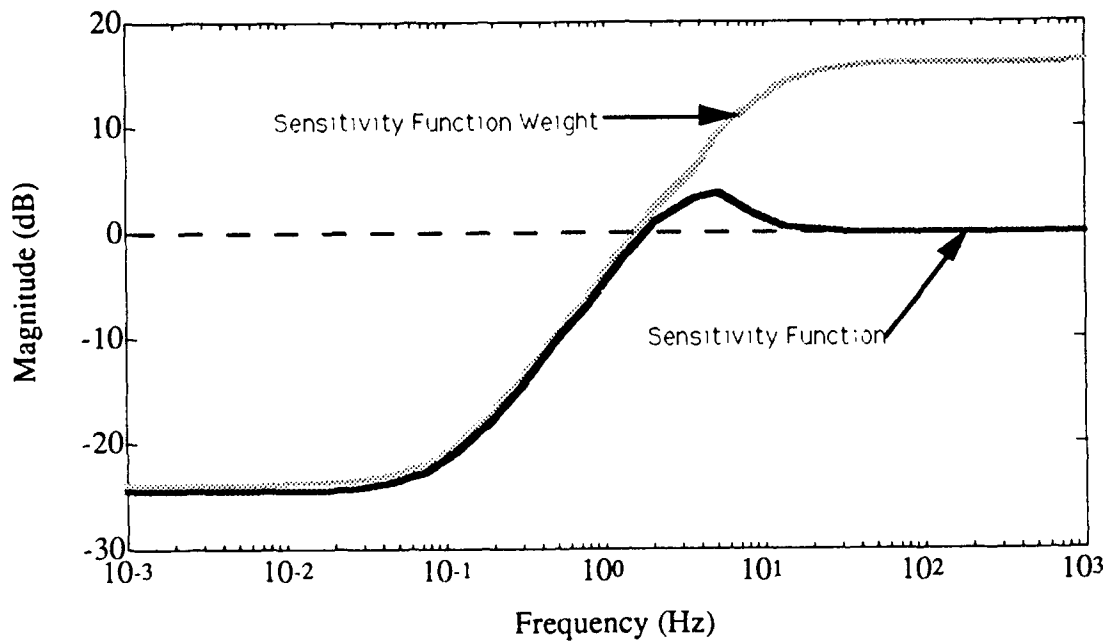


Figure 6.22: Singular Value Plot - Sensitivity Function - Case 2

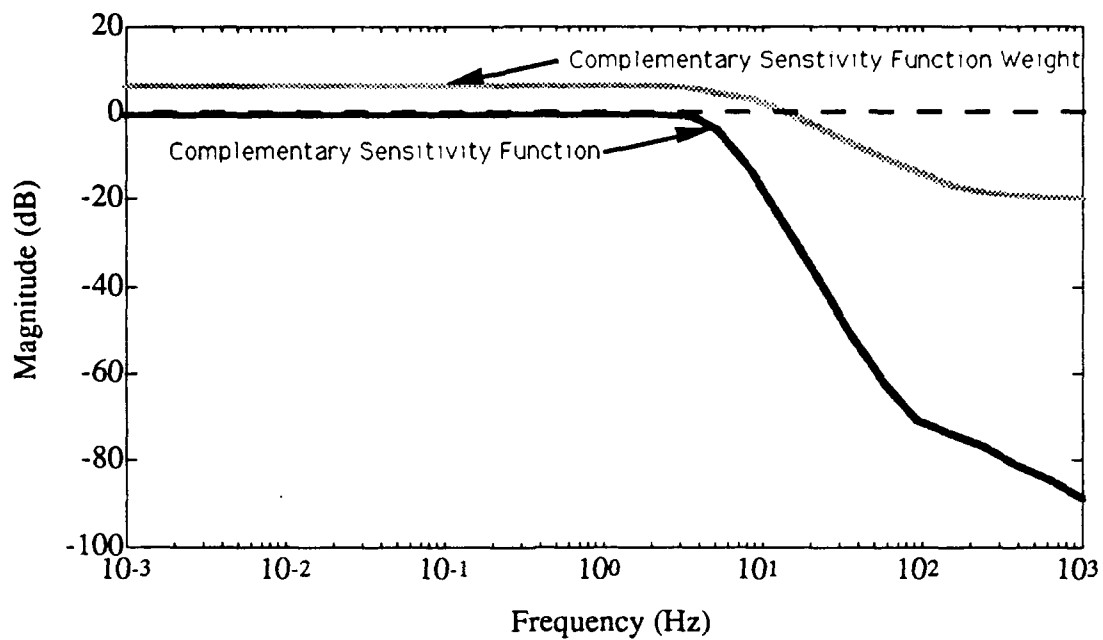


Figure 6.23: Singular Value Plot - Complementary Sensitivity Function - Case 2

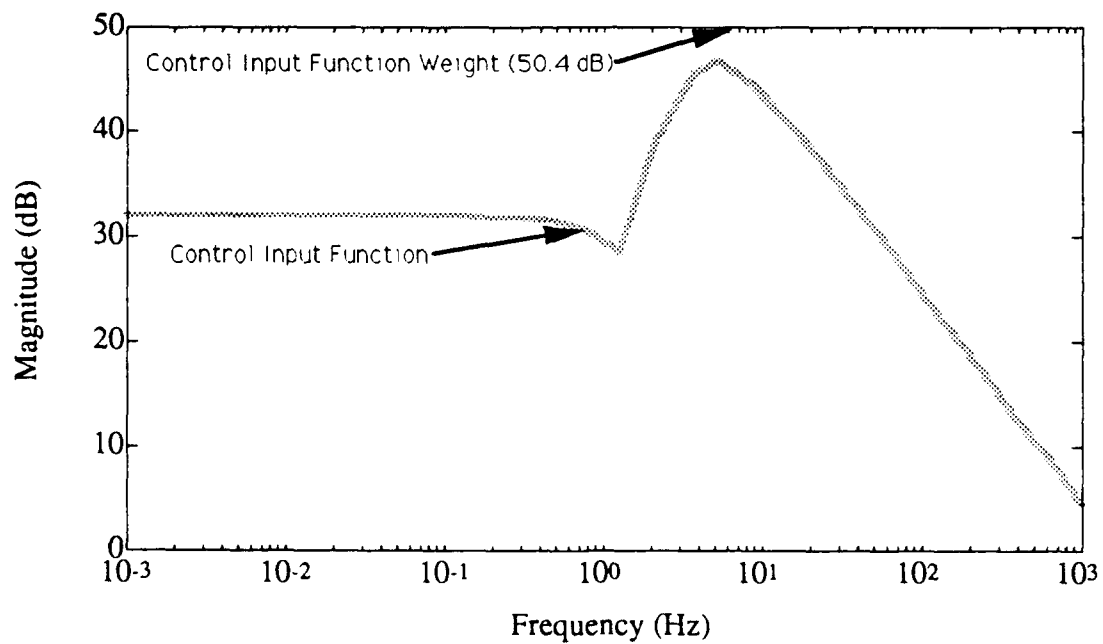


Figure 6.24: Singular Value Plot - Control Input Function - Case 2

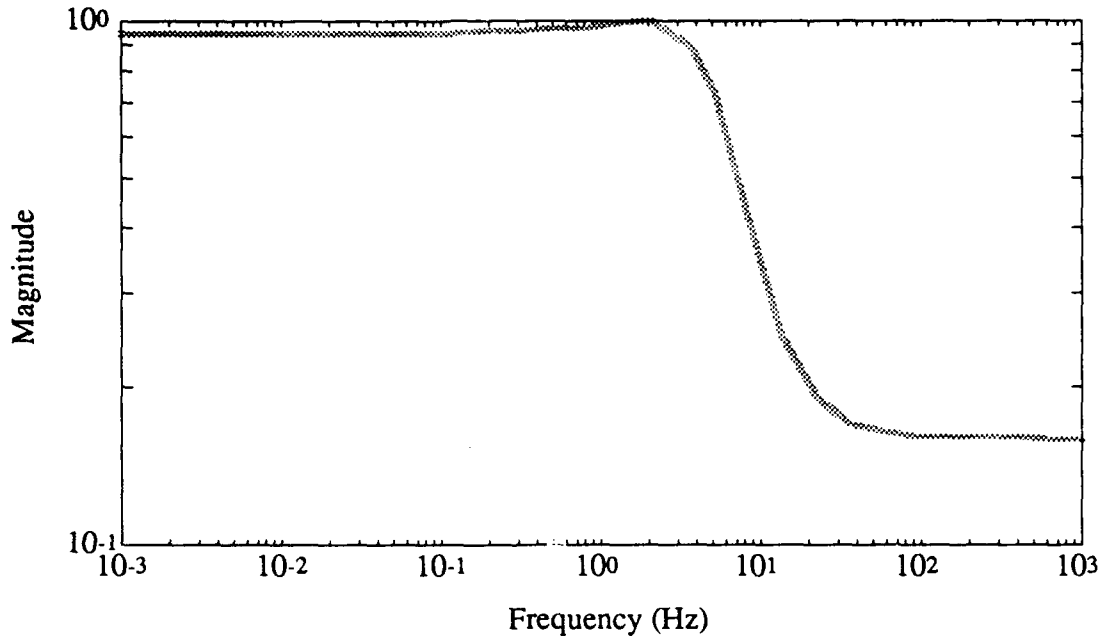


Figure 6.25: Structured Singular Value ( $\mu$ ) - Robust Performance - Case 2

and a plot of  $\mu$  is shown in Figure 6.25. It is seen that  $\mu$  is bounded by 1. Therefore, this controller yields robust performance for the deformable mirror system.

To complete the results for this case, the maximum singular value,  $\mu$ , and the spectral radius are shown in Figure 6.26. The primary reason  $\bar{\sigma}$  and  $\rho$  are calculated is to determine how well  $\mu$  was calculated and what benefit there may be in using  $\mu$ . The calculation of  $\mu$  in both case 1 and case 2 show the reduction expected from exploiting the structure of the uncertainty.

The results shown indicate that case 1 scales to the results for the full model. This provides a useful result. The amount of uncertainty tolerated can be determined in the single petal case and then applied to the full model case using 24 sensors. It will be shown below that this scaling does not hold entirely for the full model using 36 sensors.

It was again observed that for the initial set of sensors chosen for the 24 sensor case (see Chapter 5, Figure 5.3) the sensitivity function was unable to meet the performance requirement, even after relaxing the bounds on the control input function and the complementary sensitivity function. This initial set of sensors was compared with the sensors selected through the minimization of the condition number of the plant. The difference in the d.c. value of the condition number appears to be small in Figure 5.10. Perhaps the fact that the performance requirement could not be met with the original selection of the 24 sensors suggests only a numerical problem, but the best disturbance rejection properties were obtained using the sensors selected through the minimization of the plant condition number.



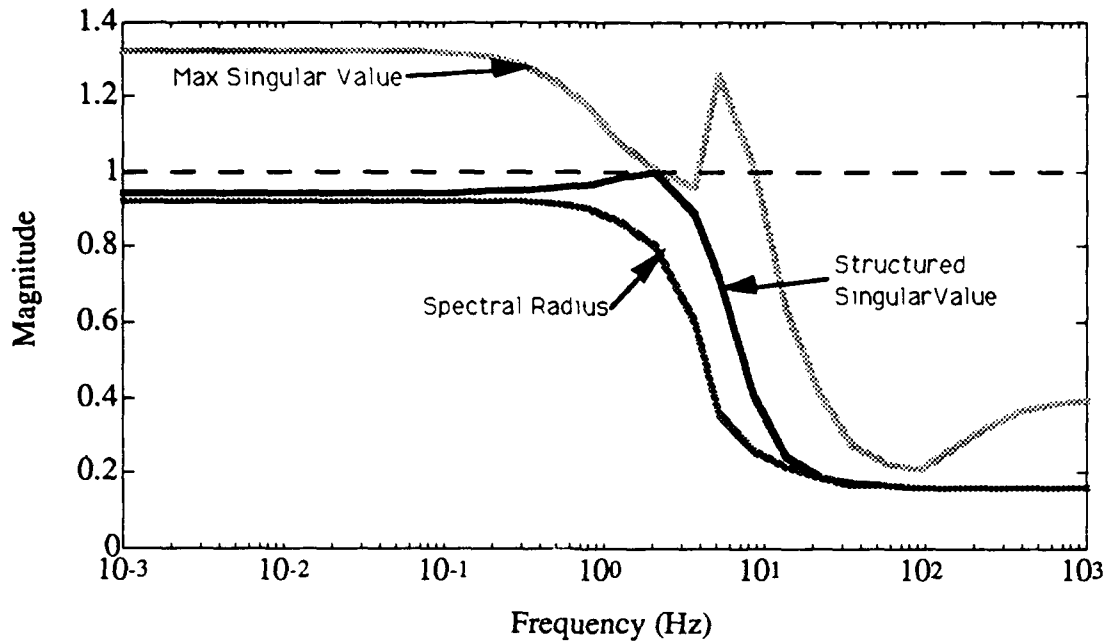


Figure 6.26:  $\bar{\sigma}$ ,  $\mu$ , and  $\rho$  Plots - Robust Performance - Case 2

### 6.3.3 Case 3: Full Model - 36 Sensors

The full model with 36 sensors utilizes the entire 6 petals with 36 inputs and 72 states. Again, the same weighting functions,  $l_H(s)$ ,  $l_T(s)$ , and  $C_c(s)$ , were applied to this model as to the two preceding cases and an  $H_\infty$  controller was calculated. As the number of sensors increases, so does the number of states of the sensor, sensitivity weighting matrix, and complementary sensitivity weighting matrix. The augmented state space now contains 180 states. The open-loop system loop gain,  $GK$ , contains 360 states. This case clearly illustrates the advantages of using transfer function matrix formats versus manipulating the state-space models to determine the various performance functions.

Using the same weighting matrices as for the above 2 cases, the  $H_\infty$  controller did not have a solution. This means that the bound shown in Equation 6.14 could not be satisfied with the current weighting functions. A reduction of the control input weighting constant by a factor of 3,

$$C_c = 1 \times 10^{-3}$$

enabled the calculation of an  $H_\infty$  controller.

Figure 6.27 shows the maximum singular value plot for the transfer function matrix between the disturbance input  $D_1$  and the weighted performance vector  $W$ . As with the prior 2 cases, Figure 6.27 shows that a valid solution was obtained for the  $H_\infty$  controller with the reduction of the control input weight. The assumption is that the added numerics of the additional sensors

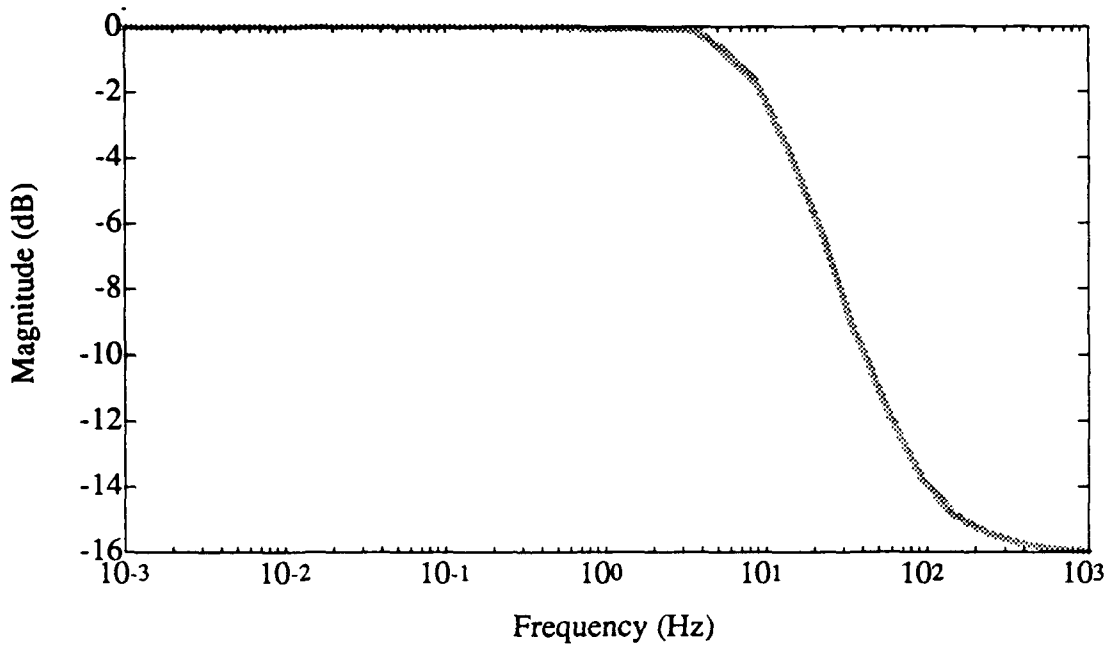


Figure 6.27:  $H_\infty$  Cost Function Singular Value Plot - Case 3

violated the bounds shown in the cost equation, Equation 6.14. For the full model case using 36 sensors, the bounds produced a problem with no solution. Relaxing the control input function bound enabled the solution of Equation 6.14.

The singular value plots of the sensitivity function and complementary sensitivity function are shown in Figure 6.28 and Figure 6.29. With the relaxed control input weighting function, the sensitivity singular values are “shaped” by the sensitivity weighting function,  $l_H(s)^{-1}$ , and the sensitivity function maximum singular value is bounded by this weight. The plot of the complementary sensitivity function is also bounded by the complementary sensitivity function weight,  $l_T(s)^{-1}$ . Figure 6.30 shows the singular value plot of the control input transfer function matrix,  $C_i(s)$ . Again, note that  $\bar{\sigma}(C_i(j\omega))$  has a similar shape when compared to the previous 2 cases.

The performance robustness was evaluated for the case of the reduced sensor uncertainty (same as case 2), and a plot of  $\mu$  is shown in Figure 6.31. It is seen that  $\mu$  is not bounded by 1. There is a small frequency range where  $\mu$  exceeds 1. Therefore, the full model using 36 sensors does not meet the performance robustness specification. It should be noted that in increasing the number of sensors from the full model using 24 sensors to the full model using 36 sensors, the performance vector increased in number of elements from 24 to 36. This induces a scaling difference that accounts for the fact that performance robustness was not maintained in this case.

When the uncertainty is reduced to a sensor accurate to within 0.1% for frequencies less than 1 Hz, the performance robustness can now be achieved for case 3. With the large dimensionality of

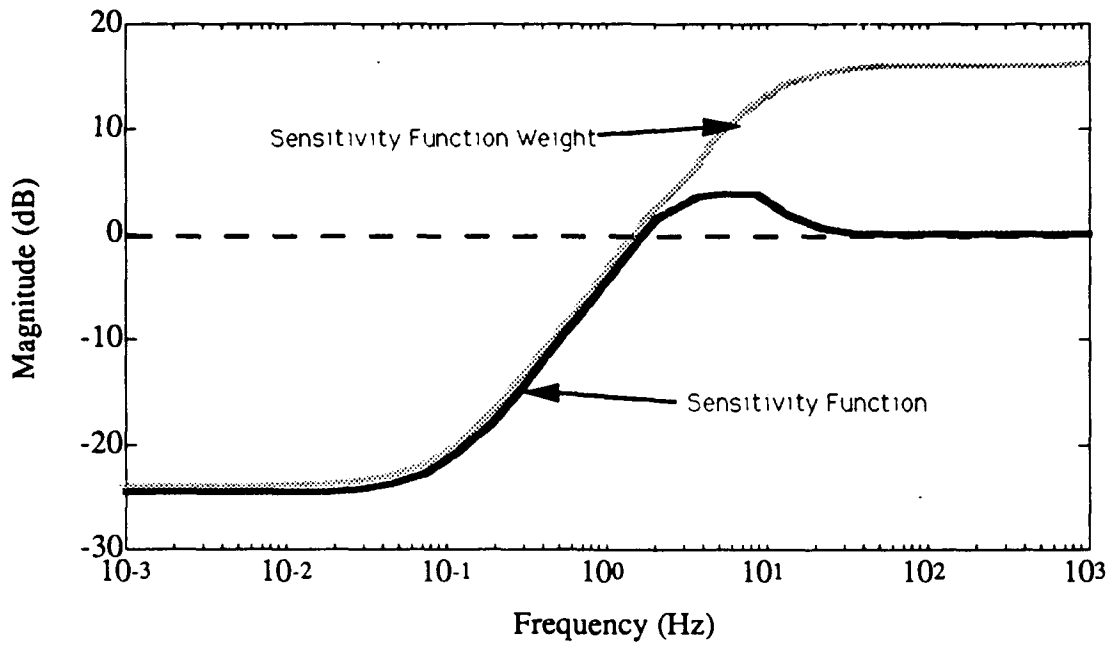


Figure 6.28: Singular Value Plot - Sensitivity Function - Case 3

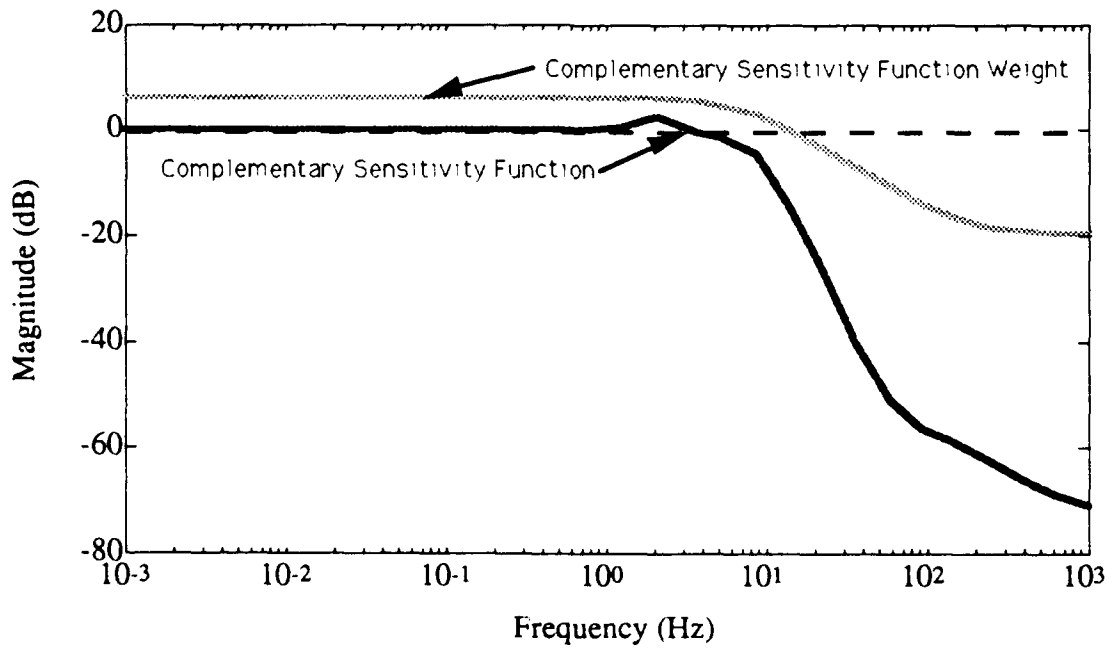


Figure 6.29: Singular Value Plot - Complementary Sensitivity Function - Case 3

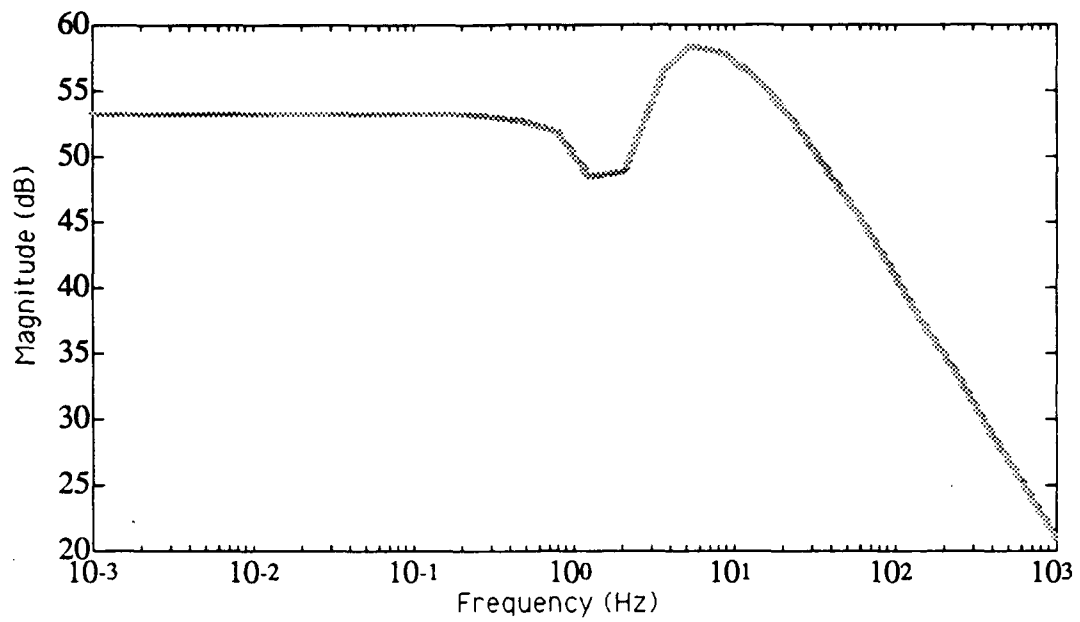


Figure 6.30: Singular Value Plot - Control Input Function - Case 3

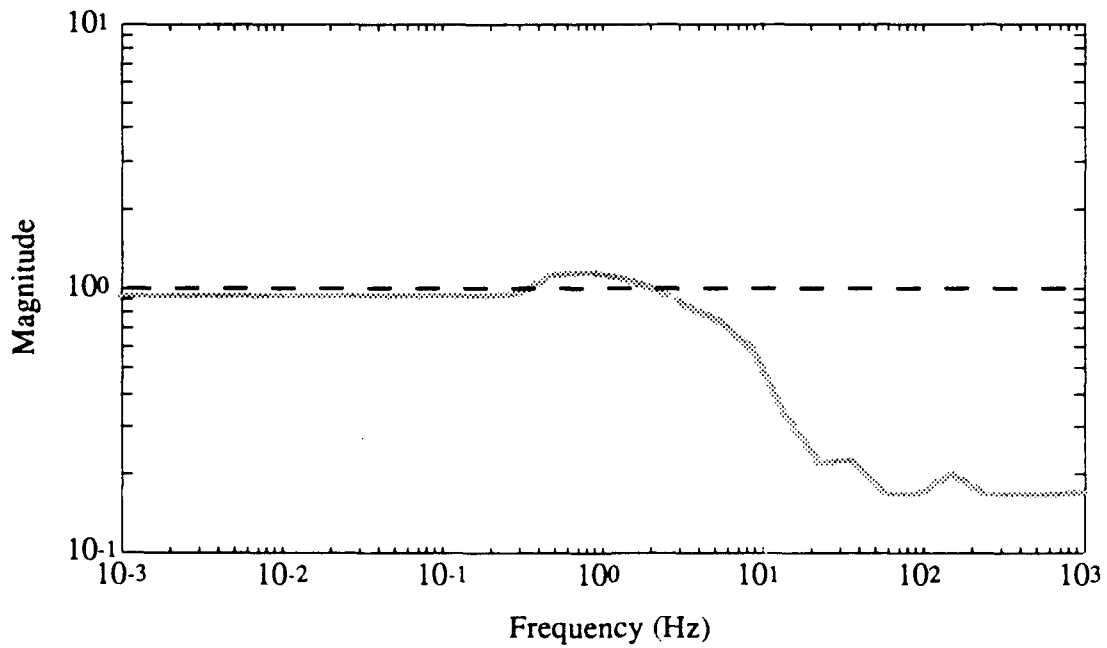


Figure 6.31: Structured Singular Value ( $\mu$ ) - Robust Performance - Case 3

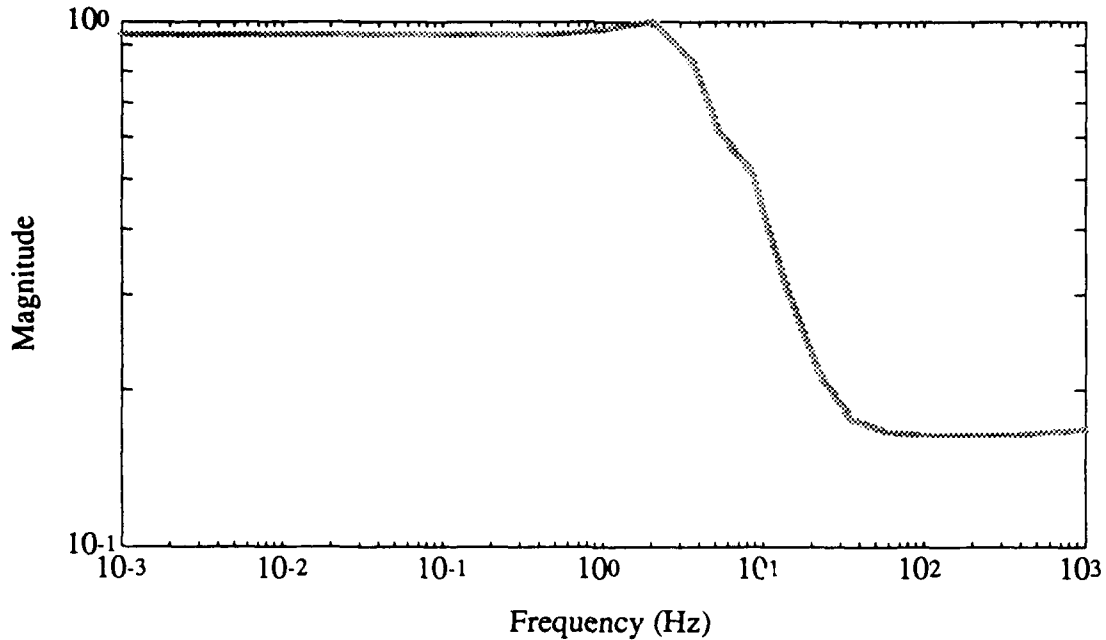


Figure 6.32: Structured Singular Value ( $\mu$ ) - Robust Performance - Case 3 - Reduced Sensor Uncertainty

the state-space for case 3, the prospect of iterating on sensor uncertainty is very time consuming. Figure 6.32 shows the plot of  $\mu$  for the robust performance case using the more accurate sensor.

The fact that an  $H_\infty$  control solution to Equation 6.14 could not be found for case 3 without reducing the control input weight demonstrates that caution needs to be used when extending the results from case 1 to case 3. The differences appear to be numeric, because as the control input weight was relaxed and the uncertainty was reduced, the results have the same “shape” as the results presented for case 1 and case 2. Based only on numerics, the additional sensors in case 3 negatively affected the results. For case 3, the uncertainty had to be reduced in order to meet the performance robustness specification.

The original sensor locations chosen in Figure 5.2 failed to yield a controller that attenuated the sensitivity function. All attempts at shaping the sensitivity function for the full model using 36 sensors failed except for the case where the condition number was minimized. It was observed that at least one singular value of the sensitivity function remained above 0 dB for low-frequencies. If the sensitivity function equation is examined again

$$H(s) = (I + G(s)K(s)S_e(s))^{-1}$$

the failure to “shape”  $H(s)$  appears to happen when

$$\underline{\sigma}((G(j\omega)K(j\omega)S_e(j\omega)) \approx 0$$

In other words, the product  $G(j\omega)K(j\omega)Se(j\omega)$  is singular.

## 6.4 Conclusions

This chapter has presented the  $H_\infty$  control solution results for three cases consisting of a single petal model, a full model using 24 sensors, and a full model using 36 sensors. It was observed that for the first two cases, the robust performance requirement could be met only for sensors accurate to within 1% for low frequencies. The results from the single petal model scaled to the second case, and without modifying weighting matrices or uncertainty, case 2 repeated the results shown for the single petal model. However, this was not the case for the full model using 36 sensors.

It was observed that for case 3, the additional 12 sensors used when comparing the results to case 2 negatively affected the robust performance. The control input weight was reduced in order to provide an  $H_\infty$  solution, and the sensor accuracy increased to 0.1%. This difference is attributed to the increase in the size of the performance vector from 24 measurements to 36 measurements.

Each of the original position locations first presented in Chapter 5 for the three cases were used to compare the impact of sensor selection and disturbance rejection. It was observed that the best disturbance rejection was found for the sensors chosen by minimizing the plant condition number. The example sensor locations chosen for the full model using 36 sensor was unable to attenuate the sensitivity function.

## Chapter 7

# Decentralized Control System Analyses

This chapter details the analyses applied to both the single petal model and the full model with 36 inputs and 36 outputs in an attempt to determine a decentralized control structure. The tests employed are necessary conditions that allow the designer to eliminate prospective structures very quickly and concentrate only on those structures that may yield adequate decentralized performance. This chapter is divided into four sections, detailing the importance of decentralized control, some simple tests for Decentralized Integral Controllability (DIC), the  $\mu$  interaction measure, and concluding with some decentralized performance degradation tests.

### 7.1 Importance of Decentralized Control

Let  $P(s)$  be a square,  $n \times n$  rational transfer function matrix relating the vector of system inputs  $u$  to the vector of system outputs  $y$ , and let  $e$  be the error signal input to the controller  $K$ . The vector inputs, outputs, and error signal are partitioned in the same manner with

$$u = [u_1, u_2, \dots, u_m]^T$$

$$y = [y_1, y_2, \dots, y_m]^T$$

$$e = [e_1, e_2, \dots, e_m]^T$$

For this thesis, the definition of decentralized control means that

$$u_i = K_i e_i$$

Rearranging the input-output maps allows the controller to be defined as block-diagonal.

Figure 7.1 shows the block-diagonal structure of the controller. By constraining the controller to this block-diagonal structure, performance degradation is expected when compared to a "full"

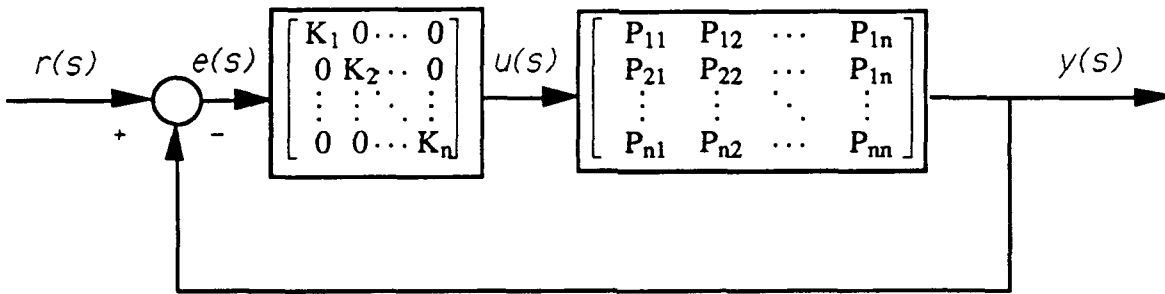


Figure 7.1: Diagonal Controller Block Diagram

centralized controller (i.e.  $K_{ij} \neq 0 \ i \neq j$ ). The advantages gained by using a block-diagonal controller can result in simplifying both the hardware required and the design procedure [16].

For cases such as electric power stations,  $u_i$  and  $y_i$  could be physically close but  $u_i$  and  $y_j$  ( $i \neq j$ ) might be separated by long distances. The communication links required of a centralized controller in this case would be very expensive. The fact that the decentralized controller could significantly simplify the hardware is a trade that needs to be made when addressing the performance. Decentralized control also can allow for separate subsystems to fail without catastrophic impact on system performance. If the controller for the large power networks was centralized, a failure in the controller could result in the loss of power for large areas of the country. This does not occur because decentralized controllers can localize the failure as well as the control.

If the plant that needs to be controlled is also block diagonal (i. e.  $P_{ij} = 0 \ (i \neq j)$ ), then each controller  $K_i$  can be designed for the isolated subsystem  $P_{ii}$  with no loss in performance. Extending this idea slightly, if  $P_{ij}$  is "small", then it should still be possible to design a controller  $K_i$  with a "small" loss in performance. The advantage of the block-diagonal controller is that fewer controller parameters need to be chosen than for the centralized case. It is very important that at the minimum, stability is maintained if a failure occurs in a controller sub-block.

To design decentralized controllers, two problems need to be addressed. The first issue involves which inputs should be paired with which outputs. The second issue is how to design each individual controller block. As shown in Chapter 4, the pairing problem can produce many different combinations. Therefore, efficient and simple tests are needed to reduce the number of control structure possibilities to a manageable level. The tests employed in this thesis are necessary conditions used to eliminate structures that will not maintain stability or a measure of performance. The second issue concerning the control design has already been presented, in part, through Chapter 6. Once a structure has been identified, the design of each individual block can be done with the



method that best suits the problem ( $H_2$ ,  $H_\infty$ , Classical Techniques, etc.).

An important point to note is that these tests only use open-loop plant information. Therefore, the application of these tests utilize information that should be available. By manipulating different interactions of the plant structure, these necessary conditions can reduce the number of potential structures that are not decentralizable.

## 7.2 Necessary Conditions for Decentralized Integral Controllability

This section describes the tests that can be used for Decentralized Integral Controllable (DIC) plants and presents results of the application of these tests to the single petal model.

### 7.2.1 Description of Tests

A centralized controller uses the complete plant output information to correct for the error. There is normally some cross-coupling that does not make it possible to totally decouple the system into a block-diagonal structure. Therefore, the coupled error from the off-diagonal blocks normally leads to a degradation in performance as compared to the performance obtained in using a centralized controller. This section describes some tools that are used in the deformable mirror system to determine the existence of a decentralized structure.

For a system to be Decentralized Integral Controllable (DIC) [16], the closed-loop system shown in Figure 7.1 must be stable and each individual decentralized closed-loop system must be stable. This means that the loss of a "channel" of information does not affect the entire stability of the closed-loop system. Unfortunately, necessary and sufficient conditions do not exist for DIC. So, tests for DIC are only necessary conditions. These tests are meant to reduce the set of possible controllers to a manageable set. The five necessary conditions are shown in Equation 7.1 through Equation 7.5 [Morari [16], p. 363-364].

$$\det(P^+(0)) > 0 \quad (7.1)$$

$$\operatorname{Re}\{\lambda_i(P^+(0)C(0))\} \geq 0 \quad \forall i, \text{ for all diagonal } C(0) \geq 0 \quad (7.2)$$

$$\operatorname{Re}\{\lambda_i(P^+(0))\} \geq 0 \quad \forall i \quad (7.3)$$

$$\operatorname{Re}\{\lambda_i(L(0))\} \geq -1 \quad \forall i, \text{ where } L = (P - \tilde{P})\tilde{P}^{-1}, \quad \tilde{P} = \operatorname{diag}[F_{ii}, \dots, P_{nn}] \quad (7.4)$$

$$\text{RGA: } \lambda_{ii}(P(0)) > 0 \quad \forall i \quad (7.5)$$

These conditions are proven in [16], where  $P^+(0)$  is derived from setting the diagonal elements of  $P(0)$  to positive values, and the RGA refers to the Relative Gain Array, which is defined as

$\Lambda(M)^1 = Mx(M^{-1})^T$ . As presented above, these conditions are for a completely decentralized case, i.e., the controller is diagonal. Most of these results can be extended to the block-diagonal case. In this thesis, the tests are used as shown above.

Equation 7.1 is implied by Equation 7.3 and is therefore redundant. Equation 7.2 is difficult to apply due to the need of a controller. With the emphasis in this thesis on open-loop plant tests, Equation 7.2 will not be used. Therefore, the tests shown in Equation 7.3 through Equation 7.5 are used to evaluate DIC for the single petal model (i.e., the case 1 model used in Chapter 6). Using these three necessary conditions, test 1 refers to the conditions implied by Equation 7.3, test 2 refers to the conditions implied by Equation 7.4, and test 3 refers to the conditions implied by Equation 7.5.

### 7.2.2 Results of Application of DIC Tests to the Single Petal Model

As discussed above, these conditions are only necessary, simple tests to determine if a system is DIC. It is important to remember that a particular system that satisfies these tests is not necessarily DIC. On the other hand, a system that does not satisfy these tests is not DIC. Therefore, the true utility of these tests is to eliminate structures that are not DIC through the failure of one of the tests.

Equation 7.3 through Equation 7.5 were applied to the single petal model. To aid in the discussion of these tests, Figure 7.2 shows the single petal with sensors numbered and the actuators, located in the center, numbered. Using the set of all possible input-output pairings, each of the three tests were applied to the plant's d.c. gain

$$P(0) = D - CA^{-1}B$$

The first test requires  $P^+(0)$ . This matrix is derived from  $P(0)$  by multiplying each column in  $P(0)$  containing a negative diagonal element by -1. This makes all of the diagonal elements of  $P^+(0)$  positive. The requirement for  $P^+(0)$  is obtained as a result of specifying that all individual loops must be stable [16]. Using Equation 7.3, 10 possible DIC structures were found. They correspond to the following pairs using the same input actuator ordering. These results are shown in Figure 7.3, which also shows that actuators acting in the "z-axis" are paired with sensors that sense "z" displacements while actuators acting in the plane are sensed by tangential and radial sensors. Although these 10 possible structures look promising, the other two tests need to be used to determine if a structure exists that passes all three tests.

The second test from Equation 7.4 was used to find input-output pairings in a similar manner as test 1. All possible pairings were tested. The matrix,  $L(0)$ , plays a key role in determining the

<sup>1</sup>Here, x refers to an element by element multiplication.

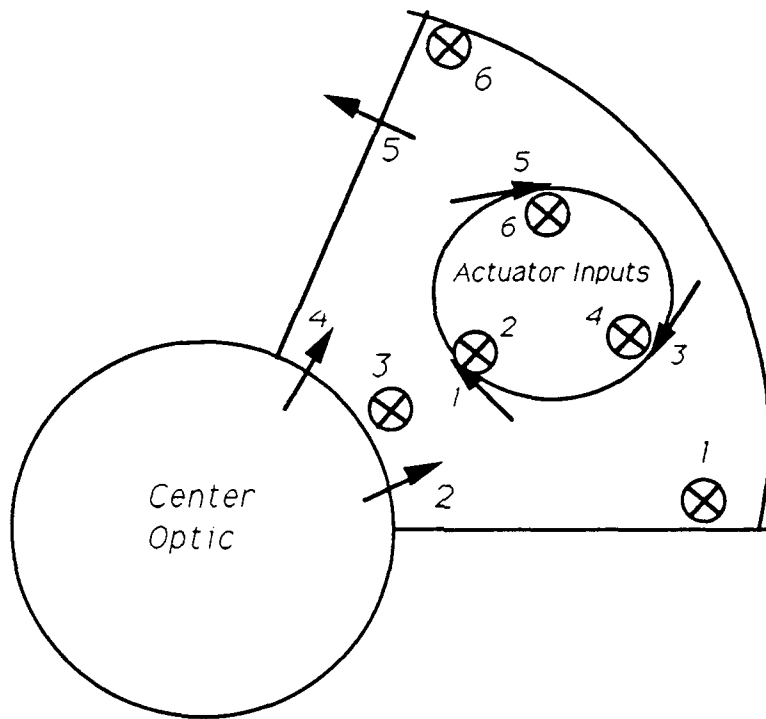


Figure 7.2: Single Petal Showing Actuator and Sensor Numbers

Input Number	Sensor Number									
1	2	2	2	2	4	4	4	4	5	5
2	1	1	3	3	1	1	3	3	1	3
3	4	5	4	5	2	5	2	5	2	2
4	3	3	1	1	3	3	1	1	3	1
5	5	4	5	4	5	2	5	2	4	4
6	6	6	6	6	6	6	6	6	6	6

Figure 7.3: Input-Output Ordering of Possible DIC Structures Using Test 1

Input Number	Sensor Number																		
1	1	1	2	2	2	2	2	4	4	4	4	4	4	5	5	5	5	6	6
2	3	3	1	1	3	3	3	1	1	1	3	3	3	1	1	3	3	1	1
3	2	5	4	5	4	5	5	2	5	6	1	2	5	2	6	1	2	2	5
4	4	4	3	3	1	1	1	3	3	2	2	1	1	3	2	2	1	4	4
5	5	2	5	4	5	4	6	5	2	5	5	5	2	4	4	4	4	5	2
6	6	6	6	6	6	6	4	6	6	3	6	6	6	6	3	6	6	3	3

Figure 7.4: Input-Output Ordering of Possible DIC Structures Using Test 2

Input Number	Sensor Number																	
1	2	2	2	2	3	3	4	4	4	4	5	5	5	5				
2	1	1	3	3	1	1	1	1	3	3	1	1	3	3				
3	4	5	4	5	2	5	2	5	2	5	2	4	2	4				
4	3	3	1	1	4	4	3	3	1	1	3	3	1	1				
5	5	4	5	4	5	2	5	2	5	2	4	2	4	2				
6	6	6	6	6	6	6	6	6	6	6	6	6	6	6				

Figure 7.5: Input-Output Ordering of Possible DIC Structures Using Test 3

relative errors arising from the use of a diagonal plant,  $\bar{P}$ , instead of the full plant,  $P$ . Through testing the real part of the eigenvalues of  $L(0)$ , the input-output pairs shown in Figure 7.4 were found that meet the bounding requirement of Equation 7.4. It can be seen from examination of Figure 7.4 that 19 input-output pairs meet the requirements of Equation 7.4. Also, 10 of the 19 input-output pairs are the same 10 input-output pairs that passed the first test. These 10 input-output pairs are shaded in Figure 7.4.

The third test using Equation 7.5 was then employed. By its name, the Relative Gain Array (RGA) provides information on the condition or relative gain of a plant. The advantages in using the RGA are

1. The RGA is scaling independent.
2. All rows and columns of the RGA sum to one.

The second advantage of the RGA will be exploited in Section 7.4. The test described by Equation 7.5 uses the RGA as another necessary condition for DIC. The single petal model had 14 sensor pairs that satisfied Equation 7.5, and these results are shown in Figure 7.5. It can be seen that the same 10 input-output pairs that met requirements from both the first and second tests also meet the requirements from Equation 7.5. Therefore, any of these potential input-output pairs may produce a decentralized integral controller. Remember that Equation 7.2 was not used.

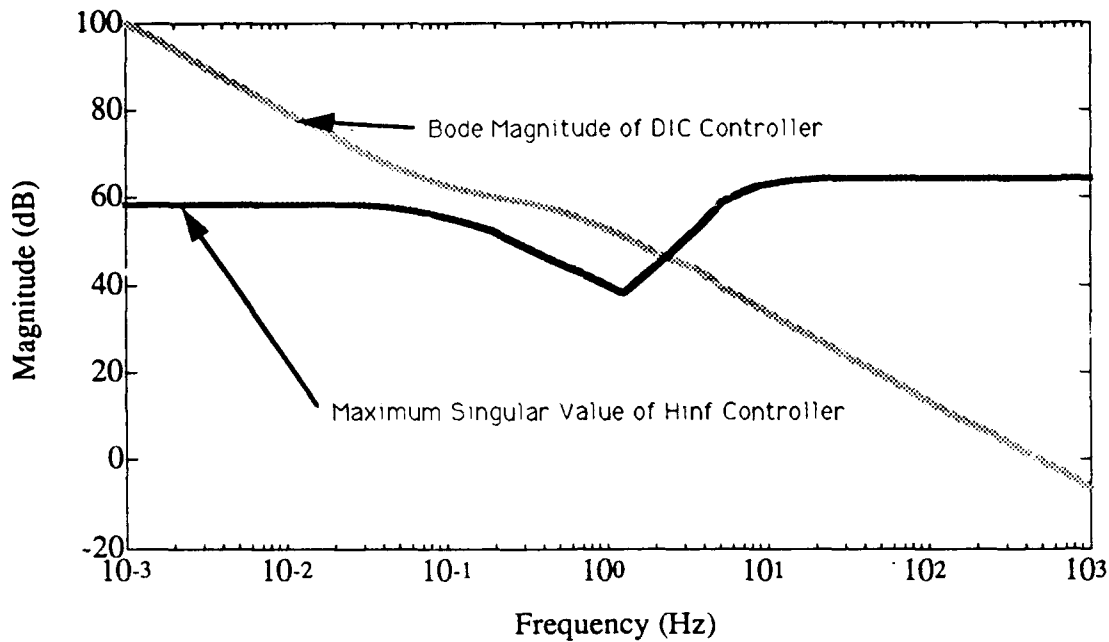


Figure 7.6: Comparison of DIC Controller Magnitude and Hinf Controller Magnitude

Using these results, a DIC controller was designed for the single petal model. The input-output pairing selected was  $\{[1, 4], [2, 3], [3, 2], [4, 1], [5, 5], [6, 6]\}$  corresponding to column 7 in Figure 7.3 where the notation,  $[Input\#, Output\#]$  is used. A simple lead-lag filter was used for the controller,  $K(s)$ , for each SISO pair. It was found that a sufficient design could be obtained using the same lead-lag filter for each SISO plant, and therefore, the diagonal controller developed has the form

$$K(s) = k_f(s)I \quad (7.6)$$

The SISO representation for  $k_f(s)$  is

$$k_f(s) = 3000 \frac{s + 0.6}{s(s + 3)} \quad (7.7)$$

Using Equation 7.7, the bode magnitude plot of the controller is shown in Figure 7.6. Also shown in Figure 7.6 is the maximum singular value of the single petal model controller calculated in Chapter 6 using  $H_\infty$  synthesis techniques. Note the attenuation at 2 Hz of the  $H_\infty$  controller. The simple lead-lag filter does not produce the same attenuation at 2 Hz, and it will be seen that this lack of attenuation will result in a decrease in the performance. The  $H_\infty$  controller attenuates the primary resonant frequency through the use of a notch-filter type of performance. It will be shown below that the DIC controller designed from Equation 7.7 has difficulties with the  $\approx 2$  Hz resonance.

Using the controller from Equation 7.7, the SISO sensitivity transfer functions were calculated (Equation 6.3). The results are shown in Figure 7.7. Also shown in Figure 7.7 is the sensitivity

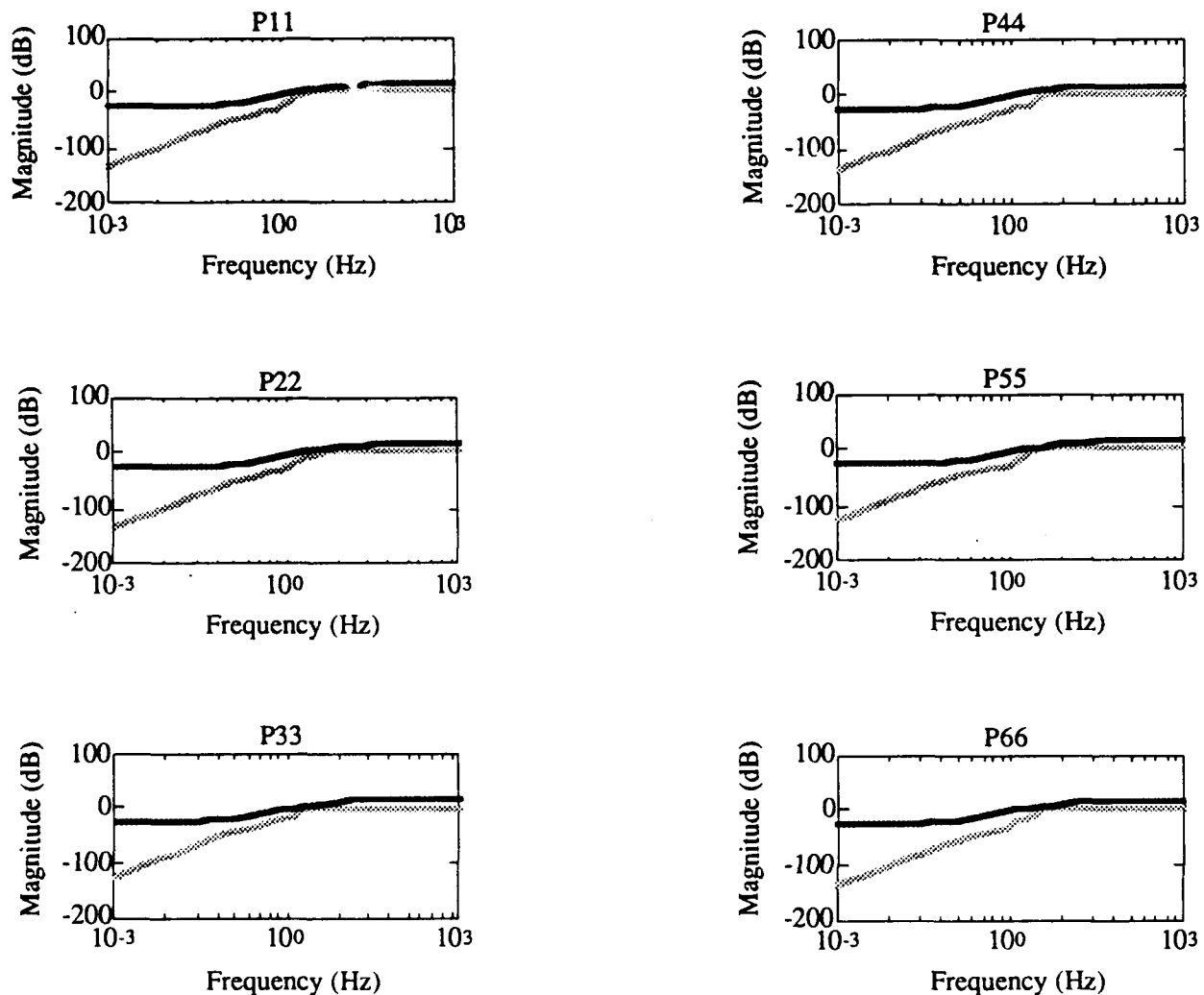


Figure 7.7: SISO Sensitivity Transfer Functions - DIC

weighting function bound used in Chapter 6. This bound was used as a performance level for each SISO system.

When each of the SISO controllers is combined to form  $K(s)$ , the evaluation of the sensitivity matrix transfer function, complementary sensitivity matrix transfer function, and control input matrix transfer function can be completed in a similar manner to Chapter 6. For this evaluation, the full plant,  $P(s)$ , is used. This becomes an analysis exercise with the controller synthesized from Equation 7.6 instead of an  $H_\infty$  controller. The results from this evaluation are shown in Figure 7.8. As can be seen from this figure, the sensitivity matrix transfer function is bounded by the original weight at almost all frequencies except around 2 Hz. Reexamination of Figure 7.7 does not show the individual SISO sensitivity functions exceeding the bound. No modification of the gain or cut-off frequencies in Equation 7.7 for the individual SISO controllers was able to “force”

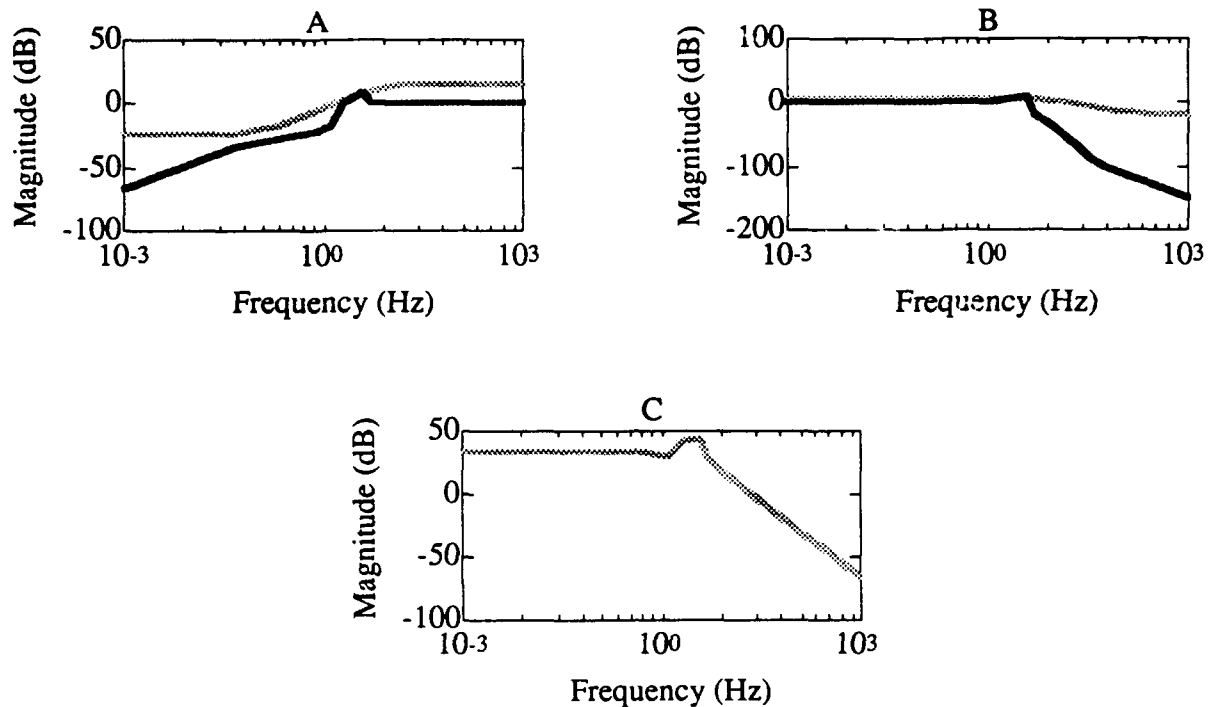


Figure 7.8: Matrix Transfer Functions Using DIC; A: Sensitivity Function and Sensitivity Weight, B: Complementary Sensitivity Function and Complementary Sensitivity Function Weight, C: Control Input Function

the matrix sensitivity function to remain within the performance bounds at  $\approx 2$  Hz. The same “peaking” at  $\approx 2$  Hz is also seen in the matrix complementary transfer function and the matrix control input transfer function in Figure 7.8. Therefore, nominal performance is not maintained, and we expect that performance robustness can not be maintained.

Using the controller from Equation 7.6, the performance robustness using a sensor accurate to 1% over low frequencies was tested. The plot of  $\mu$  is shown in Figure 7.9. Robust performance cannot be maintained as shown in Figure 7.9. The frequency scale in Figure 7.9 again shows that  $\mu$  exceeds 1 at frequencies between 2 Hz and 4 Hz.

The sensor uncertainty was reduced by a factor of 100 requiring a sensor accurate to within 0.01% at low frequencies. Again, the performance robustness was tested, and the plot of  $\mu$  using this more accurate sensor is shown in Figure 7.10. Again, performance robustness cannot be maintained. Additional tests continued to reduce the sensor uncertainty, but  $\mu$  exceeded 1 for each of these additional tests. This is caused in part by the inability of the controller to attenuate the  $\approx 2$  Hz resonance of the plant. The controller could not maintain nominal performance.

Finally, the performance requirement was reduced by 82%, and the plot of  $\mu$  is shown in Figure 7.11. This plot shows that robust performance can now be maintained. This result is verified

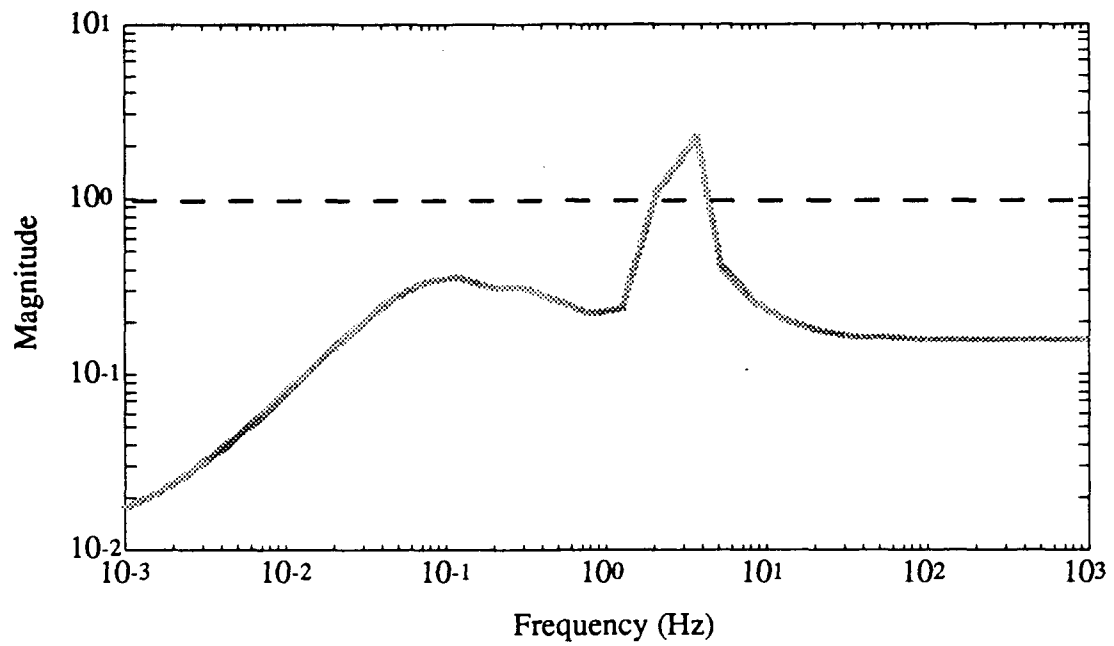


Figure 7.9: Robust Performance - Single Petal Model Using DIC

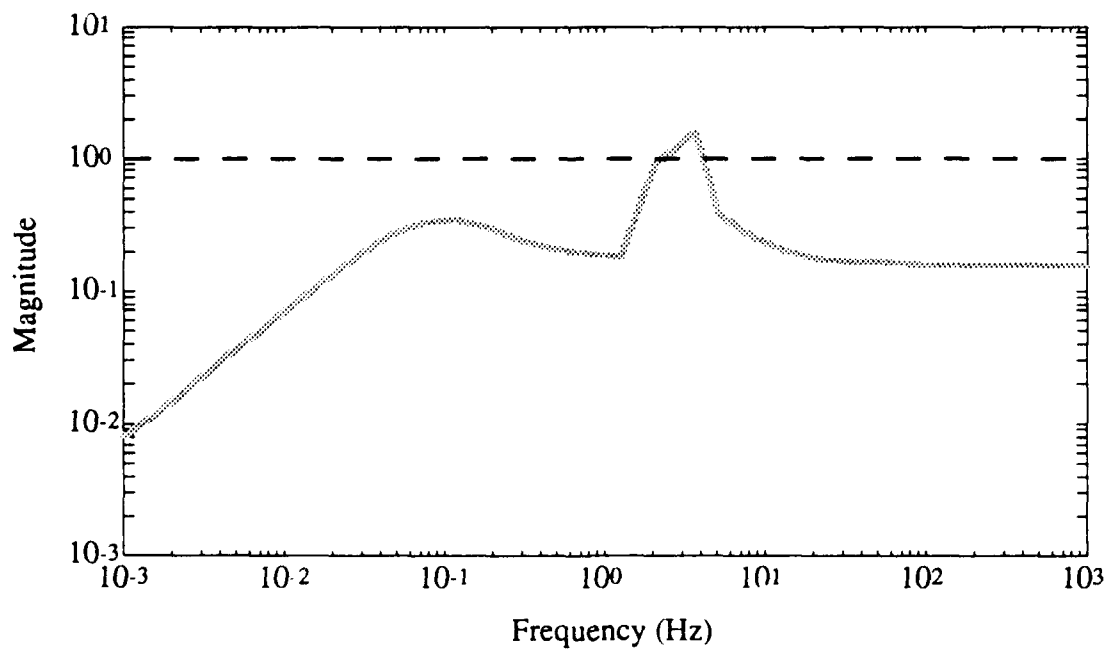


Figure 7.10: Robust Performance - Single Petal Model Using DIC - Reduced Uncertainty



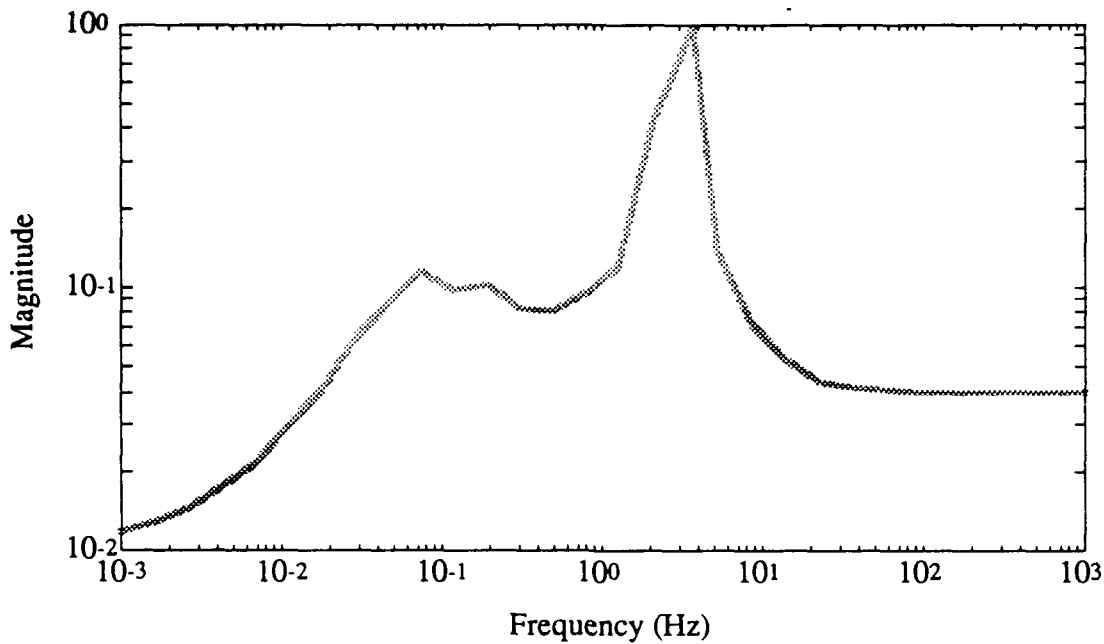


Figure 7.11: Robust Performance - Single Petal Model Using DIC - Reduced Performance

in part by results shown in Section 7.4 described below. In order to maintain performance robustness using a diagonal integral controller of the form Equation 7.6, the performance requirement needed to be reduced.

This simple example shows the usefulness of the simple DIC tests and the ease in applying these tests to a given model. The tests showed that 10 input-output pairs should yield proper structures for decentralized integral control. A very simple SISO controller was designed to meet the original performance requirement on each SISO plant, and then each SISO controller was combined to form a system controller for the  $6 \times 6$  single petal model. It was found that performance had to be lowered in order to assure robustness. This is a trade that occurs often in decentralized problems. The benefit of using a decentralized controller needs to be weighed against the cost of the loss in performance. The  $H_\infty$  controller solution notched out the 2 to 4 Hz frequency band to meet the performance requirement. A modification to the SISO controller in Equation 7.7 to attenuate the 2 Hz resonance might provide better performance.

### 7.3 $\mu$ Interaction Measure

Another test of DIC and performance degradation due to a block-diagonal controller is called the  $\mu$  interaction measure [10]. The purpose of an interaction measure is to determine the performance degradation caused by a block-diagonal controller. This section defines a specific interaction measure that, when obtained using the structured singular value, provides a sufficient condition for

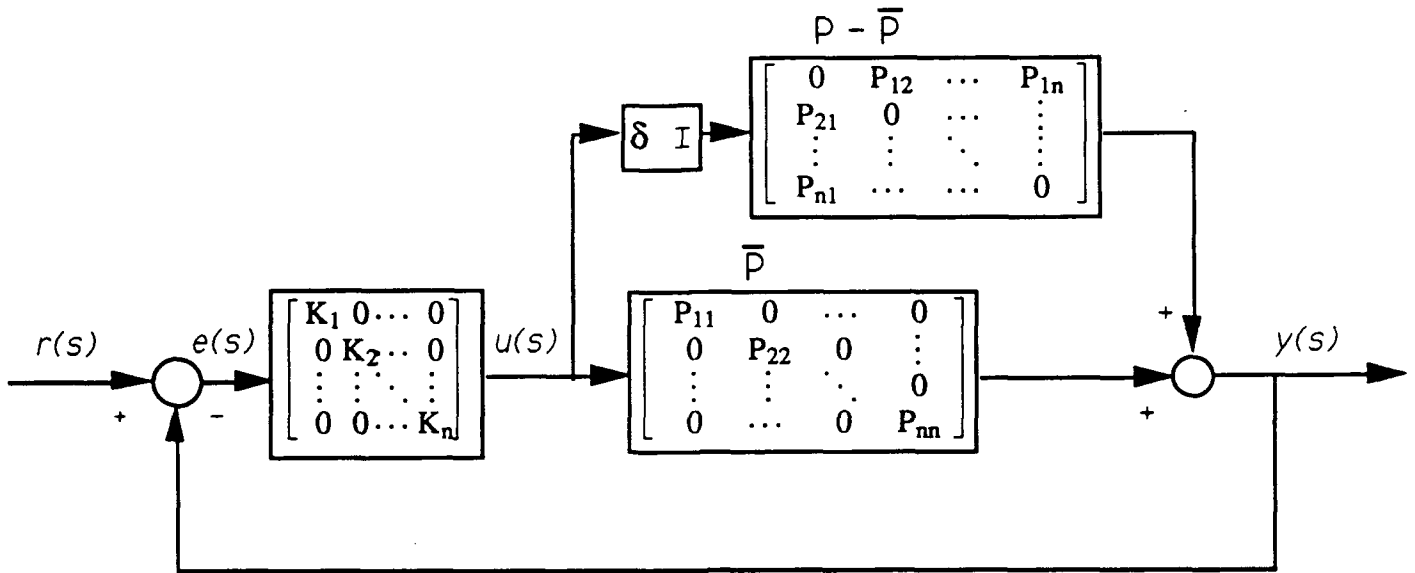


Figure 7.12: Representation of Off-Diagonal Portion of Plant as Uncertainty

achieving DIC. The  $\mu$  interaction measure is applied to the single petal model, and the results are compared with the results from Section 7.2.

### 7.3.1 Definition

The controller,  $K(s)$ , is assumed to be block-diagonal and partitioned as described in Section 7.1. Utilizing the block-diagonal representation of the plant, the off-diagonal portion of the plant can be represented as an uncertainty block. This can be shown by manipulating Figure 7.1, and Figure 7.12 results, where  $\delta$  is a constant. The closed-loop system with the transfer function matrix

$$\bar{H}(s) = \bar{P}(s)K(s)(I + \bar{P}(s)K(s))^{-1} \quad (7.8)$$

should remain stable (set  $\delta = 0$  in Figure 7.12). The interaction measure imposes constraints on the choice of  $\bar{H}(s)$  to guarantee that the full closed-loop system

$$H(s) = P(s)K(s)(I + P(s)K(s))^{-1} \quad (7.9)$$

is stable ( $\delta = 1$ ).

Through manipulations described in [10], the following matrix describing the "relative error" becomes important in this analysis

$$E(s) = (P(s) - \bar{P}(s))\bar{P}(s)^{-1} \quad (7.10)$$

Note that this expression for  $E(s)$  matches the d.c. condition of Equation 7.3.

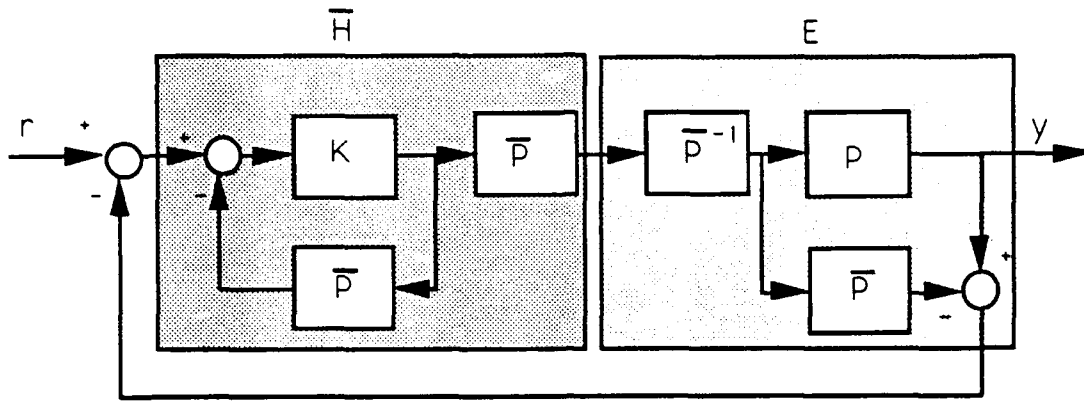


Figure 7.13: Equivalent Block-Diagram Representation Emphasizing Interaction Measure

To further aid in understanding the utility of Equation 7.10, Figure 7.12 can be rearranged ( $\delta = 1$ ) into the equivalent form shown in Figure 7.13 which provides a form to observe the effects of “large” errors,  $E$ , on the closed-loop system,  $\bar{H}$ . Applying the multivariable Nyquist criterion to Figure 7.1, it is shown in [10] that when  $E(s)$  is “large”,  $\bar{H}(s)$  has to be “small” to avoid encirclements of the origin, but “small”  $\bar{H}(s)$  implies poor performance. This illustrates the constraints on  $\bar{H}(s)$  imposed by  $E(s)$ . If the relative error,  $E(s)$  is “large”, performance will suffer. The following theorem defines this constraint using the structured singular value as a measure on the “size” of  $E(s)$ .

**Theorem 7.1:** [Grosdidier, et al. [10], p. 312] *Assume that  $P(s)$  and  $\bar{P}(s)$  have the same right-half plane poles and that  $\bar{H}(s)$  is stable. Then the closed-loop system  $H(s)$  is stable if*

$$\bar{\sigma}(\bar{H}(j\omega)) \leq \mu^{-1}(E(j\omega)) \quad \forall \omega \quad (7.11)$$

**Proof:** See [10].

The computation of  $\mu(E(j\omega))$  uses an uncertainty structure with sub-blocks dimensioned according to the block-diagonal plant  $\bar{P}$ . Therefore, this is the “tightest” norm bound available, because the structure of the block-diagonal plant is taken into consideration. Theorem 7.1 provides a bound on the block-diagonal closed-loop transfer function matrix,  $\bar{H}(s)$ , using information from the relative error. This bound can be applied in a similar manner as the bounds in Chapter 6 for the complementary sensitivity function. The information for  $E(j\omega)$  is available based only on information of the plant and the block-diagonal structure of the plant. Equation 7.11 can be manipulated into a sufficient condition on DIC, and the following result can be used

$$\mu(E(0)) < 1 \quad (7.12)$$

Equation 7.12 was applied to the single petal model using the SISO system determined in

Section 7.2 to compare with the results obtained using Equation 7.3 through Equation 7.5. This comparison was done using the 10 input-output pairs that passed the three conditions in Equation 7.3, Equation 7.4, and Equation 7.5.

The structured singular value was computed for each of the ten cases shown in Figure 7.3. As shown in Equation 7.12,  $\mu(E(0)) \leq 1$  is a sufficient condition for DIC. The form of Equation 7.11 uses  $\mu^{-1}(E(j\omega))$ . The use of Equation 7.11 provides a bound on the closed-loop transfer function. Therefore, an equivalent condition to Equation 7.12 is

$$\mu^{-1}(E(0)) > 1 \quad (7.13)$$

Equation 7.13 was used, and the resulting  $\mu^{-1}(j\omega)$  plots are shown in Figure 7.14.

It can be seen from Figure 7.3 that the only input-output pair that passed the conditions of Equation 7.3 through Equation 7.5 was the input-output pair of  $\{[1, 4], [2, 3], [3, 2], [4, 1], [5, 5], [6, 6]\}$ . The plot for Column 7 shown in Figure 7.14 does indeed produce a system that is DIC. This confirms the results obtained when designing a decentralized integral controller. These plots can also provide performance information. Again looking at the plot for Column 7, the achievable closed-loop bandwidth is limited to  $\approx 2$  Hz. This is the same bandwidth that was observed in Figure 7.8.

The application of the  $\mu$  interaction measure was relatively easy using the single petal model with a diagonal controller structure. As the system size increases, the calculation of  $\mu$  becomes more difficult and time-consuming. The information provided from this test allows the designer to determine the performance limitations of the closed-loop decentralized system by calculating the structured singular value of the relative error of the open-loop full plant to the open-loop block-diagonal plant. The results presented in Figure 7.14 illustrate a more stringent test on DIC than Equation 7.3 through Equation 7.5, but at the cost of a much more difficult calculation.

Another test for performance degradation was recently developed and is presented in Section 7.4 below. An attractive feature of the viability tests is the ease of calculation and ability to test numerous combinations of structures quickly and efficiently.

## 7.4 Necessary Tests for Viability of Control Configurations

Within the last year, D. Reeves, C. Nett, and Y. Arkun developed a practical test that focuses on the existence of a control configuration for decentralized control as described above [18]. This section describes necessary conditions used to test for viability of control configurations and details the results of these tests applied to the single petal model and the full model using 36 sensors.

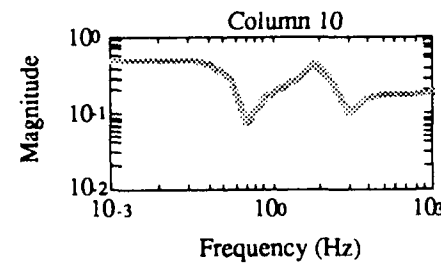
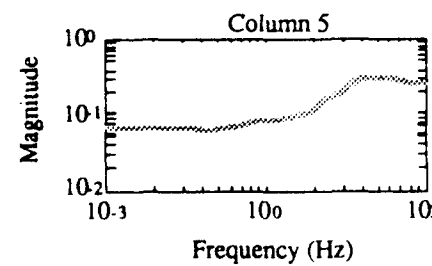
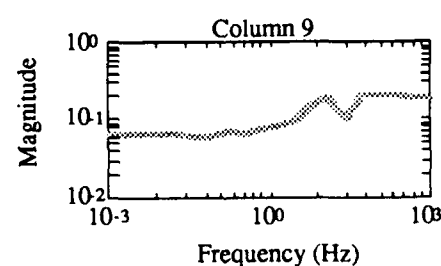
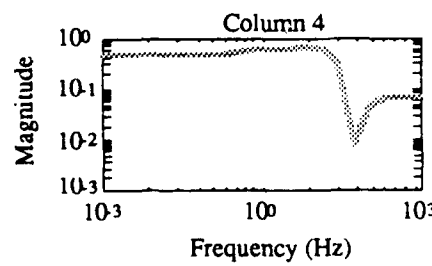
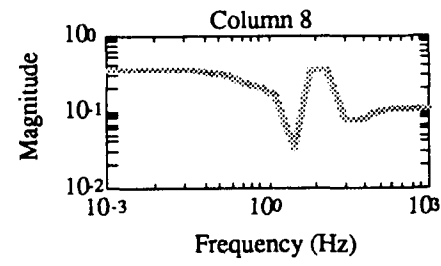
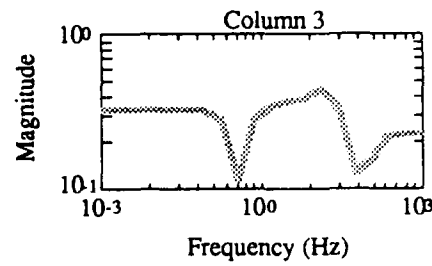
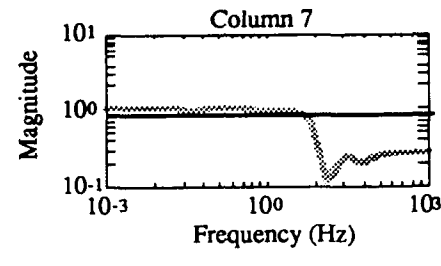
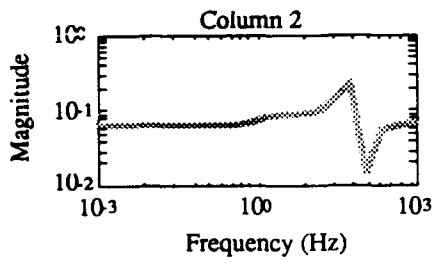
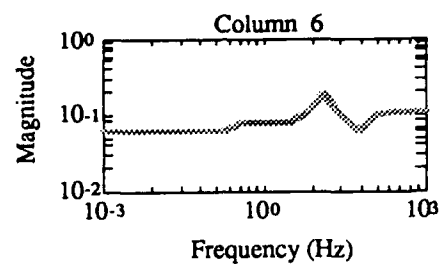
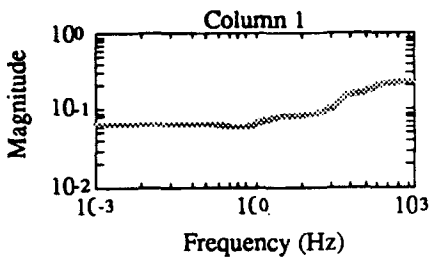


Figure 7.14: Interaction Measure Plots for DIC Cases

### 7.4.1 Discussion and Theorem

As shown in [18], partitioning leads to a decentralized control scheme. By determining the proper input-output blocks, a plant can be block-diagonalized (i.e., the plant can be partitioned into independent subsystems), and decentralized control can be applied to the full plant model. Therefore, a partitioned system implies subsystems that can be controlled independently. A centralized controller uses cross-feed information (off-diagonal information) to develop the control inputs, while a decentralized controller "ignores" the cross-feed terms. As stated above, decentralized control occurs when the matrix representation of the controller is block-diagonal. Overall performance is normally degraded due to the absence of the cross-feed. Reeves, Nett, and Arkun derived a necessary condition for low cross-feed performance degradation. This condition allows the control designer to "sort" through the potential decentralized configurations by searching over the set of possible subsystems and producing a quantitative measure of cross-feed performance degradation.

The test employed is defined by looking at the effect of cross-feed degradation on the closed-loop performance of the system using the full information from the plant  $P$  versus the loss in performance using the block diagonal plant  $\bar{P}$ . If  $P$  does not contain any cross-feed (off-diagonal block) terms, meaning  $P$  is already block-diagonal, there would be no loss in performance. Closed-loop performance is compared for the complementary sensitivity function of the full plant

$$H = PC(I + PC)^{-1}$$

versus the complementary sensitivity function of the block-diagonal plant

$$\bar{H} = \bar{P}C(I + \bar{P}C)^{-1}$$

If the difference,  $H - \bar{H}$  is studied, the maximum cross-feed performance degradation can be defined by [18]

$$\max_{r \neq 0} \frac{\|(H - \bar{H})r\|_2}{\|\bar{H}r\|_2} = \bar{\sigma}[(H - \bar{H})\bar{H}^{-1}] \quad (7.14)$$

This is the worst case cross-feed performance degradation over all possible reference inputs. The following theorem presents a viability criterion for low cross-feed performance degradation [18].

**Theorem 7.2:** [Reeves, et al. [18]] *Suppose  $P$  is a square finite dimensional linear time invariant (FDLTI) plant with its measurements and manipulations partitioned such that*

$$P = [P_{ij}] = \begin{bmatrix} P_{11} & \cdots & P_{1n} \\ \vdots & \vdots & \vdots \\ P_{n1} & \cdots & P_{nn} \end{bmatrix} \quad (7.15)$$

*Under these conditions there exists a FDLTI controller  $K = \text{blockdiag}\{K_1, \dots, K_n\}$  which achieves*

$$(i) \quad \bar{\sigma}[(H - \bar{H})\bar{H}^{-1}] \leq d_H, \text{ and}$$

$$(ii) \quad \bar{\sigma}(\bar{H}) \leq 0.707 \quad \forall \omega \geq \bar{\omega}_H$$

only if

$$\frac{\bar{\sigma}(V)}{3.414 + \bar{\sigma}(V)} \leq d_H \quad \forall \omega \geq \bar{\omega}_H \quad (7.16)$$

where:

- $V \triangleq (P - \bar{P})P^{-1} = I - \bar{P}P^{-1}$
- $d_H$  is the specified maximum allowable cross-feed performance degradation, and
- $\bar{\omega}_H$  is the specified closed-loop 3dB bandwidth of the system.

**Proof:** See [18].

This theorem has some very nice properties. First, a quantitative measure is set forth in both (i) and (ii). Property (ii) specifies that the complementary sensitivity function using the block diagonal plant must lie within the  $-3$  dB level at frequencies greater than the closed-loop crossover frequency. This allows the designer to specify the nominal performance of the system. Property (i) allows the designer to select the maximum allowable cross-feed performance degradation. Theorem 7.2 provides a *necessary* condition to determine the maximum allowable cross-feed performance degradation, and the quantitative test is very simple to calculate. Also, the fact that Equation 7.16 is computed for frequencies at or greater than the closed-loop crossover frequency increases the utility of this test. In systems with integral control, the outputs are controlled perfectly regardless of how the system is partitioned. The scaling dependence of Theorem 7.2 (i.e.,  $\bar{\sigma}(V)$ ), though, is one draw back to the broad application of this test.

Theorem 7.2 is based on the scaling dependent variable  $\bar{\sigma}(V)$ . Therefore, each time the plant is rescaled, Equation 7.16 has to be recalculated and compared to  $d_H$ . Although the calculation for Equation 7.16 is very efficient, the loosening of this condition to calculate a quantity that is not scaling dependent is desirable. This is done by using the Relative Gain Array (RGA).

As described above, the RGA is independent of scaling. Also, the RGA forms lower bounds on the condition number of a matrix as shown in [16,18]. Assuming that the plant matrix  $P$  has been partitioned into a block-diagonal form, this block-diagonal form can be imposed on the RGA. A property of the RGA is that various arrangements in the plant matrix only produce row\column rearrangements in  $\Lambda(P)$  (see Section 7.2.1 for the definition of the RGA). Therefore, modifying the input-output maps of the plant only results in rearranging the rows and columns of the RGA. If the partial row sums of the elements lying within the diagonal blocks of the RGA are defined as

$$\Pi_k \triangleq \sum_{j=\alpha_i}^{\beta_i} \Lambda(P)_{kj} \quad (7.17)$$

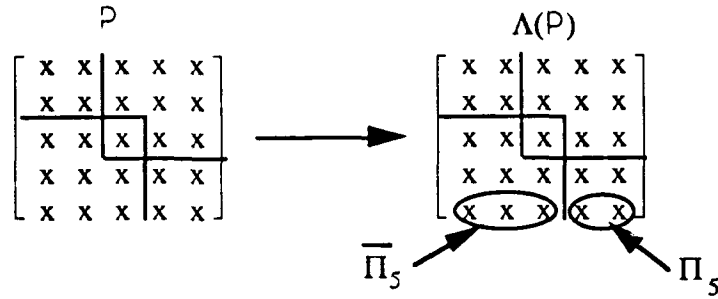


Figure 7.15: Illustration of Partial Row and Complementary Partial Row Sums of RGA

where  $k$  denotes the  $k$ th row and  $i$  denotes the  $i$ th diagonal block. The  $\alpha_i$  and  $\beta_i$  represent the beginning and ending column indices, respectively, of the  $i$ th diagonal. Figure 7.15 as taken from [18] illustrates this computation for a 5 x 5 plant. Using this property of the RGA, Theorem 7.2 can be weakened into the following Corollary.

**Corollary 7.1:** [Reeves, et al. [18]] *Theorem 7.2 remains valid if the following inequality is substituted for Equation 7.16:*

$$\frac{|\overline{\Pi}|_{max}}{3.414 + |\overline{\Pi}|_{max}} \leq d_H \quad \forall \omega \geq \overline{\omega}_H \quad (7.18)$$

where  $|\overline{\Pi}|_{max} = \max_k |\overline{\Pi}_k|$ .

**Proof:** See [18].

This result is still a quantitative, necessary condition on the cross-feed performance degradation. The advantage is that the use of the RGA now provides a scaling independent measure of the cross-feed component in the plant. This result provides an initial "screening" method for the set of possible decentralized controllers. After Corollary 7.1 has been applied, the remaining decentralized structures can be further reduced through the use of Theorem 7.2.

In Chapter 4, it was shown that the total number of possible decentralized structures for the deformable mirror system using 36 inputs with 36 sensors was  $4 \times 10^{20}$ . The test described in Corollary 7.1 was applied to  $10^7$  structures for the full model using 36 inputs with 36 sensors and all of the possible structures for the single petal model using 6 inputs with 6 sensors. These two models correspond to the case 1 and case 3 systems studied in Chapter 6. The results of these tests are described below.

#### 7.4.2 Results of Application of Cross-Feed Performance Degradation Tests to Single Petal Model

Corollary 7.1 was applied to both the single petal model and the full model using 36 sensors. This section details the results of applying Corollary 7.1 and Theorem 7.2 to the single petal model (case



System Size	Distinct Block Structures	Number of Systems Passed Cor 7.1	Minimum $d_H$ Cor 7.1	Minimum $d_H$ Thm 7.2
6x6	5x1	240	0.0766	0.6939
	4x2	240	0.1466	0.7013
	4x1x1	72	0.1616	0.6122
	3x3	360	0.1475	0.7392
	3x2x1	36	0.1475	0.4977
	3x1x1x1	18	0.1712	0.5096
	2x2x2	192	0.1475	0.5934
	2x2x1x1	48	0.1475	0.5445
	2x1x1x1x1	24	0.1571	0.5257
	1x1x1x1x1x1	4	0.1609	0.4583

Figure 7.16: Single Petal Structures Passing Theorem 7.2 and Corollary 7.1

1 - Chapter 6). The results for the single petal model provide a comparison with the results from the DIC tests described above.

The number of structures tested in the single petal case was 923. This number includes all of the possible input-output pairs arranged in all possible square combinations. Therefore, the  $6 \times 6$  plant can be divided into a structure of 6 diagonal sub-blocks, a  $5 \times 5$  sub-block and a  $1 \times 1$  sub-block, a  $4 \times 4$  sub-block and either a  $2 \times 2$  sub-block or two  $1 \times 1$  sub-blocks, etc. An arbitrary performance degradation of 20% was set for  $d_H$  in the initial calculations of Corollary 7.1. The number of structures that were found to pass each of the various structures is shown in Figure 7.16.

All of the structures that passed Corollary 7.1 were then tested using the more stringent conditions of Theorem 7.2. Not a single structure met the performance degradation requirement of 20%. It can be seen in studying Figure 7.16 that structures that intuitively should yield a smaller value of  $d_H$  do not. In particular, it seems that the larger sub-block systems should produce a better performance degradation variable ( $d_H$  should be smaller). This is not the case if the block-structure of  $5 \times 1$  is examined in Figure 7.16. Here, it is seen that the “best” performance degradation due to cross-feed is nearly 70% where the “best” performance degradation for the diagonal plant is only 45.8%. One possible reason for this apparent contradiction could be the scaling issue described above. If the plant is rescaled, the performance degradation using Theorem 7.2 will change. It was also shown in an example in [10] that block decentralized structures do not necessarily imply an improvement in performance over fully decentralized structures. For the case of the single petal model, scaling was applied and had little effect on the cross-feed performance degradation as calculated from the conditions of Theorem 7.2.

The result of using Equation 7.16 is a little surprising considering the apparent success of the

DIC tests described in Section 7.2. After further analysis, though, the results from these viability tests provide some confirmation to the results found in the design of the DIC controller. A closer examination of the particular input-output structure  $([1, 4], [2, 3], [3, 2], [4, 1], [5, 5], [6, 6])$  used to design the DIC controller shows that the value of the cross-feed performance degradation,  $d_H$ , as calculated from Corollary 7.1 is  $d_H = 0.2152$ . Therefore, Corollary 7.1 predicts a 22% degradation in performance if a diagonal controller is used for the given input-output ordering. Application of Theorem 7.2 to the same structure yields a cross-feed performance degradation of 70.57%. This is closer to the 82% reduction in performance used for the DIC.

If the cross-feed performance degradation factor is calculated for all structures of the diagonal plant (calculating the left-hand side of Equation 7.18), the minimum cross-feed performance degradation for Corollary 7.1 occurs for the input-output pairing,  $([1, 4], [2, 2], [3, 3], [4, 1], [5, 5], [6, 6])$ . The value of cross-feed performance degradation as calculated from Corollary 7.1 is 16.1%. Again, when the more stringent Theorem 7.2 condition is applied, the cross-feed performance degradation lowers to 70.96%. It is interesting to note that the minimum cross-feed performance degradation for Corollary 7.1 occurs for input-output pairs that do not match  $z$ -axis sensors with  $z$ -axis actuators and “in-plane” sensors with “in-plane” actuators.

If the cross-feed performance degradation factor is minimized according to the calculation of the Theorem 7.2 test (calculation of the left-hand side of Equation 7.16), the input-output structure becomes  $([1, 3], [2, 1], [3, 2], [4, 6], [5, 5], [6, 4])$ . This particular input-output structure yields a cross-feed performance degradation factor as calculated by Corollary 7.2 of 45.8%. Again, the input-output pairing does not follow the intuition of matching actuator displacement axes to sensor axes.

### 7.4.3 Results of Application of Cross-Feed Performance Degradation Tests to the Full Model Using 36 Sensors

The test for Corollary 7.1 was used for  $10^7$  cases of the full model using 36 sensors. The only structures tested were  $6 \times 6 \times 6 \times 6 \times 6 \times 6$ ,  $12 \times 24$  and  $18 \times 18$ . Out of these potential structures, only 237 passed the cross-feed performance degradation bound of 20%. When the Theorem 7.2 test was employed, no structure was found that met the cross-feed performance degradation bound.

The results of these tests do not eliminate the possibility of a decentralized structure for the full model case. These results do eliminate  $10^7$  combinations for the block structures listed above.

## 7.5 Conclusion

This chapter has detailed some necessary tests that can be easily applied to a plant to determine if a decentralized structure exists. These tests illustrated that a decentralized integral controller

could be designed for a diagonal plant structure, and SISO integral controllers were designed. It was shown that the use of these SISO controllers forced an 82% reduction in the performance in order for robust performance to be maintained. The  $\mu$  interaction measure was introduced and applied to the 10 structures that met the DIC requirements. The  $\mu$  interaction measure showed that only 1 structure was found that met the requirements for decentralized integral controllability. Finally, necessary tests for viability of control configurations was introduced. These tests developed a measure of cross-feed performance degradation based on different input-output pairings and sub-block structures. These tests were applied to the single petal model, and the results from the Theorem 7.2 test predicted a 71% degradation in performance for the SISO case example. This prediction compares reasonably well with the actual loss of 82% in robust performance. The Corollary 7.1 and Theorem 7.2 tests predicted a very non-intuitive structure to result in a lower cross-feed performance degradation. Finally, Corollary 7.1 was applied to  $10^7$  separate structures for the full model case using 36 sensors, but no structure was found that passed Theorem 7.2 for the same cross-feed performance degradation factor.

# Chapter 8

## Conclusion

In this thesis, an  $H_\infty$  controller was designed for the deformable mirror system to meet a set of performance specifications detailed in Chapter 2. Loop-shaping as a method of augmenting the performance requirement into the controller was demonstrated in the synthesis of the controller, and acceptable controllers were synthesized to meet the robust performance specification for the single petal model and the full model using 24 sensors. This chapter presents a summary of the effort in this thesis and describes topics for future research.

### 8.1 Summary of Thesis

Chapter 2 described the deformable mirror system and established the performance requirement in terms of a wavefront error. The state-space model of the deformable mirror was described, and the block-diagram for the control function was presented.

The tools used in the evaluation of performance in this thesis were developed in Chapter 3. The  $L_2$  space was defined, and the definition of the  $H_2$  norm was developed. The  $H_2$  problem was then presented as was the  $H_\infty$  problem. The structured singular value was introduced as a non-conservative measure of robust stability and performance. Using the small gain theorem as motivation, the small  $\mu$  theorem was presented, and the method of using the structured singular value as a robust performance measure was defined.

Chapter 4 provided a detailed problem statement listing issues and developing subgoals for the synthesis of a controller for the deformable mirror system. The difficulties with the physical dimension of the models of the deformable mirror system were discussed, and the issue of sensor selection was presented. The first subgoal established was to develop a comprehensive understanding of the single petal model and attempt to apply this knowledge to the full model. This was accomplished, in part, in Chapters 5, 6, and 7. The second subgoal was to determine the "optimal" sensor selection method. This second subgoal was met only initially through open-loop analyses in Chapter 5.

The final subgoal was to determine a decentralized structure for the full model. The resolution of this subgoal is described in more detail below.

Chapter 5 presented the open-loop analyses conducted on a single petal model and 2 full model cases. The first full model case used 24 sensors, and it was shown that this case was fully observable and controllable. The second full model used 36 sensors, and it was shown to also be fully observable and controllable. The sensor selection for each of the three models was based on minimizing the condition number of each separate plant model. This minimization proved to be sufficient in the calculation of controllers to meet the robust performance requirement. Chapter 5 also illustrated the importance of balancing the plant models.

The results of the controller synthesis and analyses were presented in Chapter 6. Three separate cases were studied including the single petal model, the full model using 24 sensors, and the full model using 36 sensors. The method of augmenting performance states into the synthesis problem was developed, and the results for the single petal model and full model using 24 sensors were almost identical. The controller synthesized was able to meet the performance specification for a sensor accurate to within 1% for low frequencies. The results from the single petal model did not scale fully to the full model using 36 sensors. The full model using 36 sensors required a sensor accurate to within 0.1% for low frequencies in order to meet the robust performance specifications.

Chapter 7 detailed the decentralized analyses employed in an effort to find a decentralized structure for the deformable mirror system. The motivation for using decentralized control was presented, and simple tests for Decentralized Integral Controllability (DIC) were presented for cases where a plant can be completely diagonalized. Ten cases using the single petal model were found that met the requirements imposed by the necessary DIC tests, and a Single Input Single Output (SISO) controller was developed to demonstrate this capability. It was shown that the performance had to be reduced by 82% in order to maintain robust performance using the DIC controller. Interaction measures were introduced, and the  $\mu$  interaction measure was used to test the ten structures that passed the simple DIC tests. It was found that only one structure of the ten met the stricter requirements of the  $\mu$  interaction measure. Finally, viability tests were presented and used to determine the cross-feed performance degradation caused by different decentralized structures and input-output pairings. The tests were applied to the structure used to develop the SISO controller, and the weaker test (Corollary 7.1) predicted a loss in performance of 21% while the Theorem 7.2 test predicted a loss in performance of 71%. The minimum cross-feed performance degradation was then determined for the diagonal structure, and the non-intuitive matching radial and tangential motion sensors to "z" axis actuators was observed. Finally, the Corollary 7.1 test was applied to  $10^7$  combinations of the full model using 36 sensors, and only a small subset met

the cross-feed performance degradation requirement of 20%. When the more stringent Theorem 7.2 test was applied, no structure met the performance degradation requirement.

This summary only begins to address the problem of robust wavefront control for the deformable mirror system. With this in mind, the following topics for future research are presented.

## 8.2 Topics for Future Research

To fully design a robust controller, the uncertainty sources should be incorporated into the synthesis of the controller. This thesis synthesized a controller for the nominal plant, and then measured the performance robustness. Using the method of  $\mu$  synthesis, a robust controller can be developed that meets a robust performance requirement. The algorithms to calculate  $\mu$  are still being tuned, and the computation time required to synthesize a robust performing controller for the deformable mirror system may be prohibitive. Still, the application of  $\mu$  synthesis techniques might provide more insight on the trade between uncertainty and performance.

The only uncertainty source considered in this thesis was uncertainty in the sensor. In actuality, uncertainty will occur at numerous other locations in the deformable mirror system. To be able to state that the deformable mirror system actually meets a robust performance requirement, each of these additional uncertainty sources should be included in the analysis.

The success of finding a decentralized controller for the single petal model partially offsets the failure of finding some decentralized structure for the full model. Due to computation limitations, only a small subset of the total possible combinations was tested. The ability to find a decentralized control structure for the full model would provide an important step in actually developing a controller for the deformable mirror system. A decentralized structure would not be as limited to the number of computations required of a centralized controller.

A methodology needs to be developed to determine sensor locations for feedback to the controller, sensor locations used for controller synthesis, and sensor locations for evaluation points. In this thesis, the sensors used for feedback to the controller were a subset of the sensors used for both the controller performance points as well as the evaluation points. There is a strong need to have some methodology to determine the selection procedures for this set of measurements. When faced with the potential of 216 measurement locations, there is a strong motivation to reduce the physical size of the model. Through analyses of the performance, there might be a way to determine a subset of the potential measurements for each of the three sets of points individually. There has been a great deal of research in this area in the chemical process industry. The parallels between the control of multivariable distillation processes to the segment phasing control of the deformable mirror system suggests a possible untapped area of experience.

Finally, the segment phasing control problem represents only one problem of a complete SDI system. The issues involved in mounting the deformable mirror system on a "noisy" structure and rapidly rotating the structure to follow a target have not been addressed. The actual measurement system required for the deformable mirror system has not been addressed. Only the accuracy of edge sensors over a limited frequency band has been examined.

## Appendix A

# Performance Criteria Relations

The rms performance requirement detailed in Section 2.3 was shown to relate to the 2-norm of the error. This appendix relates the  $\infty$ -norm performance criterion established in Chapter 3 to a stochastic system with assumed zero-mean, stationary stochastic disturbance inputs of bounded variance (standard deviation) as shown in [11]. The standard deviation of an error vector is defined by

$$E\{e^T e\} = \sigma_e^2 \quad (\text{A.1})$$

Using the trace operator and the linearity of the expectation operator, Equation A.1 can also be written in the frequency domain in terms of the power spectral density of  $e$ ,  $\Phi_{ee}$

$$E\{e^T e\} = \frac{1}{2\pi} \int_{-\infty}^{\infty} \text{tr}[\Phi_{ee}(j\omega)] d\omega \quad (\text{A.2})$$

If we assume that the output error is generated from some disturbance input,  $d(s)$ , and stable transfer function matrix,  $H(s)$

$$e(s) = H(s)d(s)$$

the power spectral density  $\Phi_{ee}$  can be written as

$$\Phi_{ee}(j\omega) = H(j\omega)\Phi_{dd}(j\omega)H^T(-j\omega) \quad (\text{A.3})$$

Equation A.2 and Equation A.3 then imply [14]

$$E\{e^T e\} = \frac{1}{2\pi} \int_{-\infty}^{\infty} \sum_i \sigma_i^2 (\Phi_{dd}^{\frac{1}{2}}(j\omega)H(j\omega)) d\omega \quad (\text{A.4})$$

from which the bound

$$E\{e^T e\} \leq \|H\|_{\infty}^2 \frac{1}{2\pi} \int_{-\infty}^{\infty} \sum_i \sigma_i^2 (\Phi_{dd}^{\frac{1}{2}}(j\omega)) d\omega \quad (\text{A.5})$$

follows. Consequently, for the case of white disturbance inputs

$$\Phi_{dd}(j\omega) = I$$



the following result holds

$$\sigma_e \leq \|H\|_\infty \quad (\text{A.6})$$

From Equation A.6, it is clear that if the input,  $d$ , is a white noise process with unity variance, then the error variance will be unity bounded only if

$$\|H\|_\infty \leq 1$$

Therefore, the stochastic optimal control problem results in a performance constraint on the  $H_\infty$ -norm of the transfer function,  $H$ , as long as the input,  $d$ , and the error vector,  $e$ , are scaled correctly.

# Bibliography

- [1] Anderson, B. D. O. and Moore, John B. , *Optimal Control - Linear Quadratic Methods*, Prentice Hall, Englewood Cliffs, New Jersey, 1990.
- [2] Brogan, William L. , *Modern Control Theory*, Prentice Hall, Englewood Cliffs, New Jersey, 1985.
- [3] Brosilow, C. B. , and Weber, R. , "The Use of Secondary Measurements to Improve Control", *AICHE Journal*, Vol 18, No 3, May 1972.
- [4] Chiang, R. Y. and Safonov, M. G. , "Robust Control Toolbox for use with MATLAB, User's Guide", *The MathWorks, Inc.*, June 1, 1988.
- [5] Desoer, C. A. and Vidyasagar, M., *Feedback Systems: Input-Output Properties*, Academic Press, New York, 1975.
- [6] Doyle, J. C. , "Analysis of feedback systems with structured uncertainties," *Proc. IEE*, vol. 129, no. 6, pp. 242-250, Nov. 1982.
- [7] Doyle, John, Glover, Keith, Khargonekar, Pramod, and Francis, Bruce, "State-Space Solutions to Standard  $H_2$  and  $H_\infty$  Control Problem." *Procedures of American Control Conference*, Atlanta, GA, June15-17, 1988.
- [8] Francis, Bruce A. , *A Course in  $H_\infty$  Control Theory*, Lecture Notes in Control and Information Sciences, Springer-Verlag, New York.
- [9] Freudenberg, J. S. , and Looze, D. P. , *Frequency Domain Properties of Scalar and Multivariable Feedback Systems*, Lecture Notes in Control and Information Sciences, Springer-Verlag, New York.
- [10] Grosdidier, P. , and Morari, M. , "Interaction Measures for Systems Under Decentralized Control." *Automatica*, 22, pp. 309-319, 1986.

- [11] Hammett, Kelly, D., "Application of Multivariable Control System Design Methodologies to Robust Beam Control of a Space-Based Laser," Master's Thesis, MIT, 1991.
- [12] Kailath, T. , *Linear Systems*, Prentice Hall, Englewood Cliffs, New Jersey, 1980.
- [13] Kwakernaak, H. and Sivan, R., *Linear Optimal Control Systems*, Wiley-Interscience, New York, 1972.
- [14] Maciejowski, J. M. , *Multivariable Feedback Design*, Addison-Wesley Publishing Company, Reading, Massachusetts, 1990.
- [15] Moore, B. C. , "Principal Component Analysis in Linear Systems: Controllability, Observability, and Model Reduction." *IEEE Trans. Autom. Control*, AC-26, pp. 17-27, 1981.
- [16] Morari, M. and Zafrou, E. , *Robust Process Control*, Prentice Hall, New Jersey, 1989.
- [17] Nett, C. N. and Manousiouthakis, V., "Euclidean Condition and Block Relative Gain: Connections, Conjectures, and Clarifications." *IEEE Trans. Autom. Control*, AC-32, pp. 405-407, 1987.
- [18] Reeves, D. E. , Nett, C. N. , and Arkun, Y. , "Control Configuration Design for Complex Systems: A Practical Theory." Submitted to the *IEEE Trans. Autom. Control*, January, 1991.
- [19] Safonov, M. G. , Laub, A. J. , and Hartmann, G. L. , "Feedback Properties of Multivariable Systems: The Role and Use of the Return Difference Matrix." *IEEE Trans. Autom. Control*, Vol. 26, No. 1, pp. 47-65, 1981.
- [20] Skogestad, S. , Morari, M. , and Doyle, J. C. , "Robust Control of Ill-Conditioned Plants: High Purity Distillation." *IEEE Trans. Autom. Control*, Vol. 33, No. 12, pp. 1092-1105, 1988.
- [21] Schilling, R. J. and Lee, H. , *Engineering Analysis - A Vector Space Approach*, John Wiley and Sons, Toronto, Canada, 1988.
- [22] Vidyasagar, M. , *Nonlinear Systems Analysis*, Prentice-Hall, Inc., Englewood Cliffs, New Jersey, 1978.
- [23] Youla, D. C. , Bongiorno, J. J. , and Jabr, H. A. , "Modern Wiener-Hopf Design of Optimal Controllers - Part I. The Single Input-Output Case." *IEEE Trans. Autom. Control*, AC-21, pp. 3-13, 1976.

- [24] Youla, D. C. , Bongiorno, J. J. , and Jabr, H. A. , "Modern Wiener-Hopf Design of Optimal Controllers - Part II. The Multivariable Case." *IEEE Trans. Autom. Control*, AC-21, pp. 319-338, 1976.
- [25] Zames, G. , "Feedback and Optimal Sensitivity: Model Reference Transformations, Multiplicative Seminorms and Approximate Inverses." *IEEE Trans. Autom. Control*, AC-26, pp. 301-320, 1981.
- [26] Zames, George, and Francis, Bruce A. , "Feedback, Minimax Sensitivity, and Optimal Robustness." *IEEE Trans. Autom. Control*, AC-28, pp. 585-601, 1983.

**Information to Accompany Master of Science Thesis**

Author: Edgar M. Vaughan, Capt, USAF

Date: 1991

Number of Pages: 104

Degree Awarded: Master of Science in Electrical Engineering

Name of Institution: Northeastern University